

Climate Variability in the Eastern Indian Ocean during Marine Isotope Stage 3: High-Resolution Proxy Studies from the Timor Sea

Dissertation

zur Erlangung des Doktorgrades
der Mathematisch-Naturwissenschaftlichen Fakultät
der Christian-Albrechts-Universität
zu Kiel

vorgelegt

von

Anke Dürkop

Kiel, 2010

Referent Prof. Dr. Wolfgang Kuhnt

Korreferentin Priv.-Doz. Dr. Mara Weinelt

Tag der mündlichen Prüfung: 14.07.2009

Zum Druck genehmigt: 11.06.2010

gez. Prof. Dr. Lutz Kipp, Dekan

Abstract

Paleoclimate reconstructions based on marine sediment proxy data are important to understand the mechanisms of past climates and to test the predictability of climate models with regard to future climate predictions. Marine Isotope Stage 3 (MIS 3), a time period of high climate variability on millennial timescales with different shapes of temperature increases in the Northern and Southern Hemispheres as firstly detected in Greenland and Antarctica ice core records, is therefore subject of this thesis. During MIS 3 high-latitude Northern Hemisphere temperatures abruptly shifted to interstadial conditions (Dansgaard-Oeschger events) followed by gradual decreases to stadial conditions (Heinrich events), whereas the high-latitude Southern Hemisphere experienced gradual temperature in- and decreases. In contrast to the wealth of information concerning the regional climate impacts in the Northern Hemisphere high latitudes, relatively little is known about the low-latitude responses to these climate fluctuations and about the role of the tropics.

To elucidate high- and low-latitude interactions in the tropics and to gain insights into the regional climate changes during MIS 3 high-resolution marine sediment multi-proxy records from the tropical eastern Indian Ocean (Timor Sea) were analyzed. Today, this area is influenced by the Intertropical Convergence Zone, which drives monsoonal winds, and by the Indonesian Throughflow (ITF), which represents a key component of the global thermohaline circulation system connecting the Pacific with the Indian Ocean. Thus, cores from the Timor Sea are ideally situated to monitor the linkages between tropical and high-latitude climate as well as regional paleoceanography and climate settings.

Benthic $\delta^{18}\text{O}$ data (*P. wuellerstorfi*) clearly covary with Antarctic warm events as recorded in Southern Hemisphere ice cores. This southern high-latitude signal is transferred by Antarctic Intermediate Water flowing northward from the Southern Ocean into the Indian Ocean. Planktonic $\delta^{18}\text{O}$ (*G. ruber*) records show close affinity to northern high-latitude records and covary with Greenland temperature signals. These northern high-latitude signals in the tropical surface water are probably transmitted through atmospheric teleconnections and a tight coupling of the Asian-Australian monsoon system. Regional monsoon variability in the Timor Sea during D-O interstadials are estimated with respect to modern temperature and salinity conditions.

Planktonic foraminiferal stable isotope values, Mg/Ca temperature and $\delta^{18}\text{O}_{\text{seawater}}$ estimates (*G. ruber* and *P. obliquiloculata*) reveal a weaker ITF intensity with a reduced transport of less saline water from the Pacific into the Indian Ocean during Heinrich events. During these stadials, when sealevel was extensively lowered, the regional paleoceanography in the outflow area of the

ITF was influenced by a northward moving hydrological front between the West Australian Current and the Leeuwin Current.

This front is probably associated with a change in food export to the seafloor as indicated by changing benthic foraminiferal accumulation rates of globocassidulinids. In contrast carbon-flux sensitive buliminids reveal increased abundances during Southern Hemisphere stadials due to higher paleoproductivity modulated by changes in the Asian-Australian monsoon system.

Zusammenfassung

Paläoklima-Rekonstruktionen, die auf Proxy-Daten mariner Sedimente basieren, sind entscheidend für das Verständnis vergangener Klimamechanismen und dienen der Überprüfung der Vorhersagbarkeit von Klimamodellen im Hinblick auf zukünftige Klimavorhersagen. Das Marine Isotopenstadium 3 (MIS 3), ein Zeitraum mit hoher Klimavariabilität auf Jahrtausend-Zeitskalen mit unterschiedlich gestalteten Temperaturerhöhungen der Nord- und Südhemisphäre, die zuerst in grönländischen beziehungsweise antarktischen Eiskernaufzeichnungen nachgewiesen wurden, ist daher Gegenstand dieser Doktorarbeit. Während MIS 3 stiegen die Temperaturen der nördlichen hohen Breiten abrupt bis hin zu interstadialen Bedingungen (Dansgaard-Oeschger-Ereignisse) an, ehe sie allmählich auf stadiale Werte (Heinrich-Ereignisse) zurückfielen. Den hohen Breiten der Südhemisphäre hingegen widerfuhren sowohl graduelle Temperaturanstiege als auch -abnahmen. Im Gegensatz zu der Fülle an Informationen über die Auswirkungen auf das regionale Klima in den hohen nördlichen Breiten ist nur wenig bekannt über die Resonanz der niederen Breiten auf diese klimatischen Schwankungen und über die Rolle der Tropen.

Um die Wechselwirkung von hohen und niederen Breiten und regionalen Klimaveränderungen näher bestimmen zu können, wurden hochauflösende Multiproxy-Aufzeichnungen mariner Sedimente aus dem tropischen östlichen Indischen Ozean (Timor See) erstellt. Heutzutage wird diese Region durch die Innertropische Konvergenzzone (ITCZ), die Monsunwinde antreibt, und durch den Indonesischen Durchstrom (ITF), der als Schlüsselkomponente in der globalen thermohalinen Zirkulation den Pazifik mit dem Indischen Ozean verbindet, beeinflusst. Daher sind die Sedimentkerne aus der Timor See hervorragend dazu geeignet, die Kopplung zwischen dem tropischen Klima und dem der hohen Breiten sowie die regionale Paläozeanographie und die regionalen klimatischen Zustände nachzuvollziehen.

Benthische $\delta^{18}\text{O}$ -Daten (*P. wuellerstorfi*) kovariieren deutlich mit antarktischen Warmereignissen, die in Eiskernen der Südhemisphäre aufgezeichnet wurden. Dieses Signal aus den südlichen hohen Breiten wurde über nordwärts strömende Tiefen- und Zwischenwassermassen vom Südlichen Ozean in den Indischen Ozean transportiert. Planktonische $\delta^{18}\text{O}$ -Daten (*G. ruber*) wiederum ähneln Eiskernaufzeichnungen aus den hohen nördlichen Breiten und kovariieren mit grönländischen Temperatursignalen. Diese Signale aus dem hohen Norden wurden möglicherweise über atmosphärische Telekonnektionen und das asiatisch-australische Monsunsystem in das tropische Oberflächenwasser übertragen.

Regionale Monsunschwankungen in der Timor See während der D-O-Interstadiale wurden anhand von modernen Temperatur- und Salzgehaltmessungen abgeschätzt.

Sowohl stabile Isotopenverhältnisse als auch Mg/Ca-Temperatur- und $\delta^{18}\text{O}_{\text{Meerwasser}}$ -Abschätzungen an planktonischen Foraminiferen (*G. ruber* und *P. obliquiloculata*) zeigen eine abgeschwächte ITF-Intensität und einen reduzierten Transport von geringsalinen Wassermassen aus dem Pazifik in den Indischen Ozean während der Heinrich-Ereignisse an. Während dieser Stadiale, wenn der Meeresspiegel deutlich abgesenkt war, wurde die regionale Paläozeanographie im ITF-Ausstromgebiet durch eine sich nordwärts bewegende hydrologische Front zwischen dem Westaustralstrom und dem Leeuwinstrom beeinflusst.

Diese Front steht wahrscheinlich im Zusammenhang mit Änderungen im Export des Nahrungsangebotes zum Meeresboden, der durch sich verändernde Akkumulationsraten benthischer Foraminiferen (Globocassidulinen) angezeigt wird. Im Gegensatz dazu treten Buliminen, die sensitiv auf Änderungen von Kohlenstofffluss-Raten reagieren, während der Südhemisphären-Stadiale häufig auf, was in den Zusammenhang mit höherer Paläoproduktivität gebracht werden kann. Diese steht möglicherweise in Verbindung mit Änderungen im Asiatisch-Australischen Monsunsystem.

Danksagung

Hiermit bedanke ich mich bei Prof. Dr. Wolfgang Kuhnt und Dr. Ann Holbourn für die Vergabe der Doktorarbeit, deren Betreuung und für die mir ermöglichte Teilnahme an der SONNE-Ausfahrt "VITAL" im Jahr 2005.

Frau Priv.-Doz. Dr. Mara Weinelt danke ich herzlich für die Übernahme des Korreferates.

Bei meiner Familie, meinen Freunden und Kollegen möchte ich mich für die stetige und liebevolle Unterstützung bedanken.

Der Deutschen Forschungsgemeinschaft danke ich für die Finanzierung des Projektes Ku649/25-1 und Ku649/25-2. Dem deutschen Bundesministerium für Bildung und Forschung danke ich für die Finanzierung eines vierwöchigen Studienaustausches am "College of Ocean and Earth Science" der Tongji University in Shanghai.

*Ich bin dankbar, nicht weil es vorteilhaft ist,
sondern weil es Freude macht.*

(von Seneca)

Contents

| | |
|--|-------------|
| Abstract | i |
| Danksagung | v |
| List of Figures | viii |
| List of Tables | ix |
| 1 Introduction | 1 |
| 1.1 Climate and paleoclimate reconstructions | 1 |
| 1.1.1 Influencing factors of climate change | 1 |
| 1.1.2 Short-term variability during Marine Isotope Stage 3 | 2 |
| 1.1.3 Motivations for this study | 5 |
| 1.1.4 Aims of this study | 7 |
| 1.1.5 Structure of this thesis | 9 |
| 2 Centennial-Scale Climate Variability in the Timor Sea | 11 |
| 2.1 Introduction | 12 |
| 2.2 Material and method | 14 |
| 2.2.1 Paleooceanographic setting | 14 |
| 2.2.2 Stable isotopes | 14 |
| 2.2.3 Accelerator mass spectrometry | 16 |
| 2.2.4 Benthic foraminiferal census counts | 16 |
| 2.3 Results | 17 |
| 2.3.1 Age model | 17 |
| 2.3.2 Stable isotopes | 20 |
| 2.3.3 Benthic foraminiferal census counts | 21 |
| 2.4 Discussion | 23 |
| 2.4.1 Northern and Southern Hemisphere climate control | 23 |
| 2.4.2 Paleoproductivity variations in the Timor Sea during MIS 3 | 24 |
| 2.5 Conclusions | 26 |
| 2.6 Acknowledgments | 26 |
| 3 Indonesian Throughflow slow-down during Heinrich Events | 27 |
| 3.1 Introduction | 28 |
| 3.2 Material and method | 30 |
| 3.2.1 Mg/Ca analysis | 30 |

| | | |
|----------|--|-----------|
| 3.2.2 | Stable isotope analysis | 32 |
| 3.2.3 | Paleo-salinity reconstruction from $\delta^{18}\text{O}$ seawater | 32 |
| 3.2.4 | Age model | 33 |
| 3.3 | Results | 34 |
| 3.3.1 | Oxygen isotopes | 34 |
| 3.3.2 | Mg/Ca temperature reconstructions | 36 |
| 3.3.3 | Sea surface and upper thermocline salinity estimates ($\delta^{18}\text{O}_{sw}$) | 36 |
| 3.3.4 | Carbon isotopes | 38 |
| 3.4 | Discussion | 38 |
| 3.4.1 | Timor Sea hydrography and planktonic foraminiferal habitats | 38 |
| 3.4.2 | Decrease in ITF intensity during Heinrich events | 40 |
| 3.4.3 | Main controls of ITF variability during MIS 3 | 42 |
| 3.5 | Conclusions | 44 |
| 3.6 | Acknowledgments | 45 |
| 4 | High-latitude climate signals and monsoon related regional climate variability | 47 |
| 4.1 | Introduction | 48 |
| 4.2 | Oceanographic and climate setting | 50 |
| 4.3 | Material and method | 52 |
| 4.3.1 | Stable isotope values | 52 |
| 4.3.2 | Accelerator mass spectrometry | 53 |
| 4.3.3 | Benthic foraminiferal census counts | 54 |
| 4.4 | Results | 56 |
| 4.4.1 | Age model | 56 |
| 4.4.2 | Stable isotope values | 57 |
| 4.4.3 | Benthic foraminiferal census counts | 61 |
| 4.5 | Discussion | 61 |
| 4.5.1 | Southern Hemisphere climate signals and regional differences in benthic oxygen and carbon isotope records from the Eastern Indian Ocean | 63 |
| 4.5.2 | Northern Hemisphere climate signals, monsoon activity, and regional differences in planktonic oxygen and carbon isotope values from the Eastern Indian Ocean | 65 |
| 4.5.3 | Regional differences in benthic foraminiferal abundances in the Eastern Indian Ocean | 68 |
| 4.6 | Conclusions | 70 |
| 4.7 | Acknowledgment | 71 |
| 5 | Summary | 73 |
| 5.1 | High-resolution age model for Marine Isotope Stage 3 | 73 |
| 5.2 | High-latitude climate signals in the tropics | 74 |
| 5.3 | Paleoproductivity in the Timor Sea | 75 |
| A | Taxonomic list | 77 |
| | Bibliography | 78 |

List of Figures

| | | |
|-----|--|----|
| 1.1 | Methane synchronized oxygen isotope records of the EDML and NGRIP ice cores | 3 |
| 1.2 | Position of the Intertropical Convergence Zone (ITCZ) | 4 |
| 1.3 | Spatial distribution of sites with clear D-O type climate oscillations and without or unclear D-O cyclicity | 6 |
| 1.4 | Study sites, salinity, temperature and oxygen profiles from Timor Sea | 8 |
| 2.1 | Geographic Map | 13 |
| 2.2 | Different Morphotypes of <i>P. wuellerstorfi</i> | 15 |
| 2.3 | Benthic $\delta^{18}\text{O}$ versus depth of Core MD01-2378 | 18 |
| 2.4 | Age/ depth plot of Core MD01-2378 | 19 |
| 2.5 | Benthic and planktonic $\delta^{18}\text{O}$ of Core MD01-2378 and $\delta^{18}\text{O}$ of EDML and NGRIP ice cores | 20 |
| 2.6 | Proxy data of Core MD01-2378 and December and February insolation at 25° S | 22 |
| 3.1 | Annual temperature and salinity distribution in the Indo-Pacific | 29 |
| 3.2 | Oxygen isotope values, Mg/Ca derived SST, and ice volume corrected oxygen isotopes | 35 |
| 3.3 | Oxygen isotope values (measured and seawater corrected) | 37 |
| 3.4 | Carbon isotopes and gradient | 39 |
| 3.5 | Temperature and salinity profiles | 40 |
| 3.6 | Comparison of sea level reconstructions, benthic $\delta^{18}\text{O}_{sw}$, temperatures and insolation during MIS 3 | 43 |
| 4.1 | Geographic Map | 49 |
| 4.2 | Monthly temperature and salinity at positions of Cores SO-185 18460 located in the Timor Passage and MD01-2378 in the Timor Sea | 51 |
| 4.3 | Benthic $\delta^{18}\text{O}$ versus depth of Core SO-185 18460 | 55 |
| 4.4 | Age/ depth plot of Core SO-185 18460 | 57 |
| 4.5 | Benthic and planktonic $\delta^{18}\text{O}$ of Core SO-185 18460 and $\delta^{18}\text{O}$ of EDML and NGRIP ice cores | 58 |
| 4.6 | Benthic and planktonic $\delta^{18}\text{O}$ and $\delta^{13}\text{C}$ of Cores SO-185 18460 and MD01-2378 | 60 |
| 4.7 | Benthic and planktonic $\Delta\delta^{18}\text{O}$, $\Delta\delta^{13}\text{C}$, $\Delta\delta^{18}\text{O}_{sw}$, ΔSST (SO-185 18460 minus MD01-2378) and Insolation at 25°S | 62 |
| 4.8 | Benthic foraminiferal $\delta^{18}\text{O}$ and accumulation rates of Cores SO-185 18460 and MD01-2378 | 64 |

List of Tables

| | | |
|-----|---|----|
| 2.1 | AMS ^{14}C dates <i>G. ruber</i> (white) in Core MD01-2378 | 16 |
| 2.2 | Tie points between MD01-2378 foraminiferal $\delta^{18}\text{O}$ and EDML ice core $\delta^{18}\text{O}$. . | 17 |
| 3.1 | Comparison of average water temperatures at sea surface and 100 m water depth with Mg/Ca and $\delta^{18}\text{O}$ derived temperature estimates | 31 |
| 3.2 | Tie points between MD01-2378 benthic foraminiferal $\delta^{18}\text{O}$ and EDML/ NGRIP ice core $\delta^{18}\text{O}$ | 34 |
| 4.1 | AMS ^{14}C dates <i>G. ruber</i> in Core SO-185 18460 | 53 |
| 4.2 | Tie points between SO-185 18460 foraminiferal $\delta^{18}\text{O}$ and EDML/ NGRIP ice core $\delta^{18}\text{O}$ | 54 |

Chapter 1

Introduction

1.1 Climate and paleoclimate reconstructions

Understanding natural climate variability is important for predictions of future climate evolution and to differentiate between natural and anthropogenic influences. Climate models are used to investigate modern and paleoclimate changes and to predict future climate changes. Models are important to understand mechanisms of climate change and to test physical hypothesis. Especially paleoclimate reconstructions are supported by simulations bridging local informations and developing global patterns (*Jansen et al., 2007*). On the other hand paleoclimate data are essential to evaluate the ability of climate models to simulate realistic climate changes.

1.1.1 Influencing factors of climate change

Numerous cyclic and non-cyclic processes affect Earth's climate. These processes appear to be superimposed on each other and result in enhancing, reducing or compensating effects.

Influencing factors are:

- Changes in Earth's orbit
- Changes in solar output
- Changes in the concentration of Greenhouse Gases in the atmosphere
- Changes in the distribution of continents and oceans.

Sequences of glacial-interglacial cycles are documented by paleoclimatic records from Antarctica in ice cores (*EPICA Community Members, 2004*) covering the last 740 kyr, in deep sea sediment cores (*Lisiecki and Raymo, 2005*) and loess deposits (*Ding et al., 2002; Chlachula, 2003; Chen, 2009*) covering several million years. Changes in the Milankovitch parameters (eccentricity: 100 kyr, obliquity: 41 kyr and precession: 19–23 kyr) are modulating latitudinal and seasonal insolation distribution, which can be calculated for past and future changes with a high degree of confidence (*Berger and Loutre, 1991; Laskar et al., 2004*). Furthermore there are observations

that the total solar irradiance variation affect meteorological parameters (*Labitzke and Matthes, 2003; Solanki et al., 2004*) which if sustained on longer timescales could be a significant forcing for climate change. However, there is still a debate about the strength of solar activity cycle effects on Earth's climate as the physical mechanisms remain unclear. Another important factor on orbital timescale climate changes is the concentration of Greenhouse gases, primarily CO₂ (*Ruddiman, 2006*). Paleoclimate model simulations support the importance of CO₂ in explaining global mean temperatures in the geologic past (*Ledley et al., 1999*). Glacial periods are associated with low natural CO₂ concentrations and interglacial periods with high natural CO₂ concentrations. Additionally the distribution of the continents are suggested to play a crucial role for coolings and warmings (*Pearson and Palmer, 1999*). While plate tectonics led to changes of ocean gate ways (*Cane and Molnar, 2001*) ocean circulation underwent strong reorganizations resulting in climate changes.

1.1.2 Short-term variability during Marine Isotope Stage 3

The Pleistocene is characterized by repeated glacial cycles with ice sheets covering $\approx 30\%$ of the Earth. Climate changes during the last 800 kyr of the Pleistocene are reflected as cycles with a period of about 100 kyr (*Shackleton, 2000*) with even numbered glacial and odd numbered interglacial Marine Isotope Stages in marine sediment cores. An exception to this general rule is Marine Isotope Stage 3 (MIS 3), which can not be described as an interglacial due to its lowered sea levels (-60 m and -90 m) compared to the present (*Chappell, 2002; Siddall et al., 2003, 2008*). Additionally MIS 3 occurred not on the 100 000 yr interglacial cycle, which persisted the 800 kyr before (*Lisiecki and Raymo, 2005*). Fluctuating climate conditions on millennial timescales characterize MIS 3 covering the time period between 60–25 ka BP. These rapid climate oscillations have been largely documented in Greenland ice cores (*Johnsen et al., 1992; Dansgaard et al., 1993; Grootes et al., 1993*) and in sediment cores from the adjacent North Atlantic (*Bond et al., 1993; van Kreveland et al., 2000*) and the Iberian Margin (*Shackleton et al., 2000; Martrat et al., 2007*), but were also recorded in many other localities of the Northern Hemisphere and the tropics (*Schulz et al., 1998; Wang et al., 2001; Voelker and workshop participants, 2002; Dykoski et al., 2006*).

Greenland and the North Atlantic region developed interstadial conditions the so-called Dansgaard-Oeschger (D-O) events very abruptly within a few decades and with temperature increases by 8–16 °C (*Landais et al., 2004; Huber et al., 2006*). Afterwards temperatures decreased slowly and over centuries back to stadial conditions. Large discharges of icebergs were found in marine sediment cores from the North Atlantic (*Heinrich, 1988*). Stadial episodes during MIS 3 are characterized by these layered ice rafted debris ("Heinrich layers") in marine sediment cores and are called Heinrich events. These events have been accompanied by a strong reduction in sea surface temperature (*Bond et al., 1993*) and thus providing a link between changes in ocean circulation and surface climate (*Clark et al., 2002*). Freshwater input to the North Atlantic associated with Heinrich events is estimated to vary between 2 and 15 m of sea level equivalent

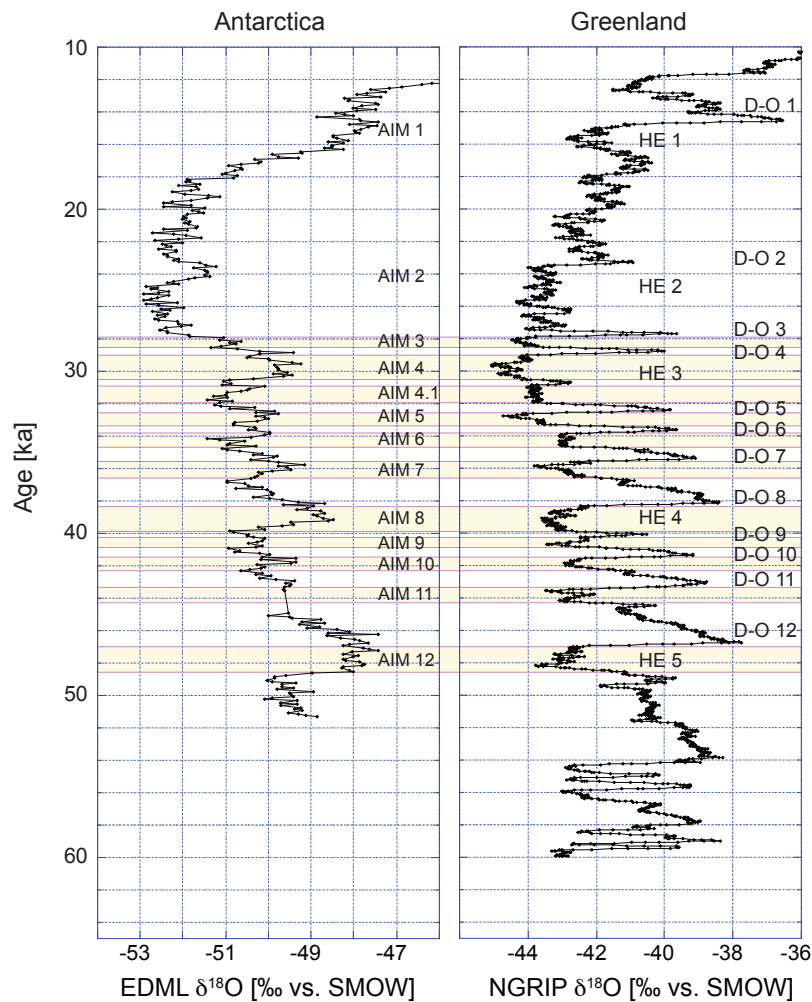


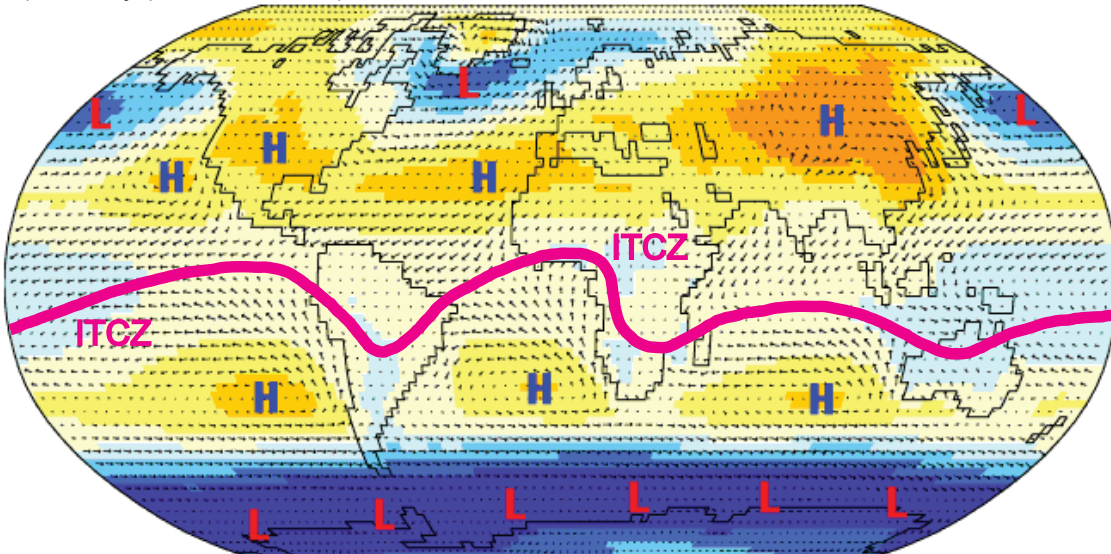
Figure 1.1 Methane synchronized oxygen isotope records of the EDML and NGRIP ice cores displayed on the GICC05 timescale. Shaded bars indicate Greenland stadial periods related to respective Antarctic temperature increases during MIS 3 (*EPICA Community Members, 2006*).

ice volume (*Chappell, 2002; Hemming, 2004*)

However, proxy data reflected warmings in the South Atlantic while North Atlantic cooled and vice versa (*Voelker and workshop participants, 2002*). A change in ocean heat transport is described as a seesaw of Northern and Southern Hemisphere temperatures (*Stocker and Johnsen, 2003*). This Northern and Southern Hemisphere bipolar seesaw has been firstly detected in ice core records from Greenland and Antarctica (*Broecker, 1998*). In contrast to Greenland rapid warmings and gradual coolings Antarctica experienced gradual increases and decreases in temperatures (*Johnsen et al., 1972; Jouzel et al., 1987; Blunier et al., 1998; Blunier and Brook, 2001*). Antarctic ice core records have been synchronized to those from Greenland using variations in the concentration of atmospheric methane as preserved in gaseous inclusions (*Blunier et al., 1998; Blunier and Brook, 2001*).

Position of the Intertropical Convergence Zone (ITCZ) sea-level pressure and surface winds

a) January (austral summer)



b) June (austral winter)

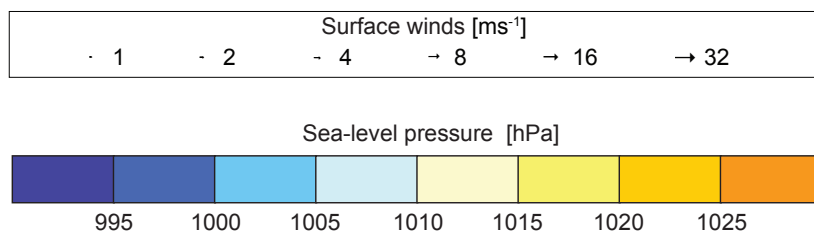
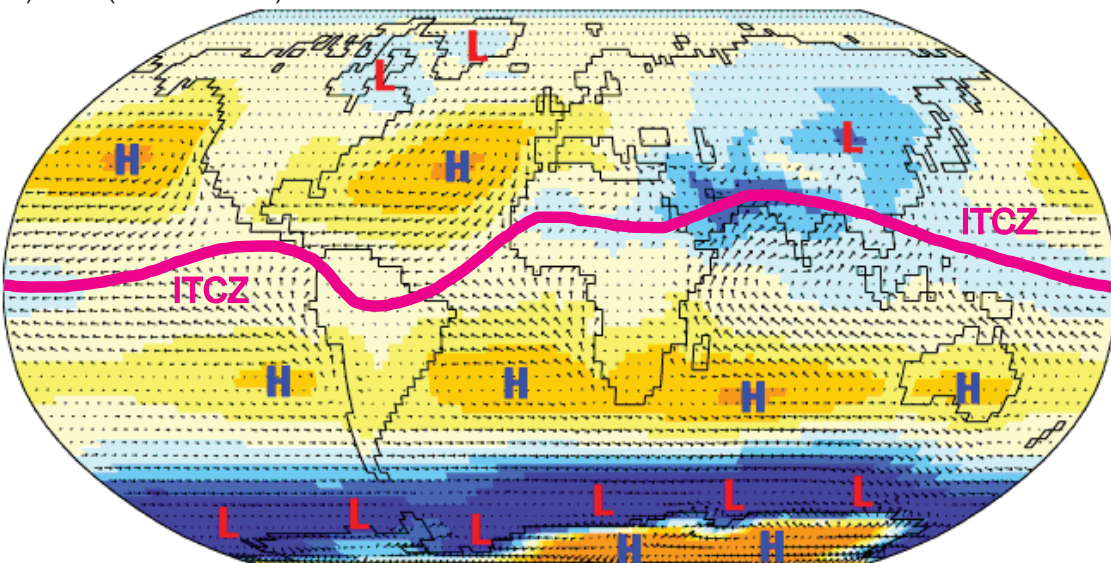


Figure 1.2 Position of the Intertropical Convergence Zone (ITCZ), surface winds and sea-level pressure based on NCEP/ NCAR Reanalysis data, 1959–1997 Climatologies modified after Citation: Pidwirny, M. (2006). "Global Scale Circulation of the Atmosphere". Fundamentals of Physical Geography, 2nd Edition. 18/05/2009. <http://www.physicalgeography.net/fundamentals/7p.html>

Additionally the Greenland Ice Core Chronology 2005 (GICC05) a new timescale based on high-resolution layer counts of the ice core from the North Greenland Ice core Project (NGRIP, *NGRIP members, 2004*) was developed (*EPICA Community Members, 2006; Andersen et al., 2006; Svensson et al., 2008*). High-resolution data of the EPICA Dronning Maud Land (EDML) ice core and the NGRIP ice core provided the basis for an one-to-one coupling between Antarctic Isotope Maxima (Antarctic warm events) and Greenland D-O interstadials (Figure 1.1). During the onset of an Antarctic warm event Greenland temperatures were still decreasing or constant (*Blunier et al., 1998; Blunier and Brook, 2001*). Model simulations explained the phase relation between temperatures in Greenland and Antarctica by a reduction in the North Atlantic Deep Water formation rate. The reduction produced a cooling in the North Atlantic and a lagged warming in the Southern Hemisphere (*Ganopolski and Rahmstorf, 2001*).

Many features of the abrupt changes are still not well constrained due to the sparsity of accurate data (*Jansen et al., 2007*) and the tendency of model simulations to underestimate past abrupt climate changes (*Alley et al., 2003*) and therefore possibly future ones. Some authors have argued that some of the abrupt climate shifts could have been triggered from the tropics (*Clement and Cane, 1999*). Climate variability in the tropics during MIS 3 is still poorly understood due to the scarcity of high-resolution marine archives. Sub-orbital changes during MIS 3 have been detected by high-resolution records in the northern part of the West Pacific Warm Pool (*Stott et al., 2002; Dannenmann et al., 2003*). These changes were related to increased South East Asian summer monsoon rainfall and warmer and fresher surface conditions in the West Pacific Warm Pool during Northern Hemisphere D-O interstadials. Studies of stalagmites support the idea of far-reaching Northern Hemisphere atmospheric circulation patterns on millennial timescale (*Wang et al., 2001; Burns et al., 2003; Ruth et al., 2007*). Furthermore there are evidences of a highly correlated variability of the Asian monsoon with other northern low-latitude records (*Dykoski et al., 2006*), but there is still a debate, whether a transhemispheric coupling between the South East Asian and Australian monsoon systems exists and how it may be related to high-latitude climate changes (*Wyrwoll and Miller, 2001; Wyrwoll and Valdes, 2003; Miller et al., 2005*). Monsoonal winds and precipitation are dependent on the migration of the intertropical convergence zone (ITCZ) the low pressure trough driven by solar heating (Figure 1.2). The inherent seasonality of monsoon circulation results in seasonal changes in atmospheric circulation and precipitation also affecting the ocean, leading to strong seasonality in current strength and direction, sea-surface temperature and salinity patterns (*Wang et al., 2005*).

1.1.3 Motivations for this study

Since millennial scale climate oscillations were identified in ice cores from Greenland (*Johnsen et al., 1992; Dansgaard et al., 1993; Grootes et al., 1993*), one major aim in climate research has been to gain insights into these D-O oscillations into their driving factors (*Voelker and workshop participants, 2002*). In contrast to the wealth of information concerning Atlantic Meridional Overturning Circulation slow-down and related regional climatic impacts during

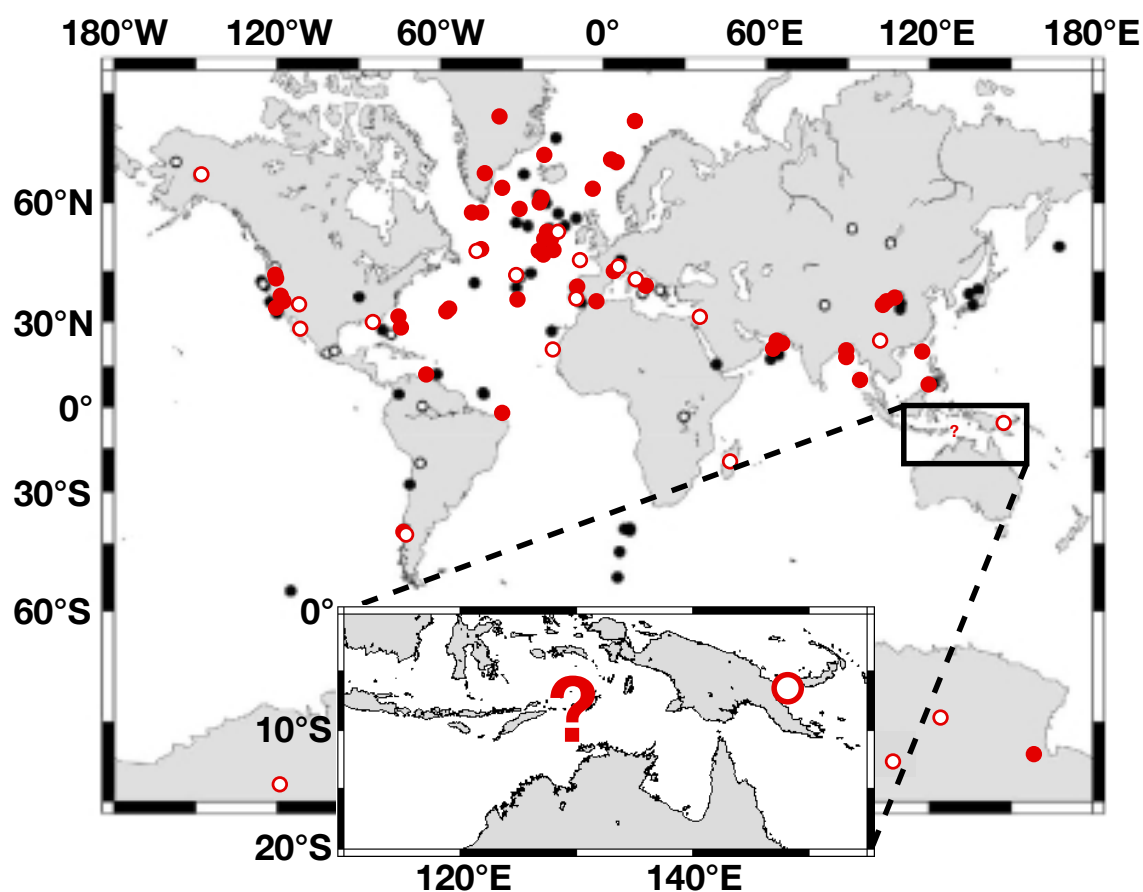


Figure 1.3 Spatial distribution of sites with resolutions of 1–200 yr (red dots and circles) and of 200–500 yr (black dots and circles) during MIS 3 after *Voelker and workshop participants (2002)*. Dots indicate sites with clear D-O type climate oscillations and circles those without or unclear D-O cyclicity

Heinrich events, relatively little is known about the response of a reduction in North Atlantic Deep Water formation on the thermohaline circulation in the Pacific and Indian Oceans. The global thermohaline circulation consists of a westward flow from the Pacific Ocean through the Indonesian Archipelago where this flow is 'transformed' to produce the Indonesian Throughflow (ITF). The tropical Indian Ocean surface water mass is mainly formed by ITF outflow water masses and therefore records from the ITF outflow are the key to understand the influence of D-O climate cycles in the Indian Ocean and Australian sector of the Southern Hemisphere. On the other hand the role of the tropics as a possible trigger for millennial scale climate variability remains still unclear and especially high-resolution records from the Indian Ocean and Australasian sector of the Southern Ocean are missing entirely (Figure 1.3). However, it remains unclear how far Greenland and Antarctica are representative for the entire hemispheres.

This study will assess the impact of the ITF on the hydrography of the eastern Indian Ocean and global thermohaline circulation during MIS 3. ITF fluctuations associated with sea level changes, temperature and salinity variations strongly influence regional climate. As a result precipitation

over Australia and the Indonesian Archipelago changes control the strength of the Australian summer and winter monsoon with possible effects on global climate.

Planktonic foraminiferal oxygen isotope and paleoproductivity studies based on benthic foraminiferal census counts in the outflow region of the ITF already indicated high variability in paleoproductivity during MIS 3 (*Holbourn et al., 2005*). Furthermore proxy records on glacial-interglacial timescales in the ITF outflow area and circulation models indicated reduced flow during cold intervals (*Müller and Opdyke, 2000; Kuhnt et al., 2004; Holbourn et al., 2005*). These authors related this reduced throughflow to lowered sea level and changes in local paleoceanographic and climatic boundary conditions. However, the time resolution of these studies did not allow detection of individual D-O events nor detailed correlation to high-latitude climate records during MIS 3.

High-resolution marine sediment Cores MD01-2378 and SO-185 18460 from the Timor Sea (Figure 1.4) will provide the detailed paleoceanographic framework that will be crucial to validate and refine circulation models of D-O events and high-frequency climate variability on a global scale.

1.1.4 Aims of this study

Using planktonic and benthic foraminiferal oxygen and carbon isotope values, benthic foraminiferal accumulation rates and Mg/Ca temperature estimates in this multi-proxy study we expect:

- to detect millennial scale fluctuations in marine sediment records from the tropical eastern Indian Ocean
- to monitor interhemispheric linkages between high- and low-latitude climate variability
- to estimate regional paleoproductivity patterns in the Timor Sea
- to determine regional paleoceanographic changes in the Timor Sea, and
- to monitor changes in the Asian-Australian monsoon system.

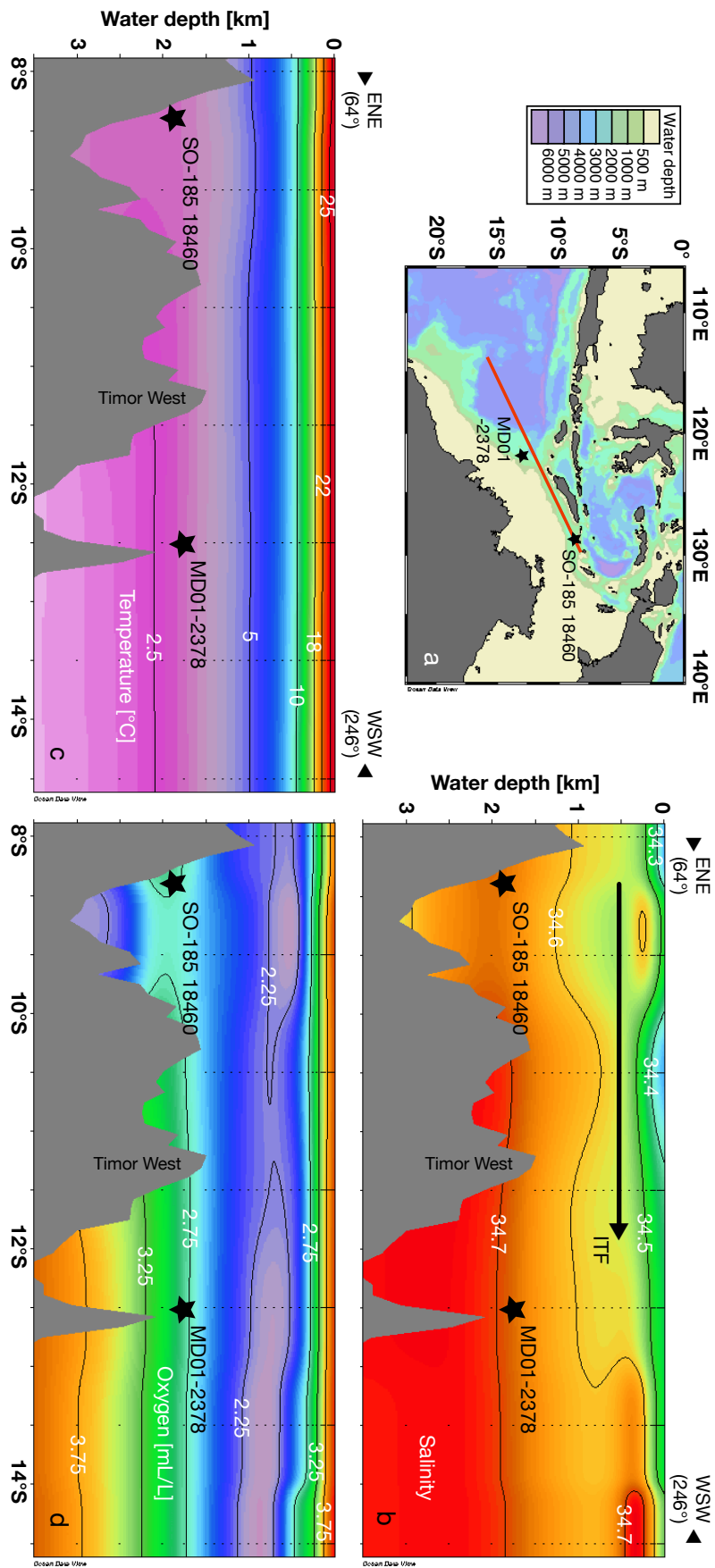


Figure 1.4 a) Map of the study area showing the locations of the Cores MD01-2378 (13°04.95' S and 121°47.27' E, 1783 m water depth) and SO-185 18460 (8° 47.386' S, 128° 38.485' E, 1875 m water depth) located in the Timor Sea. Along the red line, b) Salinity, c) Temperature [°C] and d) Oxygen concentration [mL L⁻¹] ENE-WSW profiles (National Oceanographic Data Center, *NODC*, 2001) are given to illustrate the modern conditions at the study sites. Annual data are obtained from the indicated 1x1° gridded positions (black dots) and plotted with Ocean Data View (*Schitzer*, 2002). Note that maximum sill depths at Leti Strait (ITF inflow into the Timor Sea, not illustrated in the profiles) and Timor West are ≈1250 m and ≈1890 m, respectively (*Sprintall et al.*, 2009). The upper branch of the Indonesian Throughflow (ITF) is indicated by a black arrow in b).

1.1.5 Structure of this thesis

- In Chapter 2 a high-resolution multi-proxy record spanning MIS 3 from Core MD01-2378 located in the Timor Sea off NW Australia is presented (Figure 1.4). Today, this area is influenced by the Intertropical Convergence Zone (Figure 1.2), which drives monsoonal winds during austral summer and by the main outflow of the ITF. Core MD01-2378 is ideally situated to monitor the linkages between tropical and high-latitude climate variability. Possible propagation of these climate signals, regional paleoceanographic and climate settings are discussed.
- In Chapter 3 high-resolution sea surface and upper thermocline temperature records of Core MD01-2378 are investigated (Figure 1.4). The study site reflects ITF variability during MIS 3, which is linked to global changes in Thermohaline Circulation, to sea level changes and to regional paleoceanography.
- In Chapter 4 high-resolution multi-proxy records from Core SO-185 18460 located in the Timor Passage and from Core MD01-2378 are compared to separate between high-latitude and regional climate signals. Differences in paleoceanographic settings and monsoonal influence between the main flow and outflow regions, respectively, are discussed.

Chapter 2

Centennial-Scale Climate Variability in the Timor Sea during Marine Isotope Stage 3

Anke Dürkop^a, Ann Holbourn^a, Wolfgang Kuhnt^a, Rina Zuraida^{a,b}, Nils Andersen^c, Pieter M. Grootes^c

^aInstitute of Geosciences, Christian-Albrechts-University, Ludewig-Meyn-Str. 10-14, D-24118 Kiel, Germany

^bLeibniz-Institute of Marine Sciences, IFM-GEOMAR, Wischhofstr. 1-3, D-24148 Kiel, Germany

^cLeibniz-Laboratory for Radiometric Dating and Stable Isotope Research, Christian-Albrechts-University, Max-Eyth-Str. 11 - 13, D-24118 Kiel, Germany

Published in *Marine Micropaleontology*, 66(2008)

doi:10.1016/j.marmicro.2007.10.002

Abstract. We present a high-resolution ($\approx 60\text{--}110$ yr) multi-proxy record spanning Marine Isotope Stage 3 from IMAGES Core MD01-2378 ($13^{\circ}04.95'$ S and $121^{\circ}47.27'$ E, 1783 m water depth), located in the Timor Sea, off NW Australia. Today, this area is influenced by the Intertropical Convergence Zone, which drives monsoonal winds during austral summer and by the main outflow of the Indonesian Throughflow, which represents a key component of the global thermohaline circulation system. Thus, this core is ideally situated to monitor the linkages between tropical and high latitude climate variability. Benthic $\delta^{18}\text{O}$ data (*Planulina wuellerstorfi*) clearly reflect Antarctic warm events (A1–A4) as recorded by the EPICA Byrd and Dronning Maud Land ice cores. This southern high latitude signal is transferred by deep and intermediate water masses flowing northward from the Southern Ocean into the Indian Ocean. Planktonic $\delta^{18}\text{O}$ shows closer affinity to northern high latitudes planktonic and ice core records, although only the longer-lasting Dansgaard-Oeschger warm events, 8, 12, 14, and 16–17 are clearly expressed in our record. This

northern high latitude signal in the surface water is probably transmitted through atmospheric teleconnections and coupling of the Asian-Australian monsoon systems. Benthic foraminiferal census counts suggest a coupling of Antarctic cooling with carbon flux patterns in the Timor Sea. We relate increasing abundances of carbon-flux sensitive species at 38–45 ka to the northeastward migration of the West Australian Current frontal area. This water mass reorganization is also supported by concurrent decreases in Mg/Ca and planktonic $\delta^{18}\text{O}$ values (*Globigerinoides ruber* white).

2.1 Introduction

One of the most fascinating and enigmatic findings of paleoclimate research is the succession of extremely rapid and large-amplitude climate fluctuations during the last glacial period: the so called Dansgaard-Oeschger (D-O) events. These dramatic climate events are most clearly seen in Greenland ice cores (*Johnsen et al., 1992; Dansgaard et al., 1993; Grootes et al., 1993*) and in sediment cores from the adjacent North Atlantic, but were also recorded in many other localities of the Northern Hemisphere (*Voelker and workshop participants, 2002*). The most rapid shifts occurred during Marine Isotope Stage 3 (MIS 3) from cool stadial to warm interstadial conditions in the North Atlantic region (D-O warm events) with temperatures rising by 8–16 °C (*Landais et al., 2004; Huber et al., 2006*) within a few decades followed by a gradual temperature decrease back to stadial conditions within approximately 1500 yr. In contrast, the Southern Hemisphere experienced slower millennial changes with moderate temperature fluctuations of approximately 1–3 °C (*Watanabe et al., 2003; EPICA Community Members, 2004*). Climate models and paleoceanographic records suggest that when Greenland warmed during D-O events the North Atlantic sea surface warmed, trade winds strengthened and the Asian monsoon intensified (*Voelker and workshop participants, 2002; Ruth et al., 2007*).

In the tropics climate variability during MIS 3 is still poorly understood due to the scarcity of high-resolution marine archives. Distinct, sub-orbital scale $\delta^{18}\text{O}$ changes during MIS 3 in the northern part of the West Pacific Warm Pool (WPWP) were detected in high-resolution records from the Mindanao Eddy and Sulu Sea (*Stott et al., 2002; Dannenmann et al., 2003*). These changes were related to increased South East Asian summer monsoon rainfall and warmer and fresher surface conditions in the WPWP during Northern Hemisphere interstadials. It remains an open question, whether such changes also affected the Southern Hemisphere part of the SE Asian tropics, in particular northern Australia and the northeastern Indian Ocean, where high-resolution records of glacial climate variability are still missing or contradictory during MIS 3. There is, for instance, considerable debate concerning the transhemispheric coupling between the South East Asian and Australian monsoon systems and their relation to high latitude climate change (*Wyrwoll and Miller, 2001; Wyrwoll and Valdes, 2003; Miller et al., 2005*).

A further major influence on the climate of the Indonesian-Australian region is the intensity of surface water flow from the Pacific into the Indian Ocean (=Indonesian Throughflow, ITF).

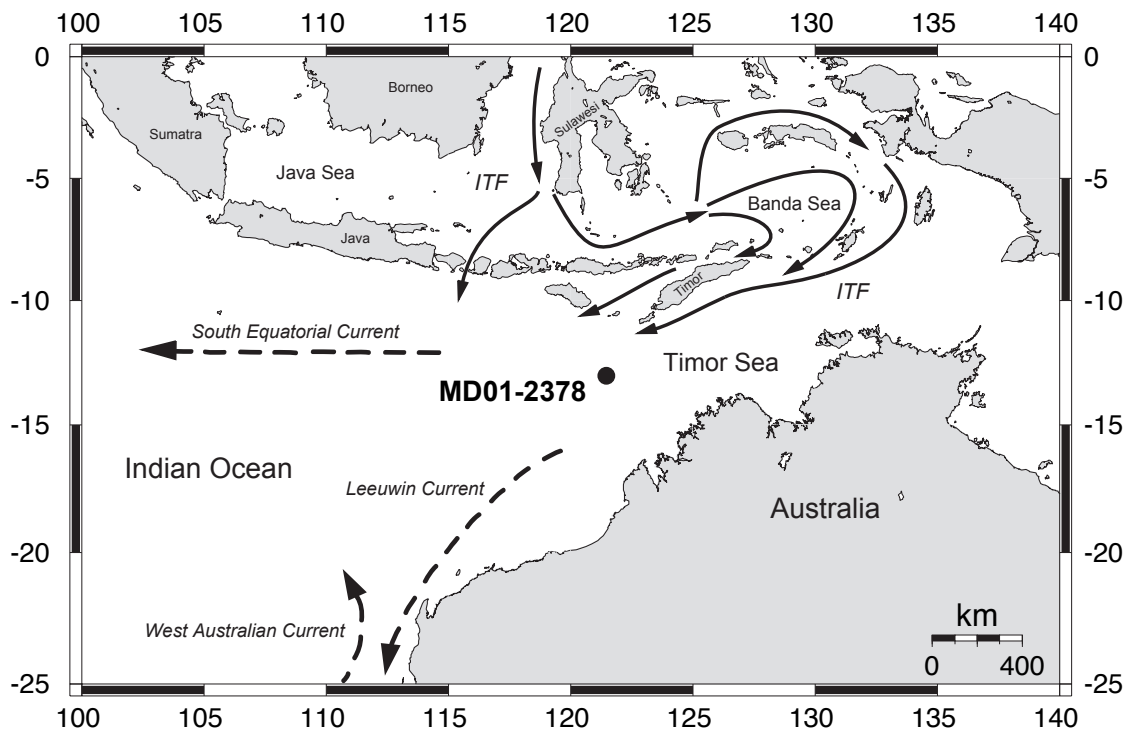


Figure 2.1 Location of Core MD01-2378 ($13^{\circ}04.950' \text{ S}$, $121^{\circ}47.270' \text{ E}$, water depth: 1783 m) in the Timor Sea. Solid arrows indicate main pathways of the Indonesian Throughflow (=ITF, after [Gordon, 2005](#)). Dashed arrows indicate the South Equatorial Current, Leeuwin Current and West Australian Current.

At the onset of Greenland interstadials D-O 5, 8, 12, 14 and 17, substantial sea-level highstands (+9 to 26 m) were recorded in coral terraces at Huon Peninsula in Papua New Guinea ([Chappell, 2002](#)). Similar magnitudes of sea-level fluctuations during MIS 3 were reported from the Red Sea ([Siddall et al., 2003](#)), where the magnitude of sea-level fluctuations during MIS 3 reached 35 ± 12 m, which is comparable to the maximum values of 26 m estimated by [Chappell \(2002\)](#) from coral reef data. Proxy records on glacial-interglacial timescales in the ITF outflow area and circulation models indicated reduced flow during cold intervals ([Müller and Opdyke, 2000](#); [Kuhnt et al., 2004](#); [Holbourn et al., 2005](#)). These authors related this reduced throughflow to lowered sealevel and changed local paleoceanographic and climatic boundary conditions (i.e. reduced precipitation and higher salinity in the central part of the WPWP or differing monsoonal wind patterns). Planktonic foraminiferal oxygen isotope and paleoproductivity studies in the outflow region of the ITF already indicated high variability during MIS 3 ([Holbourn et al., 2005](#)). However, the time resolution of these studies did not allow detection of individual D-O events nor detailed correlation to high latitude climate records during this interval of rapid climate change.

Here, we present a centennial-scale resolution multi-proxy record spanning MIS 3 from IMAGES Core MD01-2378, located in the tropical eastern Indian Ocean between Indonesia and Australia. This core is situated close to the main outflow of the ITF, and is also influenced by the

Asian-Australian monsoon system, which induces strong seasonal changes in atmospheric deep convection and local wind and precipitation patterns. Thus, this core is ideally placed to investigate regional climate variability in relation to thermohaline circulation changes and to assess linkages between high latitude and tropical climate evolution.

2.2 Material and method

2.2.1 Paleoceanographic setting

IMAGES Core MD01-2378 (13°04.95' S, 121°47.27' E, water depth: 1783 m) was recovered in May 2001 at the northwestern margin of the Scott Plateau in the Timor Sea (Figure 2.1). Core MD01-2378 is located close to the oceanographic front between relatively cool, saline water carried northward by the West Australian Current (WAC) and warm, fresh water from the ITF partly feeding the South Equatorial Current (SEC) and the Leeuwin Current (LC), which continues southward along the West Australian coast and is mainly active during austral autumn and winter (Godfrey and Weaver, 1991; Tomczak and Godfrey, 2003; Peter et al., 2005). Today, tropical water masses clearly dominate at the coring site resulting in warm (≈ 29.5 °C and ≈ 27.5 °C), low-saline (≈ 34.1 psu and ≈ 34.4 psu) surface water, and a deep thermocline (=18 °C isotherm, 170 m) (May 2001 and September 2005 CTD data given by Bassinot et al., 2002 and Kuhnt, 2005) with low nutrient levels and a deep chlorophyll maximum (Longhurst, 1998). However, this situation may have been fundamentally changed towards stronger influence of the WAC during glacial times, when the NW Australian shelf was exposed, the ITF reduced, and the LC weakened (Wells and Wells, 1994; Kuhnt et al., 2004; Holbourn et al., 2005).

2.2.2 Stable isotopes

Samples (30–40 cm³ from 1 cm thick sediment slices) were taken at 1 cm interval between 448 and 895 cm in Core MD01-2378. Samples were dried and weighed, then washed over a 63 μm sieve. Residues were dried on a sheet of filter paper and weighed, then sieved into 63–150 μm , 150–250 μm , 250–315 μm , and >315 μm fractions. For stable isotope analysis, we selected 3 to 8 tests (>250 μm) of the epibenthic foraminifera *Planulina wuellerstorfi* and 20 tests (250–315 μm) of the planktonic foraminifera *Globigerinoides ruber* (white). In a few samples, where benthic foraminiferal density was low, a smaller number (1–2) of specimens were analyzed. Tests were checked for cement encrustations and infillings before being broken into large fragments, then cleaned in ethanol in an ultrasonic bath and dried at 40 °C. Stable carbon and oxygen isotope measurements were made with the Finnigan MAT 251 mass spectrometer at the Leibniz Laboratory, University of Kiel. The instrument is coupled online to a Carbo-Kiel Device (Type I) for automated CO₂ preparation from carbonate samples for isotopic analysis. Samples were reacted by individual acid addition. The mean external error and reproducibility of carbonate standards is better than $\pm 0.07\text{‰}$ and $\pm 0.05\text{‰}$ for $\delta^{18}\text{O}$ and $\delta^{13}\text{C}$, respectively. Results were calibrated using the National Institute of Standards and Technology (Gaithersburg, Maryland)

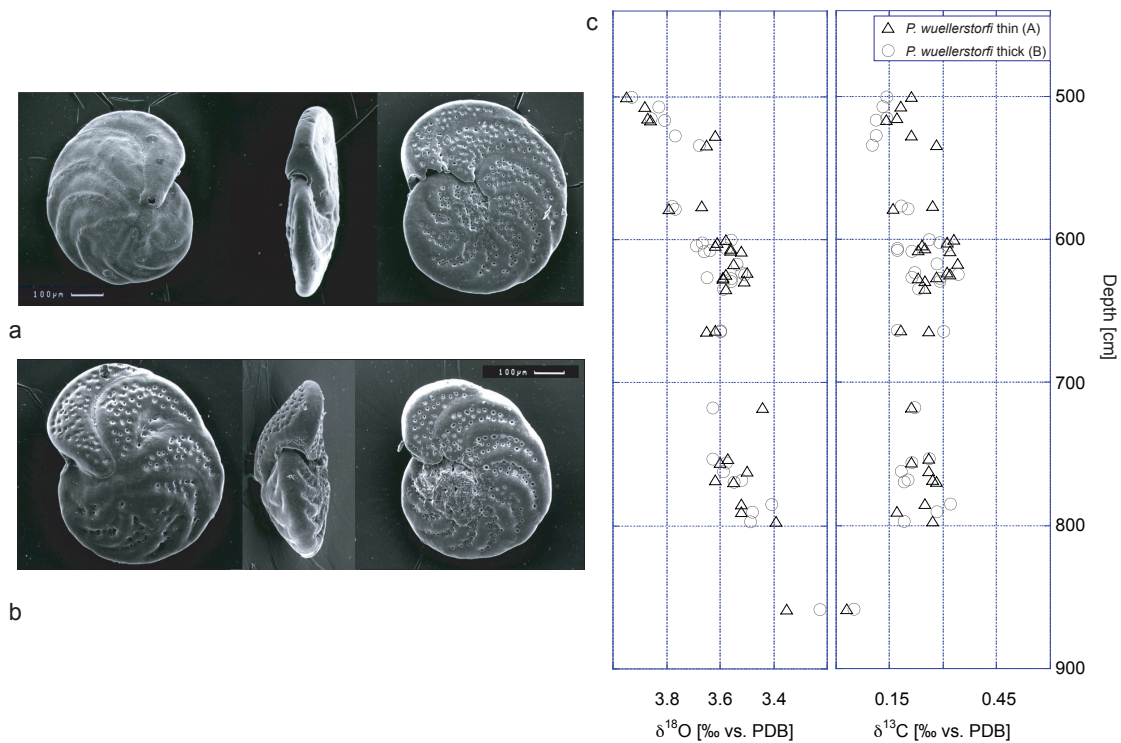


Figure 2.2 Scanning electron micrographs of two morphotypes of the epibenthic foraminifera *P. wuellerstorfi*. a) Morphotype A: flat in cross-section with thinner wall; b) morphotype B: plano-convex in cross-section with thicker wall. Umbilical, apertural and spiral views of morphotypes A and B are from different specimens; c) Paired stable isotope measurements on morphotypes A (triangles) and B (circles) in Core MD01-2378. Reproducibility between the two morphotypes is better than $\pm 0.06\text{‰}$ and $\pm 0.05\text{‰}$ for $\delta^{18}\text{O}$ and $\delta^{13}\text{C}$, respectively

carbonate isotope standard NBS 20 and in addition NBS 19 and 18, and are reported on the PeeDee belemnite (PDB) scale.

We recognized two different morphotypes of *P. wuellerstorfi*: morphotype A is generally flatter in cross-section and has a thinner wall, whereas morphotype B has a more plano-convex cross-section and thicker wall (Figure 2.2). Most of our measurements were performed on *P. wuellerstorfi* A, except in ten samples, where this morphotype was rare, and *P. wuellerstorfi* B was measured. We determined from 33 paired samples that there is no statistically significant difference between morphotypes A and B of *P. wuellerstorfi* (reproducibility is better than $\pm 0.06\text{‰}$ and $\pm 0.05\text{‰}$ for $\delta^{18}\text{O}$ and $\delta^{13}\text{C}$, respectively). Replicate measurements on 51 paired samples of *P. wuellerstorfi* A indicated that the mean reproducibility is better than $\pm 0.06\text{‰}$ and $\pm 0.04\text{‰}$ for $\delta^{18}\text{O}$ and $\delta^{13}\text{C}$, respectively. For the planktonic foraminifera *G. ruber* (white), the reproducibility is better than $\pm 0.08\text{‰}$ for $\delta^{18}\text{O}$ and $\delta^{13}\text{C}$ in 49 paired measurements.

The difference in $\delta^{13}\text{C}$ between planktonic and benthic foraminifera ($\Delta\delta^{13}\text{C}_{(PF-BF)}$) has been used for qualitative estimates of export productivity in tropical and subtropical oceans (Sarnthein and Winn, 1977; Jian et al., 2001; Holbourn et al., 2005), even though additional

complex factors are influencing the $\delta^{13}\text{C}$ profiles in the ocean, including mixing rates and exposure time of surface waters to the atmosphere. However, in the extended, low-resolution MD01-2378 time series (Holbourn *et al.*, 2005), the $\Delta\delta^{13}\text{C}_{(PF-BF)}$ curve exhibits striking similarities to other productivity proxy records and thus, probably reflects productivity changes in near-surface waters at this site.

2.2.3 Accelerator mass spectrometry

For accelerator mass spectrometry (AMS) ^{14}C dating, approximately 1500 well preserved tests of the planktonic foraminifera *G. ruber* (white) were picked from the $>250\ \mu\text{m}$ fraction at levels, where *G. ruber* showed maximum abundance, to minimize the proportion of tests displaced by bioturbation. AMS conventional ^{14}C ages (Table 2.1) were determined at the Leibniz-Laboratory, University of Kiel, using standard methods described by Nadeau *et al.* (1997) and Schleicher *et al.* (1998). Calendar ages were calculated with the radiocarbon calibration program from Fairbanks *et al.* (2005) (<http://www.radiocarbon.ldeo.columbia.edu/research/radiocarbon.htm>), after applying a reservoir age correction of 300 yr (Butzin *et al.*, 2005).

2.2.4 Benthic foraminiferal census counts

An average of 150 benthic foraminifera were picked and counted in size fractions $>250\ \mu\text{m}$ following the approach of Holbourn *et al.* (2005). In samples, where benthic foraminiferal abundance was high, a quantitative split of the $>250\ \mu\text{m}$ size fractions was picked, and census counts were then reconverted to whole samples. Counts of globocassidulinids include *Globocassidulina subglobosa* and *Globocassidulina elegans*. Buliminids counts include *Globobulimina spp.*, *Bulimina aculeata*, *Bulimina marginata* and *Bulimina mexicana* (see Taxonomic list A). Low-resolution counts from Holbourn *et al.* (2005) were integrated with our high-resolution counts.

Benthic foraminiferal accumulation rates (BFAR: number of specimens $>250\ \mu\text{m}\ \text{cm}^{-2}\ \text{kyr}^{-1}$) were calculated as the product of the number of benthic foraminifera per gram dry sediment and the sediment accumulation rate (in $\text{g}\ \text{cm}^{-2}\ \text{kyr}^{-1}$). Accumulation rates (AR) of buliminids

Table 2.1 AMS ^{14}C dates measured on *G. ruber* (white) in Core MD01-2378

| Lab Code | Sample (Core MD01-2378) | ^{14}C -Conventional age (BP) | CAL-age (BP) |
|-----------|-------------------------|--|-----------------|
| KIA 19611 | 316.5cm, 1.0 mg C | 14260 \pm 70 | 16280 \pm 150 |
| KIA 19612 | 338.5cm, 1.2 mg C | 15410 \pm 70 | 18310 \pm 160 |
| KIA 19613 | 364.5cm, 1.0 mg C | 16340 \pm 80 | 19170 \pm 110 |
| KIA 19614 | 390.5cm, 1.0 mg C | 17440 \pm 90 | 20320 \pm 100 |
| KIA 19615 | 424.5cm, 1.1 mg C | 18990 \pm 100 | 22300 \pm 100 |
| KIA 19616 | 440.5cm, 1.0 mg C | 19960 \pm 110 | 23490 \pm 170 |
| KIA 31094 | 500.0cm, 1.2 mg C | 23210 \pm 170 | 27510 \pm 240 |
| KIA 31095 | 534.0cm, 1.1 mg C | 24970 \pm 210 | 29530 \pm 320 |
| KIA 19617 | 591.5cm, 1.1 mg C | 29920 + 330 / -310 | 35040 \pm 350 |
| KIA 31096 | 642.0cm, 1.1 mg C | 34560 + 650 / -600 | 39630 \pm 650 |
| KIA 31785 | 683.0cm, 1.4 mg C | 35660 + 750 / -690 | 40670 \pm 720 |

and globocassidulinids were calculated in the same fashion. We calculated sediment accumulation rates based on sedimentation rates derived from the age model and dry bulk density values (g cm^{-3}) (*van Andel et al., 1975*). Dry bulk density values were determined every 20 cm of the core from discrete samples taken with a metal tube of 10 cm^3 inner volume and a 9 pt running average smooth was used to avoid artificial fluctuations in mass accumulation rates (*Holbourn et al., 2005*). The resulting values show only a small scatter between 0.6 and 0.7 g cm^{-3} for the studied interval.

2.3 Results

2.3.1 Age model

Our age model is based on the correlation of high-resolution benthic oxygen isotope data to the new EDML ice core recovered from the interior of Dronning Maud Land within the European Project for Ice Coring in Antarctica (*EPICA Community Members, 2004*). This ice core has been synchronized to the layer counted NGRIP ice core following the new Greenland Ice Core Chronology (GICC05) timescale (*EPICA Community Members, 2006; Andersen et al., 2006*). Between 15 and 48 ka six tie points were used to correlate MD01-2378 and EDML (Figures 2.3–2.5; Table 3.2). An interpolated curve was fitted through the tie points using a Stineman function in Kaleidagraph Version 4, and the curve was then sampled. A change in sedimentation rates from ≈ 11 to $\approx 16 \text{ cm kyr}^{-1}$ is evident at a depth of about 554 cm (≈ 30 ka). This change is most probably caused by sediment oversampling in the upper part of the core during the piston coring process (*Sz er em eta et al., 2004; Holbourn et al., 2005*). As no isotopic data are published beyond 50 ka for the EDML ice core, the lower part of our age model (740–895 cm corresponding to 47–64 ka) is based on linear extrapolation. Comparison of MD01-2378 planktonic $\delta^{18}\text{O}$ with NGRIP (Figure 2.5) fully supports this linear extrapolation.

Eleven AMS dates including 7 dates from *Holbourn et al. (2005)* provide additional constraint for our age model (Figure 2.4, Table 2.1). However, within this interval the earth magnetic field showed several episodes of weakness leading to increased production of cosmogenic isotopes and resulting in occurrence of ^{14}C -plateaux, such as the Laschamp Event at around 41 ka (*Voelker et al., 2000; Hughen et al., 2004*).

Table 2.2 Tie points between benthic foraminiferal $\delta^{18}\text{O}$ and EDML ice core $\delta^{18}\text{O}$ versus depth and age

| Core MD01-2378 | | EDML ice core | | Event |
|----------------|-----------------------------------|--------------------|------------------------------------|---|
| Depth [cm] | $\delta^{18}\text{O}$ [‰ vs. PDB] | GICC05 age [ka BP] | $\delta^{18}\text{O}$ [‰ vs. SMOW] | |
| 342 | 3.92 | 18.15 | -51.89 | $\delta^{18}\text{O}$ maximum prior to deglaciation |
| 506 | 3.92 | 27.45 | -52.53 | $\delta^{18}\text{O}$ maximum after AIM 4 event |
| 554 | 3.72 | 30.65 | -51.04 | $\delta^{18}\text{O}$ maximum before AIM 4 event |
| 642 | 3.31 | 38.15 | -48.68 | Last $\delta^{18}\text{O}$ minimum of A1 event |
| 664 | 3.65 | 39.85 | -50.91 | $\delta^{18}\text{O}$ maximum before A1 event |
| 742 | 3.28 | 47.25 | -47.44 | $\delta^{18}\text{O}$ minimum in center of A2 event |

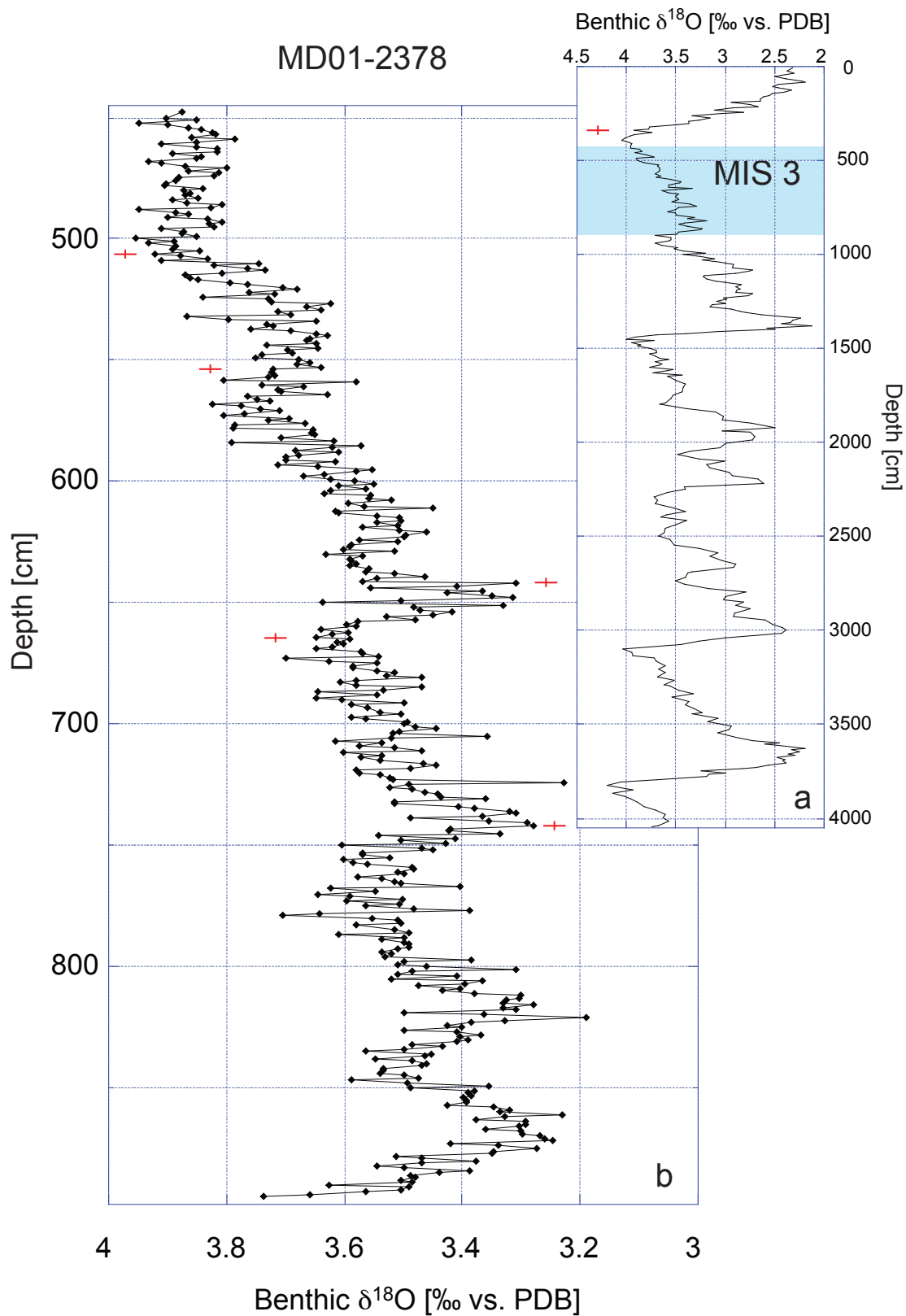


Figure 2.3 a) Benthic foraminiferal oxygen isotope data versus depth spanning MIS 1-12 from *Holbourn et al. (2005)*; b) and centennial-scale resolution record spanning MIS 3 (this study). Crosses indicate tie points between Core MD01-2378 and the EDML ice core used as basis for MIS 3 age model

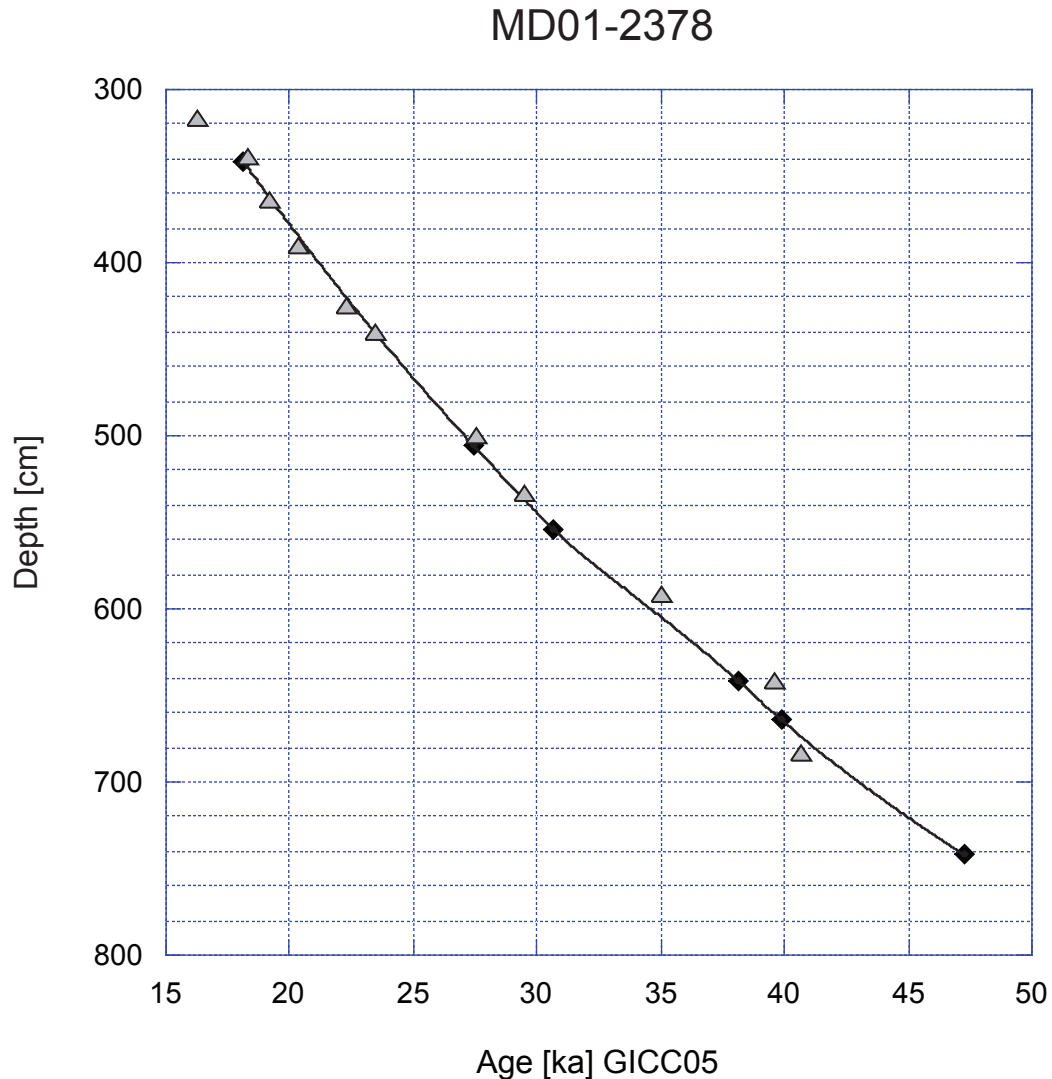


Figure 2.4 Age/depth plot showing tie points (diamonds) between EDML ice core and MD01-2378 benthic foraminiferal $\delta^{18}\text{O}$. Our age model is further constrained by 11 AMS ^{14}C dates (triangles).

Significant changes in thermohaline circulation intensity occurred during this time interval, in particular during Heinrich events (*NGRIP members, 2004*). Hence, most of the conditions for constant marine reservoir ages do not hold (*Grootes and Sarnthein, 2006; Sarnthein et al., 2007*), and the calibration of AMS ^{14}C dates and the estimation of reservoir ages for MIS 3 are not straightforward. The AMS ^{14}C dates show relatively good correlation to the EDML tie points between 18 and 47 ka (Figure 2.4). However, converted calendar ages show more pronounced deviations between 27 and 40 ka, due to increasing uncertainty in the Fairbanks calibration curve prior to 29 ka (*Svensson et al., 2006*). This problem is additionally compounded by the occurrence of the Mono Lake event at 34 ka (*Hughen et al., 2004*).

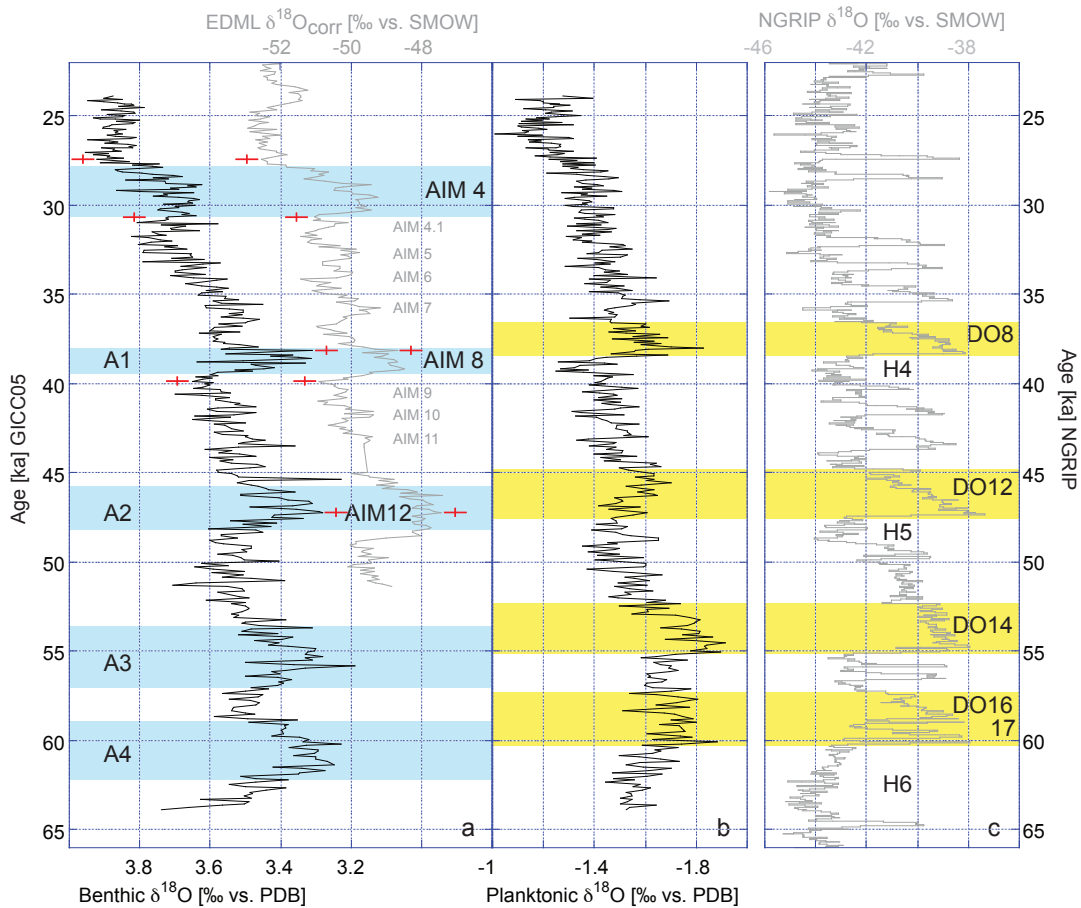


Figure 2.5 a) Benthic foraminiferal $\delta^{18}\text{O}$ (*P. wuellerstorfi*) in Core MD01-2378 and $\delta^{18}\text{O}$ in EDML ice core versus age. Crosses indicate tie points between $\delta^{18}\text{O}$ records. Antarctic warm events (A1–A4) and Antarctic Isotope Maxima (AIM4, AIM8 and AIM12) indicated by shaded bars; b) and c) Comparison of MD01-2378 planktonic foraminiferal $\delta^{18}\text{O}$ with Greenland ice core $\delta^{18}\text{O}$; only longer-lasting D-O warm events (shaded) are clearly expressed in the MD01-2378 planktonic record.

2.3.2 Stable isotopes

Benthic and planktonic foraminiferal $\delta^{18}\text{O}$ records indicate complete recovery of a continuous hemipelagic sedimentary succession between 22 and 64 ka, spanning the entire MIS 3 with a time resolution of ≈ 60 – 110 yr (Figure 2.5). The benthic $\delta^{18}\text{O}$ record varies between ≈ 3.9 – 3.2 ‰ exhibiting a maximum amplitude fluctuation of 0.7 ‰. Most prominent features in the older part of the record are the four distinct excursions to lower $\delta^{18}\text{O}$ with an amplitude fluctuation of 0.3 ‰ at ≈ 62 ka, ≈ 55 ka, ≈ 46 ka and ≈ 38 ka, which we correlate to Antarctic warm events A1–A4 (Figure 2.5a). The upper part of the time series is characterized by two gradual increases in $\delta^{18}\text{O}$ values: Step 1 occurs between 38.0–31.0 ka with an increase from 3.5 ‰ to 3.8 ‰. After a minor decrease of about 0.2 ‰, step 2 takes place between 31.0–26.5 ka with an increase from 3.7 ‰ to 3.9 ‰.

The benthic $\delta^{13}\text{C}$ record (Supplementary Figure ??) exhibits an overall variability of 0.4‰. $\delta^{13}\text{C}$ values show an increase of about 0.2‰ between 59–51 ka, then vary between 0.2‰ and 0.3‰ until 29 ka. The younger record (29–24 ka) shows an increasing trend from 0.2‰ and 0.1‰.

Planktonic foraminiferal $\delta^{18}\text{O}$ values vary between $\approx 1.0\text{‰}$ and $\approx 1.9\text{‰}$ over the entire record (Figure 2.5b). In general, three main trends are observed. In the lower part before 55 ka, $\delta^{18}\text{O}$ values decrease from $\approx 1.5\text{‰}$ to $\approx 1.9\text{‰}$. Between 55 and 39 ka, planktonic $\delta^{18}\text{O}$ increases to $\approx 1.3\text{‰}$. After a rapid decrease in planktonic $\delta^{18}\text{O}$ to $\approx 1.8\text{‰}$ at 38.0 ka, an overall increase of 0.6‰ occurs until 26 ka, followed by a slight decrease in values. The planktonic $\delta^{13}\text{C}$ record shows a maximum amplitude fluctuation of 0.6‰ (Supplementary Figure ??). The lower part (64–59 ka) is characterized by the lowest $\delta^{13}\text{C}$ values around 1.2‰ increasing after 59 ka to an almost constant level of about 1.5‰.

2.3.3 Benthic foraminiferal census counts

Robust methods to estimate carbon flux and paleoproductivity using benthic foraminifera include BFAR (Herguera and Berger, 1991; Herguera, 2000) and the accumulation rates and relative abundances of organic flux indicator species such as buliminids (Lutze and Coulbourn, 1984; Altenbach and Sarnthein, 1989; Thomas and Gooday, 1996; Jian et al., 1999; Holbourn et al., 2005). Figure 2.6 documents BFAR variations and the distribution of organic flux indicator taxa (buliminids and globocassidulinids) in relation to benthic and planktonic $\delta^{18}\text{O}$. The number of buliminids per gram shows a clear positive correlation to benthic $\delta^{18}\text{O}$. Such covariance was already evident in the low-resolution benthic foraminiferal and $\delta^{18}\text{O}$ records from the same core spanning the last 460 ka, published by Holbourn et al. (2005). In our high-resolution records, the number of buliminids increases to ≈ 2.5 specimens per gram (or an accumulation rate of ≈ 26 individuals $\text{cm}^{-2} \text{kyr}^{-1}$) during stadials and decreases to ≈ 0.5 specimens per gram (or an accumulation rate of ≈ 5 individuals $\text{cm}^{-2} \text{kyr}^{-1}$) during interstadials. Globocassidulinids show marked variations in number (from ≈ 1 to 12 specimens per gram or an accumulation rate of ≈ 10 –110 individuals $\text{cm}^{-2} \text{kyr}^{-1}$) and represent up to half of the total benthic foraminiferal assemblage. The distribution of globocassidulinids exhibits four prominent increases between 60 and 39 ka. Three of the peaks coincide with A4–A2 event, whereas the last and most sustained increase at 43–39 ka is not directly correlated to the A1 event.

The total number of benthic foraminifera per gram varies from 4 to 24 (or an accumulation rate of ≈ 50 –200 individuals $\text{cm}^{-2} \text{kyr}^{-1}$). Although globocassidulinids provide the stronger imprint on benthic foraminiferal distribution, the number of buliminids per gram also significantly affects total abundances (see for instance, at 27–28 ka). However, the main increases in the number of specimens between ≈ 60 and 39 ka generally reflect marked rises in the numbers of globocassidulinids.

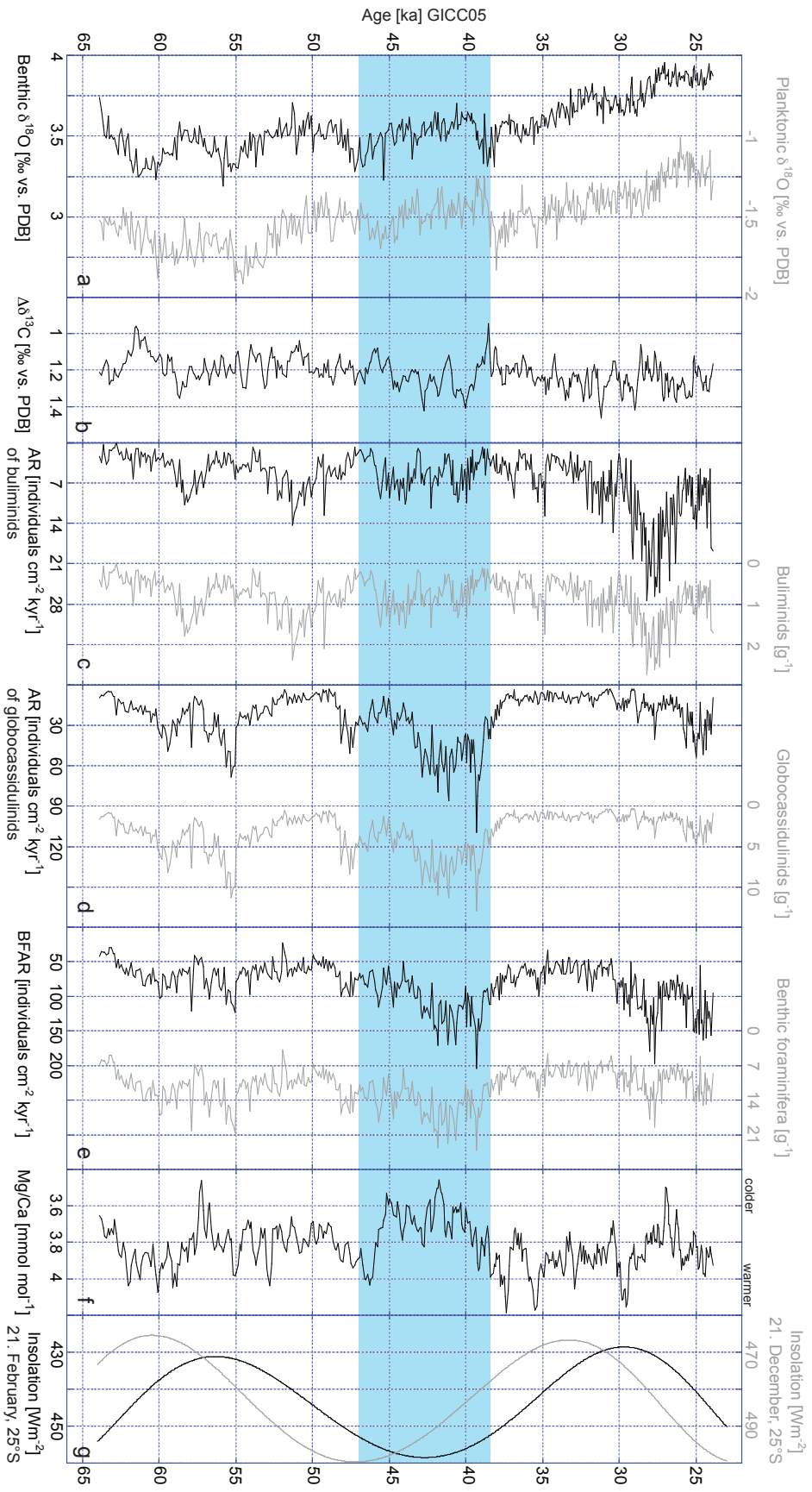


Figure 2.6 a) Benthic and planktonic $\delta^{18}\text{O}$; b) $\Delta\delta^{13}\text{C}$ obtained by subtracting $\delta^{13}\text{C}$ benthic from $\delta^{13}\text{C}$ planktonic; c-e) Accumulation rates (black) and census counts (grey) of benthic foraminifera, globocassidulids and total benthic specimens; f) Mg/Ca measured on *G. ruber* (white) (Zuraida et al., 2009, see Chapter 3); g) December (grey) and February (black) insolation at 25° S, February maximum insolation at 25° S is shaded

2.4 Discussion

2.4.1 Northern and Southern Hemisphere climate control

A striking feature in the Core MD01-2378 records from the Timor Sea is the contrast between the benthic and planktonic oxygen isotope signals (Figure 2.5). The benthic $\delta^{18}\text{O}$ record captures Antarctic cooling and warming trends, including warm events A1 to A4 in the Byrd ice core following the nomenclature of *Blunier and Brook (2001)* and Antarctic Isotope Maximum 4 (AIM4) in the EDML ice core following the nomenclature of the EPICA Community members (2006). However, during times of gradual warming in the Southern Hemisphere as shown by the MD01-2378 benthic $\delta^{18}\text{O}$, the planktonic isotope data indicate cooling. Thus, planktonic $\delta^{18}\text{O}$ shows closer affinity to northern high latitudes planktonic and ice core records, although only the longer-lasting D-O warm events 8, 12, 14, and 16–17 are clearly expressed in the MD01-2378 core (Figure 2.5). This phase relationship between warming and cooling events in the Southern and Northern Hemispheres, previously detected in ice cores and Northern Hemisphere sediment cores, was interpreted as a bipolar climate seesaw, as Northern Hemisphere cooling is balanced by Southern Hemisphere warming (*Broecker, 1998*). *Shackleton et al. (2000)* and *Martrat et al. (2007)* described a clear out-of-phase relationship for Cores MD95-2042, MD01-2444 and MD01-2443 from the Iberian Margin, where the onsets of warm events in benthic $\delta^{18}\text{O}$ lead rapid cold-to-warm transitions in planktonic $\delta^{18}\text{O}$. Benthic $\delta^{18}\text{O}$ values from the Iberian Margin display an Antarctic temperature signal, whereas planktonic $\delta^{18}\text{O}$ values reflect Greenland temperature variations. *Martrat et al. (2007)* suggested, that benthic $\delta^{13}\text{C}$ values reflected the mixing of southern and northern sourced deep-water masses. In particular, depleted benthic $\delta^{13}\text{C}$ values coinciding with high planktonic $\delta^{18}\text{O}$ document dominance of Antarctic Bottom Water in the North Atlantic.

An interesting hypothesis to explain rapid climate changes during MIS 3 was proposed by *Adkins et al. (2005)*. These authors suggested that during slowdowns of the Meridional Overturning Circulation (MOC) bottom water is increasingly warmed by geothermal heat in a more stratified deep ocean, eventually leading to instability in stratification and re-start of northern deep-water formation. During MOC re-acceleration heat would be released to the atmosphere in the Southern Ocean, driving the ice core record. According to *Adkins et al.*'s hypothesis, the warming should be confined to bottom water, whereas warming in much of the water column should occur with the ingression of warmer southern sourced intermediate and deep waters ("bipolar seesaw" hypothesis). Our benthic $\delta^{18}\text{O}$ data from Core MD01-2378 at 1783 m water depth show warming during slowdowns of the MOC associated with Heinrich events 4–6 (Figure 2.5), which implies that warming extended to much of the water column in accordance with the bipolar seesaw hypothesis. The Southern Hemisphere signal in the MD01-2378 benthic oxygen isotope record is probably transmitted through the transfer of deep and intermediate water masses towards the Timor Sea. Data analysis and numerical models suggest that today the major formation region for Antarctic Intermediate Water is in the southeastern Pacific (*McCartney, 1977*; *England, 1992*) and that these waters flow eastward through the Drake Passage along the Antarctic

Circumpolar Current towards the Indian Ocean. The deep water enters the Indian Ocean through the South-Australian-Basin, flows further north into the West-Australian-Basin into the Central-Indian-Basin (*McCorkle et al.*, 1998). Radiocarbon ages of deep water indicate that the transfer between the Antarctic Circumpolar Current and Timor Sea is relatively rapid, in the order of 300 yr (*Matsumoto and Key*, 2004).

However, a different transfer mechanism must be invoked to explain the occurrence of prolonged D-O events 8, 12, 14 and 16–17 in the Timor Sea planktonic $\delta^{18}\text{O}$ record, far away from the source of northern climate variability. D-O events are widely detected in Northern Hemisphere records, and model studies by *Knutti et al.* (2004) suggested that atmospheric processes largely transmit these climatic signals. Furthermore, oxygen isotope studies of stalagmites show evidence of atmospheric teleconnections between North Atlantic climate and the East Asian monsoonal convection (*Wang et al.*, 2001; *Burns et al.*, 2003; *Ruth et al.*, 2007). Modeling experiments also support that North Atlantic cooling can be transmitted through atmospheric teleconnections leading to cooling of the Asian continent and thereby weakening of the Asian summer monsoon (*Timmermann et al.*, 2005). Fluctuations in Asian monsoon intensity may have far reaching repercussions in the tropics through the coupling of Asian and Australian monsoon systems (*Hung et al.*, 2004). The migration of the Intertropical Convergence Zone (ITCZ) over the Indonesian archipelago represents a crucial link between the two monsoon systems. For instance, reconstructions of thermocline variability during Terminations I and II suggested that the displacement of the ITCZ largely controlled Australian monsoon intensity and ITF variability (*Xu et al.*, 2006, *Xu, pers. comm.*, 2007). A similar mechanism may have operated on shorter timescales during MIS 3 and played a crucial role in controlling climate and oceanography in the Timor Sea.

2.4.2 Paleoproductivity variations in the Timor Sea during MIS 3

Benthic foraminiferal abundance and distribution patterns are closely related to the availability of food at the sea floor, which is almost exclusively derived from the export flux of primary production in the photic zone (e.g. *Loubere*, 1991; *Altenbach*, 1992; *Loubere*, 1994, 1996). *Holbourn et al.* (2005) suggested that variations in the intensity of NW monsoonal winds over northern Australia were closely related to productivity fluctuations in the Timor Sea on a precessional scale. These authors interpreted increases in the numbers of buliminids and benthic foraminifera per gram as reflecting increased export flux due to more intense mixing within the upper water column, leading to nutrient enrichment and enhanced primary production. In our high-resolution record spanning MIS 3, buliminids exhibit maximum abundance during stadials whereas numbers decrease significantly during interstadials (Figure 2.6), suggesting that the intensity of the Australian monsoon may have also varied significantly on much shorter timescales. For instance, the intensity of monsoonal winds and frequency of related cyclones are related to the intensity of low-pressure systems over NW Australia (*Tapper*, 2002). The strength of these low-pressure systems is not only controlled by insolation but also by changes in albedo, related to vegetation

cover and cloudiness over the Pilbara region over relatively short timescales. Tropical cyclones, which form mostly between 10° and 20° S (*Suppiah, 1992*), can additionally contribute to strong vertical mixing of the upper water column (*Sriver and Huber, 2007*), leading to increasing primary production (*Lin et al., 2003*).

Buliminids show their highest abundance at 25–30 ka (Figure 2.6), close to the Last Glacial Maximum, when sea surface temperature (SST) was at a minimum (*Xu, pers. comm., 2007*) and productivity at a maximum (*Holbourn et al., 2005*). In contrast, the abundance of globocassidulinids increases markedly from 2 to 11 g⁻¹, during an interval (38–45 ka), which corresponds to the 25 °S February insolation maximum (Figure 2.6) and to more intense heating of the NW Australian landmass, triggering peak monsoon conditions and tropical cyclones. This is also the period, when the ITCZ reaches its most southerly position. The globocassidulinid maximum also coincides with somewhat higher $\Delta\delta^{13}\text{C}$ values during a sustained interval of low Mg/Ca (*G. ruber* white) and low planktonic $\delta^{18}\text{O}$, indicating lower SST and increased sea surface salinity. Core top data from the Timor Sea indicate that globocassidulinid maxima occur at intermediate carbon flux rates to the seafloor (4–10 g m⁻²yr⁻¹), whereas buliminids are associated with higher flux rates (*Holbourn, unpublished data*). It is also known that globocassidulinids increase in abundance following seasonal pulses of fresh phytodetritus (*Goody, 1988, 1993*) and appear to selectively favor diatoms as food (*Suhr et al., 2003*). Therefore, a change in regional oceanography must have been responsible for the increase in globocassidulinids: for instance a stronger influence of cool, silicate-rich surface-water providing a different food source.

The ITF transports low-salinity tropical waters from the western Pacific through the Indonesian Archipelago into the Eastern Indian Ocean, thereby feeding the SEC and LC. The low-salinity LC flows along the Western Australian coast into the Great Australian Bight (*Pearce and Cresswell, 1985*), whereas relatively cool, high-salinity water is transported northward by the undercurrent (*Cresswell, 1991*), which is linked to the eastern component of the Southern Hemisphere subtropical gyre forming the WAC. Isotopic data from the Exmouth Plateau (Core RS53-GC06, *McCorkle et al., 1998*) document that the distribution of water masses during the Last Glacial Maximum (LGM) was different from the present day. Large zones of cool surface-water occurred during glacial times, probably reflecting the increased influence of the WAC on surface-water circulation (*Wells and Wells, 1994*). These authors suggested that a large-scale reorganization of regional circulation patterns occurred with the development of a hydrological front between 15°–19° S, as the LC and WAC respectively decreased and increased in intensity. Thus during the LGM, the WAC acted as a dominant eastern-boundary current locally associated with upwelling of nutrient-rich water. A similar but less pronounced shift in water masses may have also taken place during cooler intervals of MIS 3 and explain the distribution of carbon-flux sensitive benthic foraminifera. Rapid and short-lived increases in globocassidulinids also occurred during Antarctic warm events A2–A4, which approximately corresponded to Heinrich events in the Northern Hemisphere. Shutdown of the thermohaline circulation during these events may have reduced the ITF, weakened the intensity of the LC and favored transient migrations of the hydrological front, thus altering the food export flux to the seafloor.

2.5 Conclusions

The benthic oxygen isotope record from Core MD01-2378 exhibits a Southern Hemisphere signal with Antarctic warm events A1–A4 distinctly expressed, whereas the planktonic oxygen isotope record reflects Northern Hemisphere climate with a strong imprint of longer-lasting D-O events 8, 12, 14 and 16–17. The Southern Hemisphere signal in the benthic $\delta^{18}\text{O}$ is probably transmitted through the transport of deep and intermediate water masses from the Southern Ocean into the eastern Indian Ocean and Timor Sea. In contrast, the Northern Hemisphere signal in the planktonic $\delta^{18}\text{O}$ may be transferred through atmospheric teleconnections due to the tight coupling between Asian and Australian monsoon systems.

High-resolution stable isotope data and benthic foraminiferal census counts from Core MD01-2378 provide new insights into centennial climate variability in the Timor Sea during MIS 3. Increasing abundance of high productivity indicators (buliminids) during stadials and decreasing abundance during interstadials point to significant changes in Australian monsoon intensity on these relatively short timescales. A sustained increase in globocassidulinids between Antarctic warm events A1 and A2 (38–45 ka), corresponding to the February insolation maximum at 25° S and an episode of intensified Australian monsoon, suggest northward migration of the hydrological front between the WAC and LC and resulting change in food export towards diatom dominated particulate organic carbon to the seafloor. This water mass shift is also supported by concurrent decreases in Mg/Ca and planktonic $\delta^{18}\text{O}$.

2.6 Acknowledgments

We thank Franck Bassinot, Yvon Balut and the crew of the RV "Marion Dufresne" of the Institut Français de Recherche et Technologie Polaires for their efforts during the WEPAMA Cruise as part of the IMAGES program. We are grateful to Michael Sarnthein and Juan Carlos Herguera for discussions, and to Brigitte Salomon for help with picking benthic foraminifera. Our paper benefited from careful reviews by F. Sierro and an anonymous reviewer. We gratefully acknowledge the Deutsche Forschungsgemeinschaft (DFG) for funding this research (Grant Ku 649/25–1).

Chapter 3

Evidence for Indonesian Throughflow slow-down during Heinrich Events 3-5

Rina Zuraida^{a,b}, Ann Holbourn^a, Dirk Nürnberg^b, Wolfgang Kuhnt^a, Anke Dürkop^a, Anna Erichsen^a

^aInstitute of Geosciences, Christian-Albrechts-University, Ludewig-Meyn-Str. 10-14, D-24118 Kiel, Germany

^bLeibniz-Institute of Marine Sciences, IFM-GEOMAR, Wischhofstr. 1-3, D-24148 Kiel, Germany

Published in *Paleoceanography*, 24(2009)

doi:10.1029/2008PA001653

Abstract. We present sea surface and upper thermocline temperature records (60–100 yr temporal resolution) spanning Marine Isotope Stage 3 (≈ 24 –62 kyr BP) from IMAGES Core MD01-2378 (121°47.27' E and 13°04.95' S; 1783 m water depth) located in the outflow area of the Indonesian Throughflow within the Timor Sea. Stable isotopes and Mg/Ca of the near surface dwelling planktonic foraminifer *Globigerinoides ruber* (white) and the upper thermocline dwelling *Pulleniatina obliquiloculata* reveal rapid changes in the thermal structure of the upper ocean during Heinrich Events. Thermocline warming and increased $\delta^{18}\text{O}_{\text{seawater}}$ (*P. obliquiloculata* record) during Heinrich Events 3, 4, and 5 reflect weakening of the relatively cool and fresh thermocline flow and reduced export of less saline water from the North Pacific and Indonesian Seas to the tropical Indian Ocean. Three main factors influenced Indonesian Throughflow variability during Marine Isotope Stage 3: (1) global slow-down in thermohaline circulation during Heinrich Events triggered by Northern Hemisphere cooling; (2) increased freshwater export from the Java Sea into the Indonesian Throughflow controlled by rising sea level from ≈ 60 to 47 ka and (3) insolation related changes in Australasian monsoon with associated migration of hydrological fronts between Indian Ocean and Indonesian Throughflow derived water masses at ≈ 46 –40 ka.

3.1 Introduction

Marine Isotope Stage 3 (MIS 3) is characterized by high-amplitude millennial scale climate variability, which has been generally associated with shifts in ice sheet mass balance and changing modes of Atlantic meridional overturning circulation (AMOC) (see *Clark et al., 2007*, for detailed review). Greenland ice core and North Atlantic records revealed that abrupt episodes of warming of 8–16 °C (*Huber et al., 2006*) were followed by more gradual returns to colder (stadial) conditions. These climatic oscillations with a typical duration of 1 to 3 kyrs have become known as Dansgaard-Oeschger (D-O) events. Northern Hemisphere climate records also unmasked the occurrence of unusual layers of ice rafted debris, subsequently named Heinrich layers, which have been linked to episodic, massive discharges of icebergs released from the Laurentide ice sheet into the North Atlantic during extreme stadials.

In contrast to Northern Hemisphere signals, climate variations appear to have been more subdued in the Southern Hemisphere with temperature changes of 1–3 °C recorded in Antarctica during MIS 3 (*EPICA Community Members, 2006*). Synchronization of Greenland and Antarctic ice cores using methane (*Blunier et al., 1998; Blunier and Brook, 2001; EPICA Community Members, 2006*) additionally revealed that Southern Hemisphere climate fluctuations were clearly out of phase with Northern Hemisphere variations during this interval. In particular, episodes of greatest warming in Antarctica during MIS 3 (the so called A 1–4 events) coincided with prolonged stadials or Heinrich Events (HEs). However, the repercussion of this bipolar seesaw on Southern Hemisphere climate evolution is still unclear, in particular in the low to mid latitudes, since high resolution climate proxy records are almost exclusively available from the Northern Hemisphere and southern high latitudes (*Lynch-Stieglitz, 2004*).

Proxy data and ocean modelling results both indicated that millennial scale climate variability was closely linked to changes in the rate of the AMOC. In particular, the AMOC is inferred to have considerably slowed down or even collapsed during HEs (*Sarnthein et al., 1994, 2001; Alley and Clark, 1999; Ganopolski and Rahmstorf, 2001; Broecker, 2003; Piotrowski et al., 2004*) resulting in major cooling at mid latitudes in the North Atlantic and southward displacement of the inter-tropical convergence zone (ITCZ). The widespread climatic impact of HEs was documented well beyond the North Atlantic in a variety of continental and marine settings including the Alboran Sea (*Cacho et al., 1999*), Santa Barbara Basin (*Hendy and Kennett, 2000*), China (*Wang et al., 2001*), Brazil (*Wang et al., 2004*), Australia (*Muller et al., 2008*), Borneo (*Partin et al., 2007*) and the Indo Pacific region (*Dannenmann et al., 2003; Levi et al., 2007*). The prevalence of a Northern Hemisphere climate signal at locations far away from the North Atlantic was previously attributed to a tight coupling between regional climate systems through vigorous atmospheric teleconnections. In particular, changes in surface salinity within the Indo-Pacific region were interpreted as fundamental alterations in monsoonal regime related to southward shifts of the ITCZ during HEs.

In contrast to the wealth of information concerning AMOC slow-down and related regional climatic impacts during HEs, relatively little is known about the effect of a reduction in North

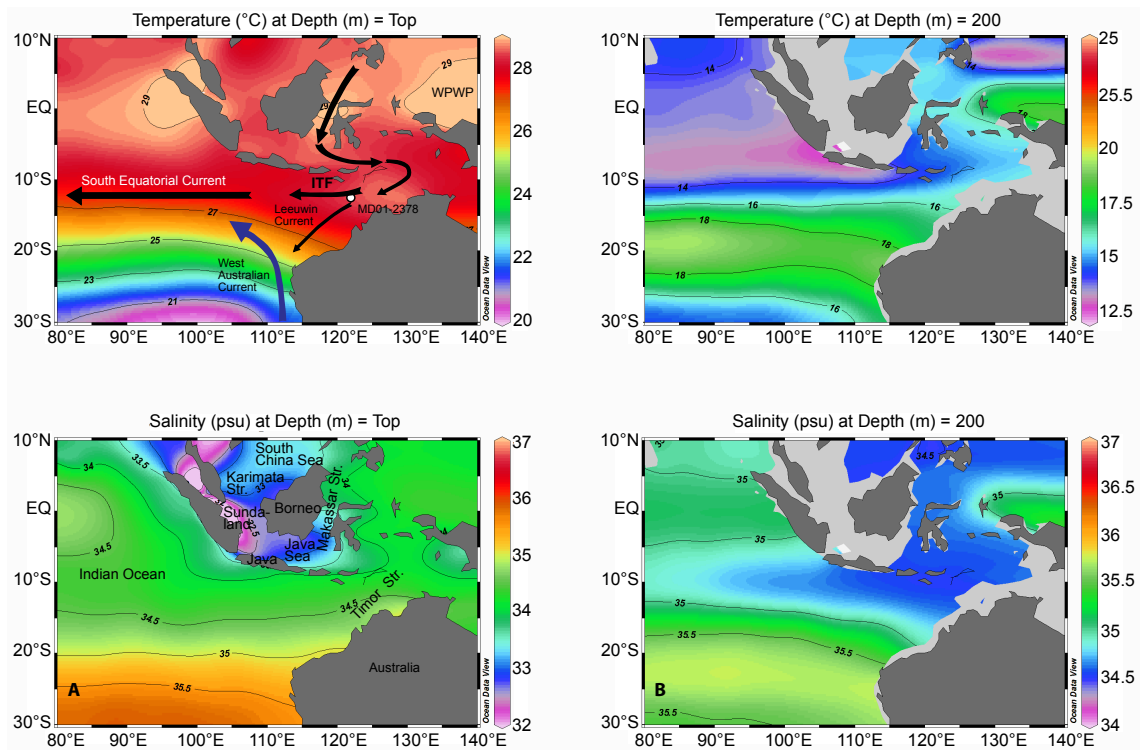


Figure 3.1 Annual temperature and salinity distribution in the Indo-Pacific region, based on World Ocean Atlas 2005 data (Locarnini *et al.*, 2006; Antonov *et al.*, 2006): (a) close to surface: habitat depth of *G. ruber* (white); (b) within upper thermocline: habitat depth of *P. obliquiloculata*. Arrows indicate modern current paths: ITF (black), South Equatorial Current (black), Leeuwin Current (black), and West Australian Current (dark blue). Core MD01-2378 is located within the main ITF outflow (white circle).

Atlantic deep water formation on the thermohaline circulation in the Pacific and Indian Oceans. The main return branch of the global thermohaline circulation consists of a westward flow from the Pacific Ocean through the Indonesian Archipelago where this flow is 'transformed' to produce the Indonesian Throughflow (ITF). Changes in ITF volume and/or hydrographic properties significantly influence the temperature, salinity and nutrient distribution in the upper water column of the Indian Ocean with major repercussions for Australasian and African climate. The conversion of inflowing relatively cool and fresh North Pacific water through mixing and addition of freshwater within the archipelago into the ITF is modulated by seasonality and regional climate patterns (Ilahude and Gordon, 1996; Sprintall *et al.*, 2003). The resulting ITF flows out of the Indonesian archipelago into the Indian Ocean through three eastern passages (Lombok, Ombai and Timor Straits). Among the three outflow passages, the Timor Strait plays the most significant role, in particular during times of lowered sea level, as it is substantially deeper and wider than the other two passages.

We generated centennial resolution records of surface and upper thermocline $\delta^{18}\text{O}$ and Mg/Ca temperatures spanning MIS 3 (24–62 ka) in Core MD01-2378 (13°4.95' S and 121°47.27' E; 1783

m water depth), situated within the main ITF outflow from the Timor Strait into the eastern Indian Ocean (Figure 3.1). Thus, this core is ideally located to monitor changes in ITF intensity and vertical structure and to resolve the impact of millennial scale climate events on the ITF outflow and related effects on the tropical Indian Ocean. This work extends previous investigations of glacial-interglacial ITF variability in the same core (Holbourn *et al.*, 2005; Xu *et al.*, 2006, 2008) and in other cores located within the ITF outflow path (Spooner *et al.*, 2005; Murgese and De Deckker, 2007). Our main objectives are:

1. To detect the amplitude and frequency of changes in surface and thermocline temperature and $\delta^{18}\text{O}$ within the main ITF outflow during MIS 3.
2. To test the hypothesis that a slow-down in thermohaline circulation during HEs reduces the cool and fresh ITF thermocline flow.
3. To test modeling predictions that a reduction in ITF thermocline flow during HEs alters hydrographic profiles in the eastern Indian Ocean and leads to a warmer and saltier tropical Indian Ocean.

3.2 Material and method

This study is based on sediment samples ($30\text{--}40\text{ cm}^{-3}$ from 1 cm thick slices) taken at 1 cm interval (approximating 60–100 yr) between 448 and 895 cm in IMAGES Core MD01-2378. Samples were initially dried and weighed, then washed over a $63\text{ }\mu\text{m}$ sieve. Residues were dried on a sheet of filter paper and weighed, then sieved into $63\text{--}150\text{ }\mu\text{m}$, $150\text{--}250\text{ }\mu\text{m}$, $250\text{--}315\text{ }\mu\text{m}$, and $>315\text{ }\mu\text{m}$ fractions. Coupled Mg/Ca and $\delta^{18}\text{O}$ analyses were performed on two species of planktonic foraminifer *Globigerinoides ruber* (white sensu stricto) and *Pulleniatina obliquiloculata* from the $250\text{--}315\text{ }\mu\text{m}$ size fraction to reconstruct surface and subsurface water masses conditions during MIS 3.

3.2.1 Mg/Ca analysis

Thirty well-preserved tests of the near surface dweller *G. ruber* (white) and 20 tests of the thermocline dweller *P. obliquiloculata* were selected under a binocular microscope, then gently crushed between two glass plates and cleaned following the protocol outlined in Barker *et al.* (2003). The choice of cleaning protocol was based on the relatively low terrigenous clay content in Core MD01-2378 (carbonate content $>70\%$, Holbourn *et al.*, 2005). The first step (clay removal) involves rinsing foraminiferal fragments five times with ultra-pure water, then twice with Aristar methanol, with ultrasonic treatment after each rinse. The next step is the removal of organic material using $250\text{ }\mu\text{L}$ of hot ($97\text{ }^\circ\text{C}$) oxidizing 1% NaOH/ H_2O_2 reagent (10 mL 0.1 N analytical grade NaOH and $100\text{ }\mu\text{L}$ 30% supra-pure H_2O_2) for 10 minutes. This process would produce gaseous build-up within sample tubes, therefore samples have to be agitated every 2.5 minutes to release bubbles. To maintain the chemical reaction, the samples were placed in an ultrasonic bath

for a few seconds. The oxidizing solution was then removed by rinsing the samples three times with ultra-pure water. The samples were then transferred into clean tubes and leached with 250 μL 0.001M HNO_3 (sub-boiled distilled) during a 30 seconds ultrasonic treatment, followed by two rinses with ultra-pure water, in order to remove any adsorbed contaminant. The final step involves the dissolution of samples in 500 μL 0.075 M HNO_3 (sub-boiled distilled). The solution has to be diluted with ultra-pure water to achieve Ca concentrations of 30–70 ppm.

A total of 543 samples of *G. ruber* (white) and 596 of *P. obliquiloculata* were analyzed with the ICP-OES Spectro Ciros CCD SOP at the Institute of Geosciences, Christian-Albrechts-University, Kiel. The analytical error of the instrument is $\approx 0.1\%$. The replicability of our measurements, based on 72 *G. ruber* (white) and 77 *P. obliquiloculata* replicate samples, is 0.2 mmol/mol (corresponding to 0.6 °C) for *G. ruber* (white) and 0.2 mmol/mol (corresponding to 1 °C) for *P. obliquiloculata*. We checked the validity of Mg/Ca values by evaluating the Fe/Mg contents of the samples using the limit of 0.1 mol/mol suggested by [Barker et al. \(2003\)](#). As a result, one sample of *G. ruber* and one sample of *P. obliquiloculata* were rejected. The effect of dissolution on Mg/Ca in the interval 1–460 ka in Core MD01-2378 was evaluated by [Xu et al. \(2006\)](#) using shell weights and a foraminiferal test fragmentation index. No significant effect of dissolution was detected even during the LGM and MIS 6, when dissolution would be most likely in the Timor Sea due to higher organic export flux ([Holbourn et al., 2005](#)).

Sea surface temperature (SST) and upper thermocline temperature were reconstructed from *G. ruber* (white) and *P. obliquiloculata* Mg/Ca values, respectively. Conversion of Mg/Ca values into temperature was performed using the general equation $\text{Mg/Ca} = (0.38 \pm 0.02) \cdot \exp[(0.090 \pm 0.003) \cdot T]$ for *G. ruber* (white) and the species specific $\text{Mg/Ca} = (0.328 \pm 0.007) \cdot \exp[(0.090 \pm 0.003) \cdot T]$ for *P. obliquiloculata* ([Anand et al., 2003](#)). The choice of equations was based on a study of 33 core tops ([Erichsen, 2008](#), unpublished Diploma-Thesis) and 19 Conductivity-Temperature-Depth (CTD) profiles taken during the Sonne-185 cruise in October 2005 ([Kuhnt, 2005](#)) and comparison to

Table 3.1 Comparison of average water temperatures at sea surface and 100 m water depth at 33 stations in the Timor Sea (CTD data from Sonne-185 cruise) with Mg/Ca derived temperature estimates from equations of [Anand et al. \(2003\)](#) and with $\delta^{18}\text{O}$ derived temperature estimates.

| | Minimum | Maximum | Stations | Mean | Median | Std Deviation | Variance | Std Error |
|--|---------|---------|----------|-------|--------|---------------|----------|-----------|
| WOA05 annual mean SST | 27.90 | 28.50 | 33 | 28.31 | 28.30 | 0.13 | 0.02 | 0.02 |
| WOA05 Austral Summer (Jan-Mar) SST | 28.80 | 29.50 | 33 | 29.16 | 29.20 | 0.25 | 0.06 | 0.04 |
| WOA05 Austral Winter (Jul-Sep) SST | 26.00 | 26.80 | 33 | 26.63 | 26.70 | 0.18 | 0.03 | 0.03 |
| October 2005 SST from SO-185 CTD (at 10 m water depth) | 26.80 | 28.40 | 19 | 27.65 | 27.60 | 0.42 | 0.18 | 0.10 |
| Mg/Ca <i>G. ruber</i> (white sensu stricto) | 4.25 | 6.62 | 33 | 5.27 | 5.20 | 0.45 | 0.20 | 0.08 |
| Mg/Ca-SST from general equation of Anand et al. (2003) | 26.80 | 31.80 | 33 | 29.19 | 29.10 | 0.93 | 0.87 | 0.16 |
| Mg/Ca-SST from <i>G. ruber</i> (white) equation of Anand et al. (2003) | 24.80 | 29.10 | 33 | 26.83 | 26.70 | 0.82 | 0.67 | 0.14 |
| $\delta^{18}\text{O}$ <i>G. ruber</i> | -3.20 | -2.30 | 32 | -2.95 | -3.00 | 0.19 | 0.04 | 0.03 |
| <i>G. ruber</i> calcification temperature from $\delta^{18}\text{O}$ | 25.90 | 29.70 | 32 | 28.60 | 28.80 | 0.79 | 0.62 | 0.14 |
| WOA05 annual mean temperature at 100 m water depth | 22.60 | 24.50 | 32 | 23.80 | 23.85 | 0.49 | 0.24 | 0.09 |
| WOA05 Austral Summer (Jan-Mar) temperature at 100 m water depth | 22.60 | 24.20 | 32 | 23.41 | 23.30 | 0.36 | 0.13 | 0.06 |
| WOA05 Austral Winter (Jul-Sep) temperature at 100 m water depth | 22.40 | 25.10 | 32 | 23.94 | 23.70 | 0.80 | 0.64 | 0.14 |
| October 2005 temperature from SO-185 CTD (at 100 m water depth) | 18.40 | 24.60 | 18 | 22.94 | 23.35 | 1.44 | 2.07 | 0.34 |
| Mg/Ca <i>P. obliquiloculata</i> | 2.28 | 3.61 | 32 | 2.78 | 2.72 | 0.31 | 0.10 | 0.05 |
| Mg/Ca <i>P. obliquiloculata</i> temperature from species specific equation of Anand et al. (2003) | 21.50 | 26.70 | 32 | 23.69 | 23.50 | 1.21 | 1.46 | 0.21 |
| Mg/Ca <i>P. obliquiloculata</i> temperature from <i>G. ruber</i> (white) equation of Anand et al. (2003) | 18.60 | 23.20 | 32 | 20.55 | 20.40 | 1.07 | 1.15 | 0.19 |
| $\delta^{18}\text{O}$ <i>P. obliquiloculata</i> | -2.10 | -1.40 | 32 | -1.83 | -1.90 | 0.15 | 0.02 | 0.03 |
| Mg/Ca <i>P. obliquiloculata</i> calcification temperature from $\delta^{18}\text{O}$ | 21.90 | 24.90 | 32 | 23.90 | 24.00 | 0.64 | 0.41 | 0.11 |

World Ocean Atlas (WOA) data (*Locarnini et al., 2006*). Mean *G. ruber* temperature (26.8 °C with 0.82 standard deviation), estimated from the species specific equation of *Anand et al. (2003)*, is significantly cooler than WOA annual average (28.3 °C with 0.13 standard deviation) and CTD measurements at 10 m (27.6 °C, with 0.42 standard deviation) from the Sonne-185 cruise. Mean SST (29.2 °C with 0.93 standard deviation), based on the general equation of *Anand et al. (2003)*, slightly overestimates WOA annual average by ≈ 0.9 °C, and agrees with mean WOA summer (January-March) SST (29.2 °C with 0.25 standard deviation). Mean *P. obliquiloculata* temperature (23.7 °C with 1.21 standard deviation), estimated from the species-specific equation, closely matches WOA annual average temperature at 100 m water depth (23.8 °C with 0.49 standard deviation), and is only slightly warmer than CTD measurements at 100 m water depth (22.9 °C with 1.44 standard deviation) from the Sonne-185 cruise. The choice of equations is additionally supported by calculation of calcification temperatures, based on $\delta^{18}\text{O}_{\text{carbonate}}$ and $\delta^{18}\text{O}_{\text{seawater}}$ measurements at five CTD stations. Mean calcification temperatures (28.6 °C for *G. ruber* and 23.9 °C for *P. obliquiloculata*) are close to WOA annual average values for sea surface (28.3 °C) and 100 m water depth (23.8 °C) and to our Mg/Ca based estimates (29.2 °C for *G. ruber* and 23.7 °C for *P. obliquiloculata*). Core top Mg/Ca data and temperatures are provided in Table 3.1. Marine Isotope Stage 3 stable isotope, Mg/Ca and estimated temperature at MD01-2378 are archived at <http://www.pangaea.de>.

3.2.2 Stable isotope analysis

For stable isotope analysis, we selected 20 tests of *P. obliquiloculata* from the 250–315 μm size fractions. All tests were checked for cement encrustations and infillings before being gently crushed between two glass plates and cleaned with methanol in an ultrasonic bath, then dried at 40 °C. Measurements of 45 replicate samples indicate that the mean reproducibility is $\pm 0.20\%$ for $\delta^{18}\text{O}$ and $\pm 0.12\%$ for $\delta^{13}\text{C}$. Stable isotope analysis was performed at IfM-Geomar on a Finnigan MAT 252 Mass Spectrometer with an automated Kiel carbonate preparation device. Samples were reacted by individual acid addition. The mean external error and reproducibility of carbonate standards is $< 0.07\%$ for $\delta^{18}\text{O}$ and 0.07% for $\delta^{13}\text{C}$. The values are reported relative to the Peedee Belemnite (PDB) scale, based on calibration to the National Bureau of Standards (NBS) 19. Stable isotope data for *G. ruber* (white) are from *Dürkop et al. (2008)*, see Chapter 2).

3.2.3 Paleo-salinity reconstruction from $\delta^{18}\text{O}$ seawater

Although reconstruction of paleo-salinity from $\delta^{18}\text{O}_{\text{seawater}}$ ($\delta^{18}\text{O}_{\text{sw}}$) may have large error propagation, estimation from paired $\delta^{18}\text{O}$ and Mg/Ca analyses allows to narrow down the uncertainty limit (*Rohling, 2004*). We calculated $\delta^{18}\text{O}_{\text{sw}}$ using the following equation $\delta^{18}\text{O}_{\text{sw}} = 0.27 + (T - 16.5 + 4.8 * \delta^{18}\text{O}) / 4.8$ (*Bemis et al., 1998*) for both *G. ruber* (white) and *P. obliquiloculata*. We used the *Orbulina universa* LL equation for both *G. ruber* and *P. obliquiloculata*, as the equation for the non-spinose *Globigerina bulloides* is only applicable for that species (*Bemis et al., 1998*). We additionally experimented with other equations (*O. universa* HL and *G. bulloides*), but found

no significant differences in our results. Since the equation extracts the effect of temperature on oxygen isotope fractionation, the calculated $\delta^{18}\text{O}_{sw}$ is mainly influenced by $\delta^{18}\text{O}_{sw}$ variability related to continental ice volume and local $\delta^{18}\text{O}_{sw}$ fluctuations related to surface and upper thermocline salinities. In order to remove the ice volume effect and to test the robustness of our $\delta^{18}\text{O}_{sw}$ reconstructions, we used two different methods:

1. We applied one ice volume correction by subtracting benthic $\delta^{18}\text{O}_{sw}$ (fivepoint smoothed) from planktonic $\delta^{18}\text{O}_{sw}$ within the same samples. To calculate benthic $\delta^{18}\text{O}_{sw}$, we used the [Bemis et al. \(1998\)](#) equation, assuming bottom water temperature of 2 °C and minimal fluctuations during MIS 3 ([Labeyrie et al., 1987](#)). The 2 °C bottom water temperature assumption for MIS 3 is inferred from recent measurements of bottom temperature (2.8 °C) at the location of Core MD01-2378 during the Sonne-185 cruise ([Kuhnt, 2005](#)). This temperature difference is approximately half of that estimated between the Holocene and LGM ([Shackleton, 1987](#)).
2. We also applied an alternative ice volume correction based on the reconstructed MIS 3 sea level curve for the central Red Sea ([Siddall et al., 2003](#)). In order to ensure chronological compatibility, we tuned the Red Sea record to the MD01-2378 record. Then, we converted the sea level record into $\delta^{18}\text{O}$ units by assuming that a 1.1‰ change in $\delta^{18}\text{O}$ is equivalent to 130 m sea level change. Because of resolution difference (200 yrs in Core KL11 and 60–100 yrs in Core MD01-2378), we interpolated the rest of Red Sea $\delta^{18}\text{O}$ sea level values to fit the MD01-2378 age scale.

Comparison between the two curves shows no significant differences in shape and absolute values, and supports that thermocline anomalies during MIS 3 are independent of the choice of ice volume correction.

3.2.4 Age model

The original age model for the MIS 3 interval in Core MD01-2378 was derived from correlation of high-resolution benthic oxygen-isotope data to the isotope record of the EPICA Dronning Maud Land (EDML) ice core ([EPICA Community Members, 2004](#)), which was synchronized to the NGRIP ice core following the new Greenland Ice Core Chronology (GICC05) timescale ([EPICA Community Members, 2006](#); [Andersen et al., 2006](#); [Svensson et al., 2006](#)). The MD01-2378 age model for this time interval is additionally constrained by 11 AMS ^{14}C dates, measured on *G. ruber* (white). Details of the original age model over the MIS 3 interval are provided in [Dürkop et al. \(2008\)](#), see Chapter 2, Section 2.3.1 and Figure 2.4). In this study, we further constrained the MIS 3 interval between 742 and 895 cm with an additional tie point between the NGRIP oxygen-isotope data on the GICC05 timescale ([Svensson et al., 2008](#)) and our high-resolution planktonic $\delta^{18}\text{O}$ record. An interpolated curve was fitted through the tie points using a Stineman function, and it was used to determine the age of each sample. The lower part of our age

model from 817 to 895 cm (corresponding to 54.5–62.5 ka) is based on linear extrapolation. Table 3.2 provides all tie points used in the revised age model for the MIS 3 interval in Core MD01-2378.

3.3 Results

3.3.1 Oxygen isotopes

Planktonic foraminiferal $\delta^{18}\text{O}$ *G. ruber* (white) values vary between $\approx -1.1\text{‰}$ and -1.9‰ over the entire MIS 3 record (Figure 3.2). Three long-term trends are observed: (1) in the older part of the record before 55 ka, $\delta^{18}\text{O}$ values decrease from -1.5‰ to -1.9‰ ; (2) between 55 and 39 ka, planktonic $\delta^{18}\text{O}$ increases to -1.3‰ ; (3) after a rapid decrease in planktonic $\delta^{18}\text{O}$ to -1.7‰ at 37.5 ka, a continuous increase of -0.6‰ occurs until 26 ka, followed by a slight decrease in values. Superimposed on this long-term variability are high frequency variations, which show close affinity to fluctuations characteristic of northern high latitudes planktonic and ice core records. However, only the longer lasting D-O warm events 8, 12, 14 and 16–17 are clearly expressed by decreases of $\approx 0.2\text{‰}$ in the MD01-2378 record, whereas HEs 3–6 are marked by increases of $\approx 0.1\text{--}0.2\text{‰}$ (Figure 3.2).

The $\delta^{18}\text{O}$ *P. obliquiloculata* varies between 0.1 and -0.8‰ , showing somewhat higher amplitude variations than $\delta^{18}\text{O}$ *G. ruber* (white) (Figure 3.3). Three long-term trends are evident over the MIS 3 interval: (1) prior to 53.5 ka, $\delta^{18}\text{O}$ *P. obliquiloculata* values decrease from -0.2‰ to -0.7‰ ; (2) between 53 and 39 ka there is an overall increase from -0.7 to 0.0‰ ; (3) following an initial decline to -0.3‰ at 39–38 ka, a long-term increase from -0.3 to 0.1‰ occurs between 38 and 24 ka. The $\delta^{18}\text{O}$ *P. obliquiloculata* curve is also characterized by high frequency variations and the most pronounced D-O warm events 8, 12, 14 and 16–17 and the HEs 3–6 are detected by respective distinct increases and decreases of $\approx 0.1\text{--}0.2\text{‰}$ (Figure 3.3).

Table 3.2 Tie points between MD01-2378 benthic foraminiferal $\delta^{18}\text{O}$ and EDML ice core $\delta^{18}\text{O}$ *Dürkop et al.* (2008, see Chapter 2) and between planktonic foraminifera $\delta^{18}\text{O}$ and NGRIP ice core $\delta^{18}\text{O}$.

| a) Tie points from <i>Dürkop et al.</i> (2008) | | | | |
|--|-----------------------------------|--------------------|------------------------------------|---|
| Core MD01-2378 | | EDML ice core | | Event |
| Depth [cm] | $\delta^{18}\text{O}$ [‰ vs. PDB] | GICC05 age [ka BP] | $\delta^{18}\text{O}$ [‰ vs. SMOW] | |
| 342 | 3.92 | 18.15 | -51.89 | $\delta^{18}\text{O}$ maximum prior to deglaciation |
| 506 | 3.92 | 27.45 | -52.53 | $\delta^{18}\text{O}$ maximum after AIM 4 event |
| 554 | 3.72 | 30.65 | -51.04 | $\delta^{18}\text{O}$ maximum before AIM 4 event |
| 642 | 3.31 | 38.15 | -48.68 | Last $\delta^{18}\text{O}$ minimum of A1 event |
| 664 | 3.65 | 39.85 | -50.91 | $\delta^{18}\text{O}$ maximum before A1 event |
| 742 | 3.28 | 47.25 | -47.44 | $\delta^{18}\text{O}$ minimum in center of A2 event |

| b) Additional planktonic foraminiferal tie point | | | | |
|--|-----------------------------------|--------------------|------------------------------------|--|
| Core MD01-2378 | | NGRIP ice core | | Event |
| Depth [cm] | $\delta^{18}\text{O}$ [‰ vs. PDB] | GICC05 age [ka BP] | $\delta^{18}\text{O}$ [‰ vs. SMOW] | |
| 817 | -1.58 | 54.49 | -42.90 | $\delta^{18}\text{O}$ maximum preceding D-O 14 |

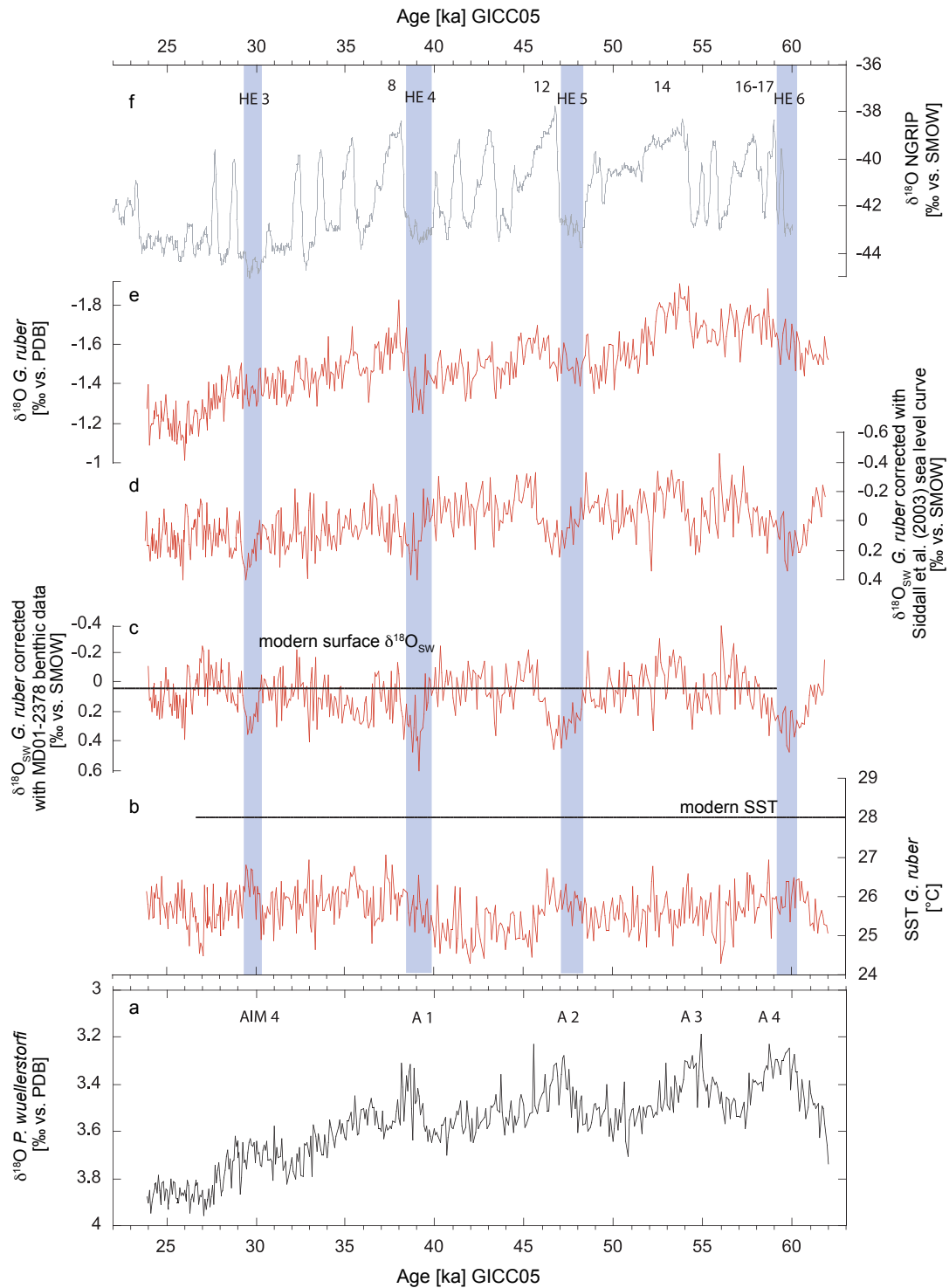


Figure 3.2 (a) Benthic $\delta^{18}\text{O}$ (*P. wuellerstorfi*) spanning MIS 3 in Core MD01-2378 from [Dürkop et al. \(2008, see Chapter 2\)](#). AIM 4 and A 1–4 refer to Antarctic warm events; (b) *G. ruber* (white) Mg/Ca derived SST, average SST over MIS 3 is 25.6 °C in contrast to present day annual SST of 28.3 °C ([Locarnini et al., 2006](#)); (c) Surface $\delta^{18}\text{O}_{sw}$; note: dashed line indicates modern surface $\delta^{18}\text{O}_{sw}$ measured in water samples from SO-185 cruise (0.05‰); (d) Surface $\delta^{18}\text{O}_{sw}$ corrected with Red Sea ice volume curve of [Siddall et al. \(2003\)](#); (e) planktonic $\delta^{18}\text{O}$ of *G. ruber* (white) from [Dürkop et al. \(2008, see Chapter 2\)](#); (f) NGRIP ice core $\delta^{18}\text{O}$ plotted on common GICC05 time scale ([Svensson et al., 2006, 2008](#)). Numbers refer to longer-lasting D-O events. Shaded bars indicate Heinrich events (HEs 3–6).

3.3.2 Mg/Ca temperature reconstructions

Average surface (25.6 °C) and upper thermocline (21.0 °C) Mg/Ca-temperature estimates over MIS 3 in Core MD01-2378 are cooler by nearly 3 °C, compared to present day mean annual SST of 28.3 °C and upper thermocline temperature of 23.8 °C (World Ocean Atlas 2005 data, [Locarnini et al., 2006](#)). Figures 3.2 and 3.3 show that temperature oscillations are more pronounced within the thermocline water mass than at the surface: SST varies between 24.3 °C and 27.0 °C, whereas upper thermocline temperature varies between 18.8 °C and 23.8 °C.

From 63 to 45 ka, SST values oscillate between 25 and 26 °C. At 45–40 ka, the SST record is marked by a prominent cooling event, which corresponds to the interval between HE 4 and HE 5 and Antarctic warm events A 1 and A 2 (Figure 3.2). This major cooling event starts with a rather abrupt decrease of 1.5 °C at the end of A 2 (46–45 ka), after which values oscillate around 25 °C for a further ≈ 5 kyr. The end of the cooling event is marked by a gradual warming of 1.5 °C from ≈ 40 to 37 ka, after which SST are maintained around 25–26 °C. In contrast to the thermocline temperature estimates, SST shows no clear imprint of HEs.

Relatively high temperature values (centering around 22 °C) are registered in the upper thermocline during HE 6 (Figure 3.3). From the end of HE 6, the upper thermocline record shows an overall cooling trend: from 22 °C at 60 ka to 19.5 °C at 48 ka, in contrast to the more consistent SST values. From 48 to 24 ka, temperatures fluctuate between 22 °C and 20 °C. However, a salient feature of the upper thermocline record within this interval is the occurrence of prominent increases in temperature during HEs 3–5, with lowest temperatures of ≈ 19.5 °C at the beginning of each HE and peak temperatures in excess of 22–24 °C at the end of each HE.

3.3.3 Sea surface and upper thermocline salinity estimates ($\delta^{18}\text{O}_{sw}$)

The MD01-2378 surface $\delta^{18}\text{O}_{sw}$ record (corrected for ice volume, see Methods) fluctuates between -0.3‰ and 0.4‰ SMOW with an average of 0.1‰ over MIS 3. Northern Hemisphere stadial events HEs 3–6 are marked by prominent increases of ≈ 0.2 –0.3‰ in surface $\delta^{18}\text{O}_{sw}$ (Figure 3.2). HE 5 differs somewhat from other HEs, because high values (≈ 0.6 –0.4‰) are maintained for ≈ 1 kyr during the early part of this interstadial.

Thermocline $\delta^{18}\text{O}_{sw}$ oscillates between -0.2‰ and 1.2‰ with an average of 0.4‰ over MIS 3. Values increase markedly by ≈ 0.2 –0.4‰ (Figure 3.3) during HEs 3–6. The increase in thermocline $\delta^{18}\text{O}_{sw}$ during HE 5 is more gradual and less pronounced than during HEs 3–4. As for surface $\delta^{18}\text{O}_{sw}$, interstadials are generally characterized by values close to modern $\delta^{18}\text{O}_{sw}$.

Based on measurements of water samples obtained during Sonne-185 cruise, the modern values of surface $\delta^{18}\text{O}_{sw}$ and thermocline $\delta^{18}\text{O}_{sw}$ close to the position of our core are 0.05‰ and 0.20‰, respectively, which gives a difference of -0.15‰ between surface and thermocline. During MIS 3, the average difference between $\delta^{18}\text{O}_{sw}$ surface and thermocline water masses was -0.3‰, indicating a somewhat more stratified upper water column during MIS 3.

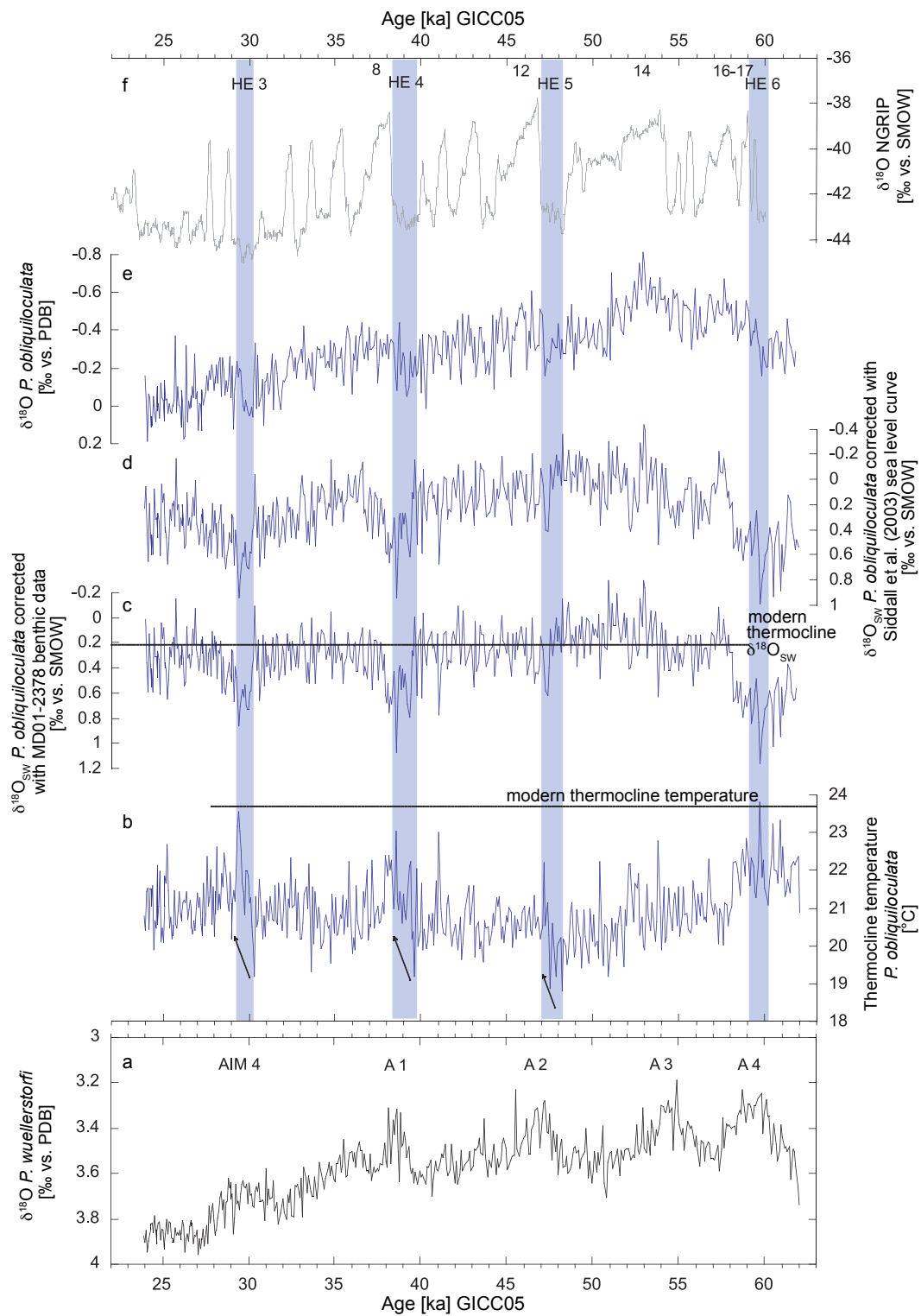


Figure 3.3 (a) Benthic $\delta^{18}\text{O}$ (*P. wuellerstorfi*) spanning MIS 3 in Core MD01-2378 from [Dürkop et al. \(2008, see Chapter 2\)](#). AIM 4 and A 1–4 refer to Antarctic warm events; (b) *P. obliquiloculata* Mg/Ca derived upper thermocline temperature (100 m water depth), average value over MIS 3 is 21 °C in contrast to present day annual value of 23.8 °C ([Locarnini et al., 2006](#)); (c) upper thermocline $\delta^{18}\text{O}_{\text{sw}}$; note: dashed line indicates modern upper thermocline $\delta^{18}\text{O}_{\text{sw}}$ measured in water samples from SO-185 cruise (0.20‰); (d) Thermocline $\delta^{18}\text{O}_{\text{sw}}$ corrected with Red Sea ice volume curve of [Siddall et al. \(2003\)](#); (e) planktonic $\delta^{18}\text{O}$ of *P. obliquiloculata*; (f) NGRIP ice core $\delta^{18}\text{O}$ plotted on common GICC05 time scale ([Svensson et al., 2006, 2008](#)). Numbers refer to longer lasting D-O events. Shaded bars indicate Heinrich events (HEs 3–6). Arrows highlight temperature changes during HEs.

3.3.4 Carbon isotopes

Planktonic $\delta^{13}\text{C}$ of *G. ruber* (white) decreases between 64 and 60 ka during HE 6, reaching minimum value of $\approx 0.95\text{‰}$ at 61 ka (Figure 3.4). From the end of HE 6, values show a two stepped, long-term increase: (1) from ≈ 1.2 to 1.5‰ between 60 and 52 ka and (2) from ≈ 1.4 to 1.6‰ between 52 and 31 ka. After 31 ka, values exhibit an overall decrease, reaching $\approx 1.3\text{‰}$ at 23 ka. The $\delta^{13}\text{C}$ record of *P. obliquiloculata* also shows a decrease during HE 6: from ≈ 0.9 at 64 ka to $\approx 0.6\text{‰}$ at 61 ka, after which values increase until ≈ 50 ka, when a maximum of $\approx 1.1\text{‰}$ is attained. From 50 to 31 ka, values generally oscillate between ≈ 1.1 and 0.9‰ . Between 31 and 23 ka, values show an overall decreasing trend from ≈ 1.1 to 0.9‰ . As for the present day, the gradient between the *G. ruber* (white) and *P. obliquiloculata* $\delta^{13}\text{C}$ does not deviate markedly from 0.5‰ over the whole interval studied (Figure 3.4).

Figure 3.4 shows that the *G. ruber* (white) and *P. obliquiloculata* $\delta^{13}\text{C}$ records exhibit overall similar trends as the epibenthic $\delta^{13}\text{C}$ in Core MD01-2378. Comparison of surface, thermocline and bottom water $\delta^{13}\text{C}$ profiles in Core MD01-2378 reveals an increasing trend from ≈ 60 to 50 ka, followed by a plateau until ≈ 30 ka and a final decrease until ≈ 23 ka. Comparison with Atlantic and Pacific records (Pahnke and Zahn, 2005; Piotrowski et al., 2005) suggests that the increase at ≈ 60 to 50 ka is a global feature. Values ranging between ≈ 0.0 and 0.3‰ for benthic $\delta^{13}\text{C}$ are significantly lower than for planktonic $\delta^{13}\text{C}$, and are in agreement with present day values at this location in the Timor Sea (Figure 3.5).

3.4 Discussion

3.4.1 Timor Sea hydrography and planktonic foraminiferal habitats

The present day upper thermal structure in the Timor Sea, close to the location of Core MD01-2378, is characterized by a near surface water mass (0–50 m water depth) with a relatively stable temperature averaging ≈ 28 °C and a thermocline water mass (50–250 m water depth) exhibiting a steep temperature gradient from ≈ 28 to 12 °C (Figure 3.5). Along with this marked temperature change, a sharp contrast in $\delta^{13}\text{C}$ also occurs within the upper water column (Figure 3.5) with values $> 1.2\text{‰}$ in the upper 50 m declining to $< 1\text{‰}$ at ≈ 100 m and reaching ≈ 0.4 – 0.1‰ below 250 m. The temperature difference between surface and upper thermocline (≈ 100 m water depth) water masses is ≈ 5 °C today, which compares well with the range of values registered during MIS 3 (Figures 3.2–3.3), suggesting that our temperature reconstructions provide realistic estimates, although thermocline temperature appears to have fluctuated more than SST during MIS 3. The planktonic and benthic $\delta^{13}\text{C}$ profiles over MIS 3 also show broad agreement with modern $\delta^{13}\text{C}$ values for surface, thermocline and bottom water masses, even though long- and short-term temporal variations are detected within the three records (Figure 3.4).

One of the limitations in the application of multi-species Mg/Ca thermometry is that inter-species differences may reflect the migration of some species within the water column during their life cycle and/or changes in habitat depth rather than real temperature changes at a constant depth.

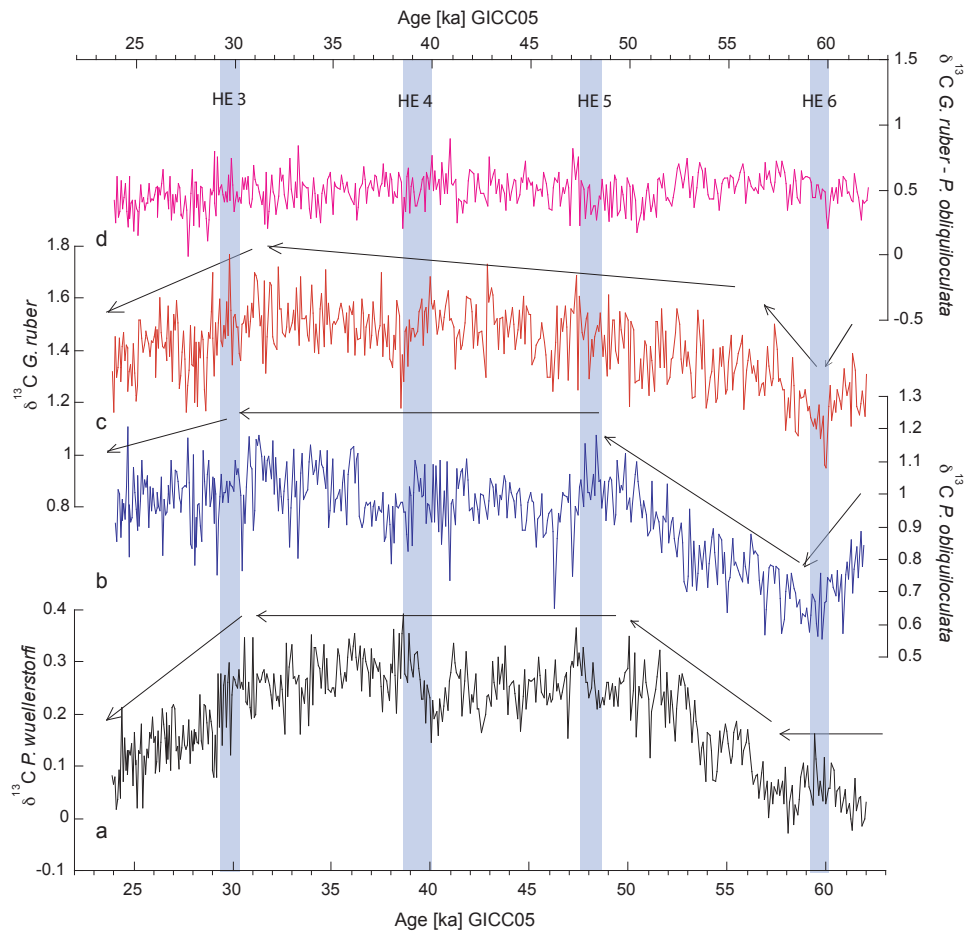


Figure 3.4 (a) Benthic $\delta^{13}\text{C}$ (*P. wuellerstorfi*) spanning MIS 3 in Core MD01-2378 from [Dürkop et al. \(2008, see Chapter 2\)](#); (b) planktonic $\delta^{13}\text{C}$ of upper thermocline dweller *P. obliquiloculata*; (c) planktonic $\delta^{13}\text{C}$ of near surface dweller *G. ruber* from [Dürkop et al. \(2008, see Chapter 2\)](#); (d) Consistent $\delta^{13}\text{C}$ gradient between *G. ruber* and *P. obliquiloculata* supports that respective depth habitats of these two species did not change significantly during MIS 3. Arrows highlight main trends during MIS 3.

The near surface dweller *G. ruber* (white) exhibits relatively consistent Mg/Ca values ([Eggins et al., 2003](#)) indicating that the effect due to vertical migration is negligible and calculated SST accurately reflect the assigned habitat depth of upper 50 m for this species ([Anand et al., 2003](#)). In terms of seasonality, *G. ruber* (white) Mg/Ca commonly reflects average annual hydrographic conditions due to the almost uniform occurrence of this species throughout the year ([Hemleben et al., 1989](#); [Lin et al., 1997](#); [Tedesco and Thunell, 2003](#)). However, in the Timor Sea, core top values of *G. ruber* fall into the range of average summer SST (29 °C) ([Xu et al., 2006](#)) (Table 3.1). Although the deeper dweller *P. obliquiloculata* exhibits high mobility in the water column and seasonality ([Prell and Damuth, 1978](#)), sediment trap studies indicate that this species mainly calcifies below the mixed layer ([Bé, 1977](#); [Ravelo et al., 1990](#); [Pflaumann and Jian, 1999](#)) or between 50 and 100 m ([Anand et al., 2003](#)). [Ravelo and Fairbanks \(1992\)](#) and [Cléroux et al.](#)

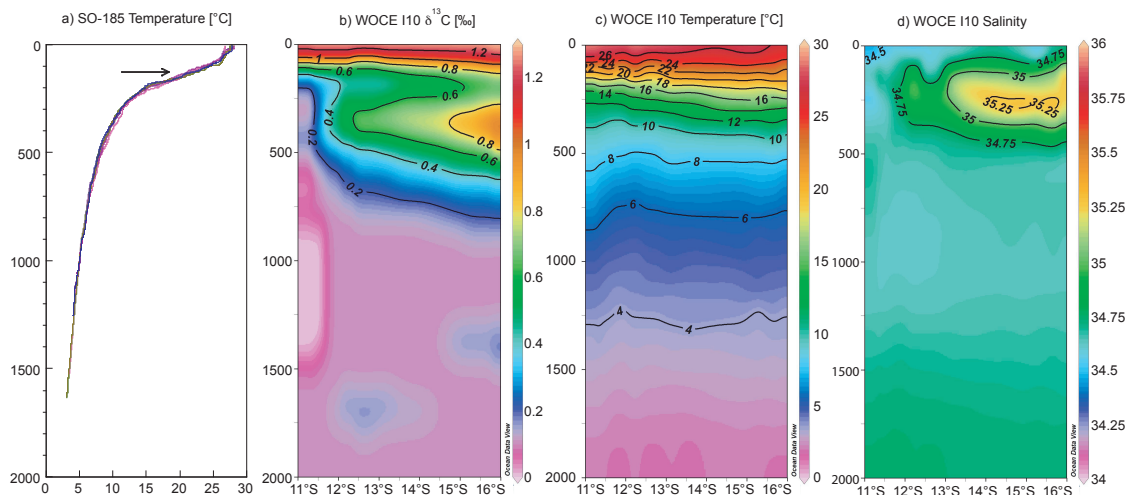


Figure 3.5 (a) Timor Sea temperature profiles obtained in September 2005 during SO-185 cruise (Kuhnt, 2005) indicates temperature difference of $\approx 5^\circ\text{C}$ between surface and upper thermocline. Shaded bar indicates extent of thermocline with arrow at base of upper thermocline, where *P. obliquiloculata* calcifies (Ravelo and Fairbanks, 1992; Cléroux et al., 2007); (b) Temperature profile along WOCE Line i10 (plotted section starts from South Java); (c) $\delta^{13}\text{C}$ profile along WOCE Line i10; (d) Salinity profile along WOCE Line i10. WOCE data are available at <http://doi.pangaea.de/10.1594/PANGAEA.277652>.

(2007) also inferred *P. obliquiloculata* living within the seasonal thermocline, which in the Timor Sea is between 50 and 250 m (CTD data from SO-185 cruise).

Several lines of evidence also support that temperature estimates derived from *P. obliquiloculata* in Core MD01-2378 do not relate to changes in habitat depth but to temperature variations occurring within the upper thermocline. Firstly, a comparison of CTD temperature profiles from the Timor Sea with temperature estimates of *P. obliquiloculata* from 33 Timor Sea core tops confirms that an estimated habitat depth below 100 m for *P. obliquiloculata* is reasonable for the present day in this area (Table 3.1). Secondly, the overall $\delta^{13}\text{C}$ gradient between *G. ruber* (white) and *P. obliquiloculata* does not deviate substantially from $\approx 0.5\text{‰}$ throughout MIS 3 (Figure 3.4), supporting that the respective habitat depths of *P. obliquiloculata* and *G. ruber* (white) remained overall quite consistent over this extended interval. Finally, $\delta^{13}\text{C}$ and temperature do not covary during MIS 3, which would be expected if *P. obliquiloculata* migrated through the upper water column and thus reflected ambient temperature and $\delta^{13}\text{C}$ gradients. For instance, temperature increases during HEs coincide with no significant change or even with slight decreases in $\delta^{13}\text{C}$ (Figures 3.3–3.4).

3.4.2 Decrease in ITF intensity during Heinrich events

A striking feature of the Timor Sea record over MIS 3 is the contrast between the benthic and planktonic oxygen isotope signals (Figures 3.2–3.3). Whereas benthic $\delta^{18}\text{O}$ captures Antarctic warming and cooling trends including the AIM 4 and A 1 to A 4 warm events, planktonic $\delta^{18}\text{O}$

shows closer similarity to Northern Hemisphere records (Dürkop *et al.*, 2008, see Chapter 2). For instance, increases in $\delta^{18}\text{O}$ *G. ruber* (white) of $\approx 0.1\text{--}0.2$ ‰ are registered during stadials HEs 3–6, which also correspond to the early phases of warming in Southern Hemisphere A 1–4 events. This distinct out of phase relationship between benthic and planktonic $\delta^{18}\text{O}$ events was previously interpreted as a bipolar climate seesaw, as Northern Hemisphere cooling/ warming is balanced by Southern Hemisphere warming/cooling (Broecker, 1998; Shackleton *et al.*, 2000).

However, our SST record indicates little change during stadials and interstadials, implying that $\delta^{18}\text{O}$ *G. ruber* (white) maxima during HEs 3–6 are mainly due to $\delta^{18}\text{O}_{sw}$ increases, as shown in Figure 3.2. Tropical records from the West-Pacific warm pool region also revealed that stadials were characterized by heavier $\delta^{18}\text{O}_{sw}$ in surface-dwelling foraminifera. These $\delta^{18}\text{O}_{sw}$ increases were interpreted as a shift towards cooler and drier (El Niño-like) conditions during stadials (Stott *et al.*, 2002; Dannenmann *et al.*, 2003; Rosenthal *et al.*, 2003; Levi *et al.*, 2007). However, the Timor Sea record from Core MD01-2378 additionally displays prominent increases in thermocline temperature and $\delta^{18}\text{O}_{sw}$ during HEs 3–6 (Figures 3.2–3.3). We attribute these changes to an increased influence of warmer, saltier thermocline water from the tropical Indian Ocean and a concurrent decrease in cool, fresh ITF thermocline flow, due to an overall slow-down in the global thermohaline circulation during HEs. The decreased freshwater export from the North Pacific would additionally contribute to higher salinity ($\delta^{18}\text{O}_{sw}$) in the tropical eastern Indian Ocean.

Proxy data and ocean model simulations indicate a near collapse of the MOC during HEs (Sarnthein *et al.*, 1994, 2001; Alley and Clark, 1999; Ganopolski and Rahmstorf, 2001; Broecker, 2003; Piotrowski *et al.*, 2004). Model experiments also predict that a slow-down in the global thermohaline circulation (for instance during the LGM) would result in a weaker ITF, which in turn would diminish the southward flowing Leeuwin Current and the fresh and cool thermocline flow feeding the South Equatorial Current (De Deckker *et al.*, 2003; Gordon, 2005). Today, the southern front of the cool and fresh thermocline water mass, which is injected into the eastern equatorial Indian Ocean by the ITF, is located at approximately 13–14°S (World Ocean Atlas 2005 data, Gordon, 2005; Locarnini *et al.*, 2006; Antonov *et al.*, 2006), close to the position of Core MD01-2378. During periods of reduced thermohaline circulation and weakened ITF flow, this front might have moved northwards. Thus, the location of Core MD01-2378 became increasingly influenced by relatively warm, salty thermocline water from the Indian Ocean rather than by cooler, fresher thermocline water flowing out of the Indonesian seas into the Timor Sea.

The pace and amplitude of thermocline warming and $\delta^{18}\text{O}_{sw}$ changes differed significantly during successive HEs. The most sustained episode of ITF weakening and thermohaline slow-down occurred at the end of MIS 4 and through HE 6, as indicated by highest temperature and $\delta^{18}\text{O}_{sw}$ values persisting over ≈ 3 kyr (Figure 3.3). Sharp drops in thermocline temperature and $\delta^{18}\text{O}_{sw}$ occurred only at ≈ 58.5 ka, which is ≈ 1 kyr later than the end of HE 6. The early part of HE 5 was characterized by minimum thermocline temperature values and low $\delta^{18}\text{O}_{sw}$, marking the end of a long-term increase in ITF intensity from ≈ 60 to 47 ka before a sharp decrease in ITF flow towards the end of HE 5. HEs 3–4 also coincided with prominent decreases in ITF flow, however the declines in ITF intensity occurred more gradually over these stadial events. For HE 4,

the decrease in ITF flow was maintained for a few hundred years after the end of the stadial, which is not surprising, as HE 4 is considered the most intense of the six Heinrich layers in the North Atlantic ([Hemming, 2004](#)).

3.4.3 Main controls of ITF variability during MIS 3

Global changes in thermohaline circulation evidently exert a major control on ITF variability, as demonstrated by the prominent decreases in outflow intensity registered during HEs 3–6. However, the different expression of HEs as well as the longer trends of ITF variability detected in our Timor Sea record suggest that the strength of the thermohaline circulation is not the sole control on ITF intensity and that additional factors may also play a significant role. Today, links between wind surges from the South China Sea prior to and during the onset of the Australian monsoon provide evidence for cross-equatorial atmospheric connections between the Asian winter monsoon and Australian summer monsoon ([Suppiah, 1998](#)). During MIS 3, such cross-equatorial connections would have effectively linked ITF outflow intensity to rapid, large-amplitude climate events in the Northern Hemisphere high latitudes. Intensification of the Australian monsoon triggered by episodes of northern hemisphere cooling would have piled up water masses in the eastern Indian Ocean, thus decreasing further the ITF outflow into the Timor Sea during HEs.

A unique feature of the ITF is the enroute alteration of inflowing Pacific water into a strongly stratified thermocline dominated flow at the southern end of the Makassar Strait ([Gordon, 2005](#)). This change in ITF vertical structure is dependent on sea level and the strength of the SE Asian boreal winter monsoon. Today, thermocline flow of relatively cool water dominates during boreal winter, as the warm surface flow becomes blocked by the development of a fresh water plug at the southern tip of the Makassar Strait, driven by monsoonal winds from the South China Sea through the Java Sea ([Gordon et al., 2003](#)). As a result, the ITF becomes cooler, fresher, and dominated by thermocline rather than surface flow ([Gordon et al., 2003](#)). However, this mechanism requires an open marine connection between the South China and Java Seas over a flooded Sunda shelf, which relates to a sea level position of at least 80 m above the LGM sea level, equivalent to the present day sill depth of the Karimata Strait (≈ 40 m).

Comparison of sea level reconstructions for MIS 3 indicates that this threshold was not reached during MIS 4, most of MIS 3 and the LGM (Figure 3.6). However, significant freshwater input may have occurred from Java, Borneo and Sundaland into the Java Sea, which increasingly became submerged at times of rising sea level during MIS 3. The most recent sea level curves ([Siddall et al., 2003](#); [Arz et al., 2007](#)) indicate that the shelf of the Java Sea became flooded in the early part of MIS 3 (after ≈ 60 ka), as sea level reached 60–70 m below present day level. The long-term increasing trend of thermocline cooling from 60 to 47 ka (Figure 3.3) may have been driven by the establishment of the Java Sea freshwater export, as sea level rose following the MIS 4 lowstand. Intensified SE Asian winter monsoon linked to increasing insolation during this interval ([Wang et al., 2001](#)) would have additionally enhanced the thermocline cooling trend (Figure 3.6). This effect even continued in the early part of HE 5, as the onset of ITF slow-down appears delayed

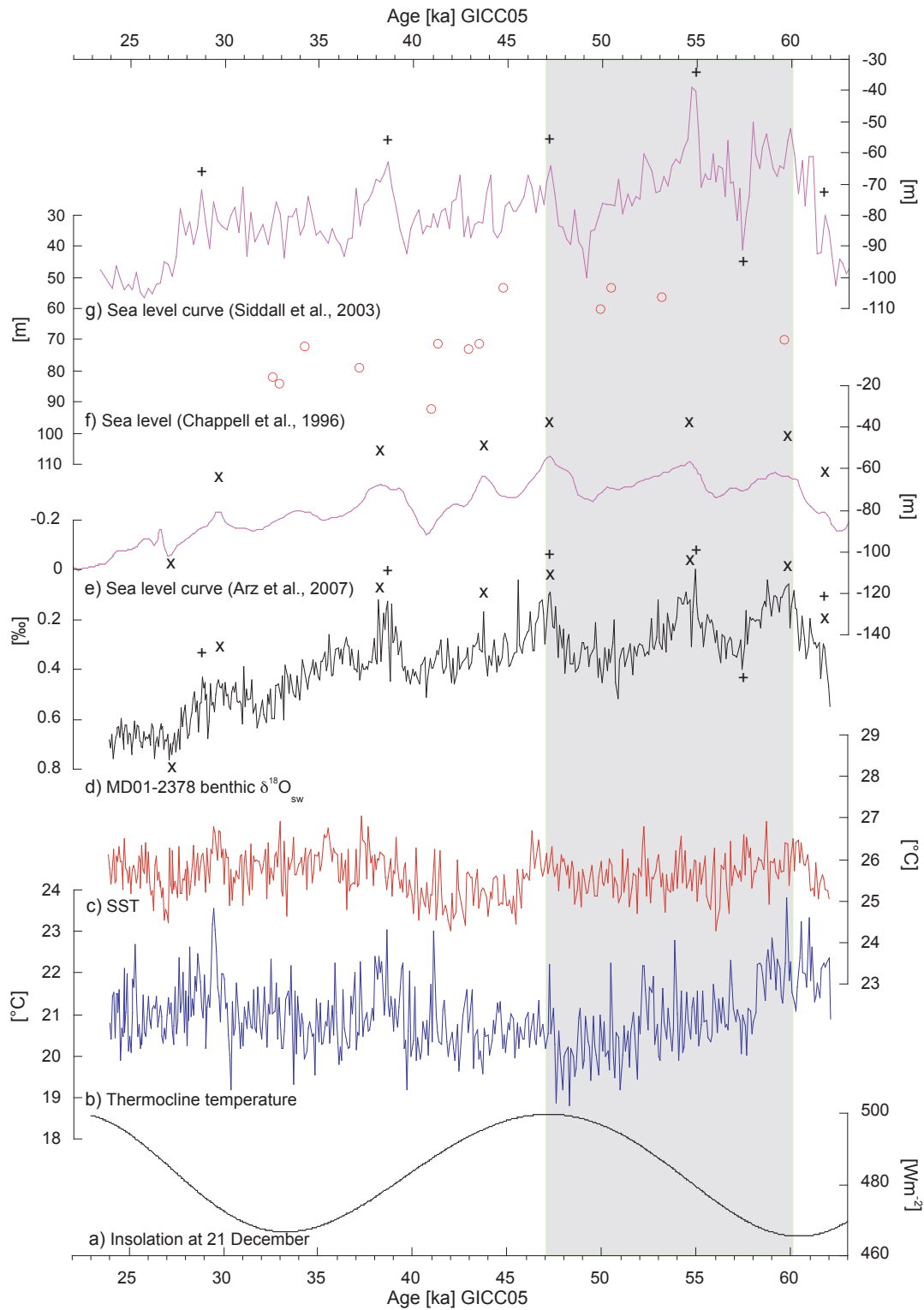


Figure 3.6 Comparison of sea level reconstructions, benthic $\delta^{18}\text{O}_{sw}$, temperatures and insolation during MIS 3. (a) December 21 maximum insolation at 25°S ; (b) *P. obliquiloculata* Mg/Ca derived upper thermocline temperature; (c) *G. ruber* (white) Mg/Ca derived SST; (d) benthic $\delta^{18}\text{O}_{sw}$, + indicates tie points to sea level curve from central Red Sea (Siddall et al., 2003), x indicates tie points to sea level curve from northern Red Sea (Arz et al., 2007); (e) Sea level curve from northern Red Sea (Arz et al., 2007) tuned to MD01-2378 to maintain chronological consistency; (f) coral-based sea level data from Huon Peninsula plotted on independent age scale (Chappell et al., 1996); (g) sea level curve from central Red Sea (Siddall et al., 2003) tuned to MD01-2378 to maintain chronological consistency. Thermocline cooling coincident with rising sea level (≈ 60 m below present) and increasing insolation over Australia in the early part of MIS 3 (60–47 ka) is indicated by grey bar.

during this HE. However, thermocline cooling stopped rather abruptly at the end of HE 5, and the intensity of the thermocline outflow remained overall decreased after HE 5 (Figure 3.3). After 47 ka, peak insolation over the neighboring Australian continent appears to have strongly influenced the hydrography of the Timor Sea (Figure 3.6). The sharp decrease in ITF intensity at the end of HE 5, which interrupts the long-term thermocline cooling trend from ≈ 60 to 47 ka occurs ≈ 1 kyr before a prominent surface cooling at 46 ka, lasting until 40 ka. *Dürkop et al.* (2008, see Chapter 2) interpreted this event as the intrusion of a cold surface water tongue with increased influence of cooler, more nutrient rich waters from the West Australian Current and overall weakening of the ITF. The maximum in austral summer (21. December, 25° S) insolation at 47 ka would have favored the intensification of monsoonal winds over northern Australia, and in turn influenced the migration of hydrological fronts between Indian Ocean and ITF derived water masses, thus altering ITF flow and intensity.

3.5 Conclusions

Our high resolution stable isotope and Mg/Ca-records of surface and thermocline dwelling planktonic foraminifera in Core MD01-2378 from the Timor Sea indicate substantial temperature and salinity ($\delta^{18}\text{O}_{sw}$) changes in ITF outflow water masses during HEs 3–6. We interpret thermocline warming during HEs 3–6 as evidence for the increased influence of warmer, saltier thermocline water from the tropical Indian Ocean and attendant decrease in cool, fresh ITF thermocline flow, due to an overall slow-down in the global thermohaline circulation during HEs 3–6. These changes in the ITF structure and intensity during HEs must have had far reaching repercussions on the hydrography of the tropical Indian Ocean as well as regional and global climate evolution. The resulting warmer and saltier eastern tropical Indian Ocean would have in turn strongly influenced the Asian Monsoon system and significantly altered the heat and energy budget within the 'warm' return branch of the global thermohaline circulation.

Three main factors appear to have influenced ITF variability during MIS 3: (1) global slow-down in thermohaline circulation during HEs, triggered by northern hemisphere cooling and restricted deep water formation in the North Atlantic; (2) increased freshwater export from the Java Sea into the ITF during the early part of MIS 3, principally controlled by sea level and (3) insolation related changes in Australasian monsoonal intensity leading to the migration of hydrological fronts between Indian Ocean and ITF derived water masses at 46–40 ka. The complex interplay between these factors resulted in a unique pattern of ITF variability during MIS 3, which differs from changes recorded on glacial-interglacial timescales. Previous work focusing on Terminations I and II indicated that an overriding control of ITF thermocline flow intensity during terminations was the establishment of an open connection through the Java Sea to the South China Sea, when sea level reached ≈ 40 m below present, in conjunction with a fully developed Australasian monsoonal system (*Xu et al.*, 2008). Such conditions were only reached at peak interglacials during MIS 5e and the late Holocene.

3.6 Acknowledgments

We thank Franck Bassinot, Yvon Balut and the crew of the RV 'Marion Dufresne' for their efforts during the WEPAMA Cruise and the Institut Polaire Français Paul Emile Victor for support. We are grateful to Gerald Dickens and two anonymous reviewers for in depth, constructive reviews and to Jian Xu, Marcus Regenberg, Andre Bahr for helpful comments. Dieter Garbe-Schönberg, Nadine Gehre, Karin Kissling and Lulzim Haxhijaj provided analytical expertise and technical assistance. We gratefully acknowledge the Deutsche Forschungsgemeinschaft (DFG) for funding this research (Grant Ku 649/25-1) and the German Ministry for Education, Science and Technology (BMBF Grant 03GO185B) for funding the Sonne-185 cruise.

Chapter 4

High-latitude climate signals and monsoon related regional climate variability in the Eastern Indian Ocean during Marine Isotope Stage 3

Anke Dürkop^a, Ann Holbourn^a, Wolfgang Kuhnt^a, Jian Xu^b, Nils Andersen^c, Pieter M. Grootes^c

^aInstitute of Geosciences, Christian-Albrechts-University, Ludewig-Meyn-Str. 10-14, D-24118 Kiel, Germany

^bDepartment of Geology, Northwest University, 229 North Taibai Rd., 710069 Xi'an, Shaanxi, P. R. China

^cLeibniz-Laboratory for Radiometric Dating and Stable Isotope Research, Christian-Albrechts-University, Max-Eyth-Str. 11 - 13, D-24118 Kiel, Germany

Manuscript for submission

Abstract. We present a high-resolution (≈ 60 – 110 yr) multi-proxy record spanning Marine Isotope Stage 3 (MIS 3) from Core SO-185 18460 located in the Timor Passage at 1875 m water depth. It monitors high-latitude climate variability and interhemispheric coupling on millennial and (semi-) precessional timescales at a key position within the global thermohaline circulation. Benthic oxygen and carbon isotope records are correlated with Southern Hemisphere high-latitude Antarctic Isotope Maxima, which are supposed to be transmitted by a southern sourced intermediate and deep water mass. This water mass apparently affected the studied site with abrupt retreats during stadials. In contrast the planktonic oxygen isotope record corresponds to Northern Hemisphere high-latitude Dansgaard-Oeschger (D-O) events probably transmitted through the East Asian-Australian monsoon system. The position of Core SO-185

18460 detected different monsoon conditions during MIS 3 on (semi-) precessional and millennial timescales. Benthic foraminiferal census counts additionally reflect (semi-) precessional variations in paleoceanographic reorganization and stadial to interstadial changes in bottom water circulation.

4.1 Introduction

Rapid climate oscillations on millennial timescales dominated the last glacial period and have been largely documented in Greenland ice cores (*Johnsen et al., 1992; Dansgaard et al., 1993; Grootes et al., 1993*) and in sediment cores from the adjacent North Atlantic (*van Kreveld et al., 2000*) and the Iberian Margin (*Shackleton et al., 2000; Martrat et al., 2007*), but were also recorded in many other localities of the Northern Hemisphere (*Schulz et al., 1998; Wang et al., 2001; Voelker and workshop participants, 2002*). These interstadials called Dansgaard-Oeschger (D-O) events are reflected as a rapid temperature increase by 8–16 °C (*Landais et al., 2004; Huber et al., 2006*) within a few decades followed by a gradual temperature decrease back to stadial conditions within approximately 1000–3000 yr. Longer-lasting D-O events are preceded by ice rafted debris events (*Bond and Lotti, 1995*) identified as "Heinrich-layers" in North Atlantic marine sediment cores (*Heinrich, 1988*). Such "Heinrich-layers" complete Bond cycles, which are bundles of D-O events with one longer warm period followed by up to three shorter warm periods separated from each other by cold periods (*Bond and Lotti, 1995*).

The Southern Hemisphere experienced gradual increases and decreases in temperatures as recorded in Antarctic ice cores (*Johnsen et al., 1972; Jouzel et al., 1987; Blunier et al., 1998; Blunier and Brook, 2001*). These Antarctic ice core records have been synchronized to those from Greenland by *Blunier et al. (1998)* and *Blunier and Brook (2001)* using variations in the concentration of atmospheric methane as preserved in gaseous inclusions. These authors showed that during the onset of an Antarctic warm event Greenland temperatures were still decreasing or constant, and that Antarctic warm events led to longer-lasting Greenland interstadials. This is supported by the study of *Wolff et al. (2009)* showing that the Southern Hemisphere generates warmings but Northern Hemisphere conditions prevent further progress in Southern Hemisphere warmings and control shifts to interstadial states. An one-to-one coupling of Antarctic warm events to longer-lasting and shorter D-O events in Greenland ice cores was established by a high-resolution Antarctic ice core record (*EPICA Community Members, 2006*) resolving also low-magnitude temperature variability from EPICA Dronning Maud Land (EDML). Thereby the new nomenclature of "Antarctic Isotope Maximum" (AIM) as synonym for Antarctic warm events was introduced (*EPICA Community Members, 2006*). This EDML ice core and the Northern Hemisphere Greenland Ice Core (*NGRIP members, 2004*) based on the same timescale, the Greenland Ice Core Chronology (GICC05) developed by *Andersen et al. (2006)* and *Svensson et al. (2006, 2008)*, give the opportunity to evaluate climate variability in high-resolution marine sediment records from low-latitudes with stadial-interstadial climate conditions in Northern and Southern Hemisphere high-latitudes during MIS 3.

The ice core studies by *Blunier et al. (1998)*, *Blunier and Brook (2001)* and *EPICA Community*

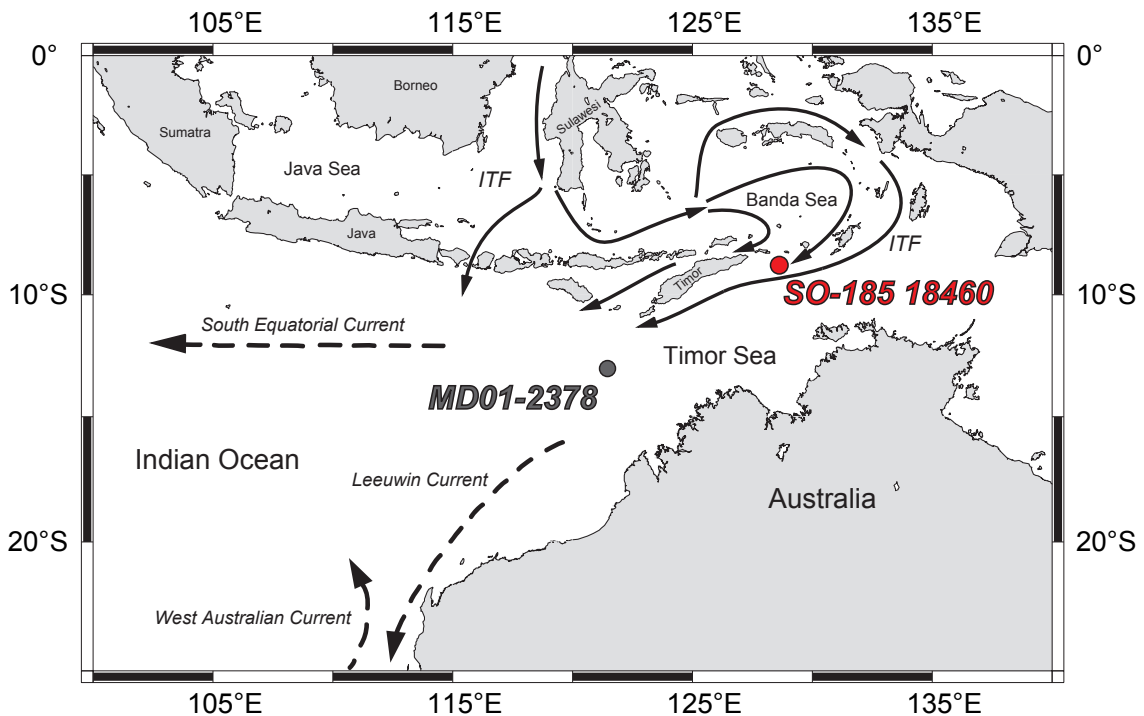


Figure 4.1 Location of Cores SO-185 18460 (8° 47.386' S, 128° 38.485' E, 1875 m water depth) and MD01-2378 (13° 04.95' S, 121° 47.27' E, 1783 m water depth; *Dürkop et al., 2008*) in the Timor Sea. Solid arrows indicate main pathways of the Indonesian Throughflow (=ITF, after *Gordon, 2005*). Dashed arrows indicate the South Equatorial Current, Leeuwin Current and West Australian Current.

Members (2006) support the idea of an anti-phase relationship on millennial timescales between warming and cooling events in the Southern and Northern Hemispheres, which was interpreted as a bipolar climate seesaw (*Broecker, 1998*). This phase relationship has also been detected in cores from the Iberian Margin, where the onsets of gradual warm events in benthic $\delta^{18}\text{O}$ with lower range of variations led rapid cold-to-warm transitions in planktonic $\delta^{18}\text{O}$ (*Shackleton et al., 2000; Martrat et al., 2007*). The benthic $\delta^{18}\text{O}$ record could not be directly converted into sea level due to unlikely rapid mixings of ice volume signals through the ocean. Hence, these benthic oxygen isotope records have been interpreted as Antarctic temperature excursions (*Shackleton et al., 2000*, and citations therein). In contrast Greenland temperatures were represented by the respective planktonic oxygen isotopes. Furthermore *Martrat et al. (2007)* used benthic $\delta^{13}\text{C}$ records to determine changes in the origin of ventilated deep water masses reaching the Iberian Margin and changing conditions linked to the global thermohaline circulation (THC).

To retrace the development of circulation changes during MIS 3 in the Eastern Indian Ocean with a probable reorganization of Southern Ocean water masses (*Wells and Wells, 1994; Holbourn et al., 2005; Dürkop et al., 2008; Zuraida et al., 2009*) it is necessary to understand the Northern and Southern Hemisphere climate interaction and the role of the THC. *Marchal et al. (1998)* proposed that the collapse of the THC would lead to a strong cooling in the northern North Atlantic

(>20°N). This cooling will be balanced by a warming in the Southern Ocean where the Southern Ocean heat will be released to the atmosphere due to a large convective event (Marchal *et al.*, 1998; Adkins *et al.*, 2005). During this onset of increasing temperatures in Antarctica, Greenland temperatures are still decreasing (Blunier *et al.*, 1998). While Antarctic temperatures are still rising and reaching maximum values reflected as an AIM event the onset of a D-O event in the Northern Hemisphere takes place and leads to an interruption of Antarctic warming (Blunier *et al.*, 1998). During these D-O events Greenland temperatures increase to interstadial conditions within only a few decades (Grootes *et al.*, 1993), and the THC begins to intensify rapidly, recovering its original intensity in a few hundred years (Manabe and Stouffer, 1997). Following the study of Schmittner *et al.* (2007) an intensified THC would then lead to a reduced circulation of Southern Ocean water masses with decreasing oxygen concentrations in the Indo-Pacific.

Dürkop *et al.* (2008) (see Chapter 2) have shown that the benthic $\delta^{18}\text{O}$ data of *Planulina wuellerstorfi* (*P. wuellerstorfi*) of Core MD01-2378 located in the outflow region of the Indonesian Throughflow (ITF) (Figure 4.1) clearly reflect a high-latitude Southern Hemisphere signal, transmitted via deep and intermediate water masses. In contrast the planktonic $\delta^{18}\text{O}$ data of *Globigerinoides ruber* white (*G. ruber*) show close affinity to high-latitude Northern Hemisphere climate variability probably transmitted through atmospheric teleconnections and a coupling to the East Asian-Australian monsoon system. The ITF represents a major component of the global THC transporting water masses from the Pacific into the Indian Ocean. While passing the Indonesian Archipelago it affects local and regional climate on interannual and longer timescales (Schott and McCreary Jr., 2001). Furthermore the Indonesian Archipelago and the Eastern Indian Ocean are climate sensitive due to the migration of the Intertropical Convergence Zone (ITCZ) and the related monsoonal influence.

To illuminate an understanding of this climate sensitive area during MIS 3 a comparison of two adjacent high-resolution multi-proxy records from the Timor Sea was performed (Figure 4.1). Benthic and planktonic foraminiferal oxygen and carbon isotope values are studied to distinguish between high-latitude and regional climate signals. Benthic Foraminiferal Accumulation Rates (BFAR) are used to determine regional differences in foraminiferal abundances and possible changes in regional paleoceanography and monsoon related paleoproductivity variations.

4.2 Oceanographic and climate setting

SONNE Core SO-185 18460 (8° 47.386' S, 128° 38.485' E, 1875 m water depth) was recovered in September 2005 in the Timor Passage (Figure 4.1) eastward off Timor. At this key area of the global conveyor belt the modern total ITF transports an annual average of ≈ 16 Sv (1 Sv = $10^6 \text{ m}^3 \text{ s}^{-1}$) low-saline tropical waters from the western Pacific into the Eastern Indian Ocean, feeding the South Equatorial Current and Leeuwin Current (Tomczak and Godfrey, 2003; Talley and Sprintall, 2005). The low-saline LC flows along the Western Australian coast into the Great Australian Bight (Pearce and Cresswell, 1985), whereas relatively cool, high-saline water is transported northward by the undercurrent (Cresswell, 1991), which is linked to the eastern com-

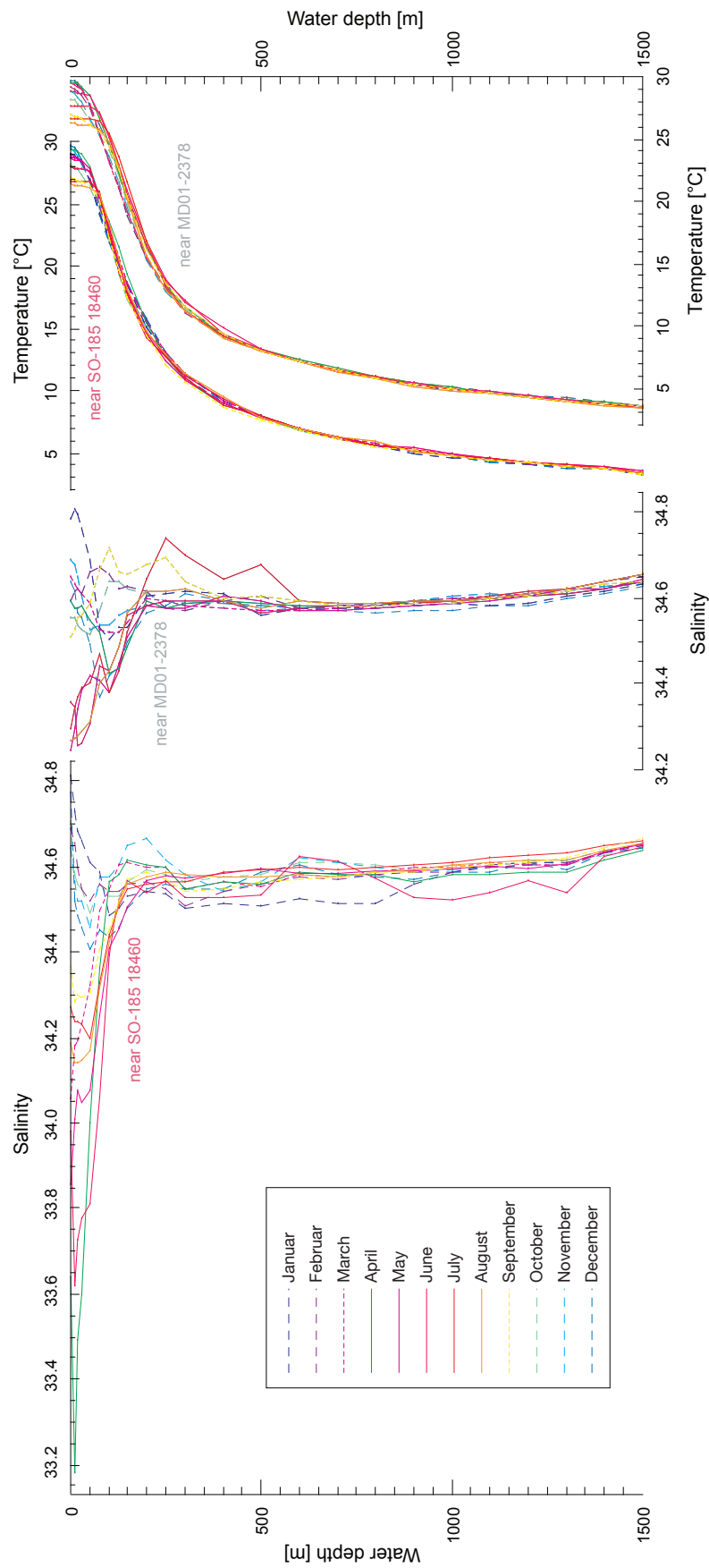


Figure 4.2 Modern monthly temperature and salinity profiles vs. water-depth (National Oceanographic and Data Center; *NODC, 2001*) near sites SO-185 18460 (Timor Passage; 8.5° S, 128.5° E) and MD01-2378 (ITF outflow region; 13.5° S, 121.5° E). 1x1° gridded values are averaged for water depths in intervals of 10 m (0–30 m), 25 m (50–150 m), 50 m (200–300 m) and 100 m (400–1500)

ponent of the Southern Hemisphere subtropical gyre forming the West Australian Current (WAC).

The total ITF is composed of the upper layer Indonesian Throughflow Water and the deeper layer Indonesian Intermediate Water (IIW), which is low-saline and of Pacific and Indonesian origin (*Talley and Sprintall, 2005*). Entering the Timor Sea via Leti Strait at a sill depth of ≈ 1250 m the IIW reaches depths below ≈ 1100 m in the ITF outflow area (*Koch-Larrouy et al., 2008; van Aken et al., 2009*). Northeastward directed inflow into the Timor Trough between ≈ 1500 m and ≈ 1890 m (West Timor sill depth) reverses to exit back into the Indian Ocean below ≈ 1300 m (*Sprintall et al., 2009*).

Today the study area is influenced by the biannual migration of the ITCZ and the related East Asian-Australian monsoon system. During austral summer the ITCZ is located over northern Australia causing the NW-monsoon with relatively wet conditions. In contrast austral winter is characterized by dry SE-monsoon conditions due to the northward shift of the ITCZ beyond the Equator (*van der Kaars et al., 2000*). The Maritime Continent, in particular the Indonesian Archipelago, is characterized by strong regional differences in precipitation patterns during the generally dry (May-September), transition (April, October, November) and wet (December-March) months as documented by *Tapper (2002, and references therein)*. However, modern sea-surface salinity profiles (National Oceanographic and Data Center, *NODC, 2001*) at the coring sites SO-185 18460 and MD01-2378 (Figure 4.1) show increased values during austral summer and decreased values during winter (Figure 4.2). An explanation for the time lag between the rainfall (December-February) related to NW-monsoon conditions and lowest salinity values at site SO-185 18460 (April-August) may be fresh surface water derived from the Java Sea with a phase lag of several months (*Atmadipoera et al., 2009*).

In detail site SO-185 18460 (MD01-2378) exhibits lowest salinity values of ≈ 33.9 (≈ 34.4) during the NW-monsoon season/ austral summer and highest salinity values of ≈ 34.8 (≈ 34.7) during the SE-monsoon season/ austral winter (National Oceanographic and Data Center, *NODC, 2001*). This implies for both sites similar salinity conditions during October-February and different for April-August. Figure 4.2 illustrates similar temperature profiles for both sites and the same seasonal differences at the sea surface of ≈ 2.5 °C.

4.3 Material and method

4.3.1 Stable isotope values

Core SO-185 18460 was sampled at 1 cm intervals between 352 and 835 cm and at 4 cm intervals between 252 and 352 cm (47.5 cm^3 from 1 cm thick sediment slices). Samples were dried and weighed, then washed over a $63 \mu\text{m}$ sieve. Residues were dried on a sheet of filter paper and weighed, then sieved into $63\text{--}150 \mu\text{m}$, $150\text{--}250 \mu\text{m}$, $250\text{--}315 \mu\text{m}$, and $>315 \mu\text{m}$ fractions. For stable isotope analysis, we selected per sample 3 to 5 tests ($>250 \mu\text{m}$) of the epibenthic foraminifera *P. wuellerstorfi* and 20 tests ($250\text{--}315 \mu\text{m}$) of the planktonic foraminifera *G. ruber*. In case of low benthic foraminiferal density smaller numbers (1–2) of specimens were analyzed.

Tests with cement encrustations and infillings were discarded, eligible tests were broken into large fragments, then cleaned in ethanol in an ultrasonic bath and dried at 40 °C. Stable carbon and oxygen isotope measurements were made with the Finnigan MAT 251 mass spectrometer at the Leibniz Laboratory, Christian-Albrechts-University of Kiel. The instrument is coupled online to a Carbo-Kiel Device (Type I) for automated CO₂ preparation from carbonate samples for isotopic analysis. Samples were reacted by individual acid addition. The mean external error and reproducibility of carbonate standards is better than $\pm 0.07\text{‰}$ and $\pm 0.05\text{‰}$ for $\delta^{18}\text{O}$ and $\delta^{13}\text{C}$, respectively. Results were calibrated using the National Institute of Standards and Technology (Gaithersburg, Maryland) carbonate isotope standard NBS 20 and in addition NBS 19 and 18, and are reported on the PeeDee belemnite (PDB) scale.

Replicate measurements on 48 paired samples of *P. wuellerstorfi* indicate that the mean reproducibility is better than $\pm 0.06\text{‰}$ for $\delta^{18}\text{O}$ and $\delta^{13}\text{C}$, respectively. For the planktonic foraminifera *G. ruber*, the reproducibility is better than $\pm 0.07\text{‰}$ for $\delta^{18}\text{O}$ and $\pm 0.09\text{‰}$ for $\delta^{13}\text{C}$ in 57 paired measurements.

For comparison of both sites within the Timor Passage and Timor Sea differences between records from Cores SO-185 18460 and MD01-2378 of benthic and planktonic oxygen and carbon isotopes ($\Delta\delta^{18}\text{O}$, $\Delta\delta^{13}\text{C}$). A continuous 3 point running mean was applied for curve smoothing. Additionally $\Delta\delta^{18}\text{O}_{sw}$ and ΔSST were calculated using Magnesium/Calcium derived oxygen isotope data of seawater and sea-surface temperature (Zuraida, unpublished data). Due to resolution changes within these two records a 3 point smooth was only applied to time slices with high-resolution (=measurements in 1 cm depth intervals).

Afterwards the smoothed data have been interpolated from point to point in Kaleidagraph Version 4 by using a Stineman function (Stineman, 1980), which passes through the data points and matches the slopes at those points. To obtain records for both sites on exact the same timescale with equidistant increments, these interpolated curves have been sampled at every 50 yr. Finally the Δ -values have been derived by subtracting MD01-2378 from SO-185 18460 data.

4.3.2 Accelerator mass spectrometry

For this study six samples of Core SO-185 18460 were ¹⁴C dated by accelerator mass spectrometry (AMS). Each sample consisted of approximately 1100 well preserved tests of the planktonic foraminifera *G. ruber* picked from the >250 μm fraction at levels, where

Table 4.1 AMS ¹⁴C dates measured on *G. ruber* in Core SO-185 18460

| Lab Code | Sample (Core SO-185 18460) | ¹⁴ C-Conventional age (BP) | CAL-age (BP) |
|-----------|----------------------------|---------------------------------------|--------------|
| KIA 30821 | 200 cm, 1.1 mg C | 11050 ± 50 | 12677 ± 49 |
| KIA 33792 | 240 cm, 1.4 mg C | 13990 ± 70 | 15935 ± 134 |
| KIA 30822 | 320 cm, 1.1 mg C | 18370 ± 100 | 21044 ± 162 |
| KIA 30823 | 350 cm, 1.2 mg C | 19800 ± 120 | 22801 ± 166 |
| KIA 30824 | 390 cm, 1.1 mg C | 21810 + 150/ -140 | 25404 ± 221 |
| KIA 30825 | 420 cm, 1.2 mg C | 23720 ± 190 | 27743 ± 255 |

G. ruber showed high abundances to minimize bioturbation effects. AMS ^{14}C ages (Table 4.1) were determined at the Leibniz Laboratory, Christian-Albrechts-University of Kiel using standard methods described by *Nadeau et al. (1997)* and *Schleicher et al. (1998)*. Calendar ages were calculated with the radiocarbon calibration program of *Fairbanks et al. (2005)* (<http://www.radiocarbon.ldeo.columbia.edu/research/radiocarbon.htm>), after applying simulated surface water reservoir age corrections following *Butzin et al. (2005)*. Preindustrial (300 yr) and glacial (600 yr) reservoir age corrections were applied for samples above and below 270 cm, respectively (Figure 4.3).

4.3.3 Benthic foraminiferal census counts

For our low-resolution study of benthic foraminiferal census counts as measure of changes in carbon-flux all benthic foraminifera, on average ≈ 300 specimens per sample, were picked and counted in size fractions $>250\ \mu\text{m}$ between 250 and 830 cm every 10 cm. In samples, where the abundance of benthic foraminifera was very high, a quantitative split of the $>250\ \mu\text{m}$ size fractions was picked, and census counts were then reconverted to whole samples. Counts of globocassidulinids include *Globocassidulina subglobosa* and *Globocassidulina elegans*. Buliminid counts include *Globobulimina* spp., *Bulimina aculeata*, *Bulimina marginata* and *Bulimina mexicana* (see Taxonomic list A). 10% of the smaller size fraction (150–250 μm) of all picked samples were scanned to prevent that smaller species were overlooked and excluded from analysis (*Holbourn et al., 2005*; *Dürkop et al., 2008*, see Chapter 2). BFAR (number of specimens $>250\ \mu\text{m}\ \text{cm}^{-2}\ \text{kyr}^{-1}$) were calculated following *Herguera and Berger (1991)* as the product of the number of benthic foraminifera per gram dry sediment and the sediment accumulation rate (in $\text{g}\ \text{cm}^{-2}\ \text{kyr}^{-1}$). Accumulation rates (AR) of buliminids and globocassidulinids were calculated in the same fashion.

Table 4.2 Tie points between benthic (planktonic) foraminiferal $\delta^{18}\text{O}$ and EDML (NGRIP) ice core $\delta^{18}\text{O}$ versus depth and age

| a) Benthic foraminiferal tie points | | | | |
|---------------------------------------|-----------------------------------|--------------------|------------------------------------|--|
| Core SO-185 18460 | | EDML ice core | | Event |
| Depth [cm] | $\delta^{18}\text{O}$ [‰ vs. PDB] | GICC05 age [ka BP] | $\delta^{18}\text{O}$ [‰ vs. SMOW] | |
| 268 | 4.11 | 18.15 | -49.87 | $\delta^{18}\text{O}$ maximum prior to deglaciation |
| 414 | 3.93 | 27.45 | -50.86 | $\delta^{18}\text{O}$ maximum after AIM 4 event |
| 535 | 3.69 | 36.75 | -49.72 | $\delta^{18}\text{O}$ maximum after AIM 8 event |
| 573 | 3.73 | 39.85 | -49.70 | $\delta^{18}\text{O}$ maximum before AIM 8 event |
| 678 | 3.67 | 48.85 | -49.85 | $\delta^{18}\text{O}$ maximum before AIM 12 event |
| b) Planktonic foraminiferal tie point | | | | |
| Core SO-185 18460 | | NGRIP ice core | | Event |
| Depth [cm] | $\delta^{18}\text{O}$ [‰ vs. PDB] | GICC05 age [ka BP] | $\delta^{18}\text{O}$ [‰ vs. SMOW] | |
| 733 | -1.31 | 54.49 | -42.90 | $\delta^{18}\text{O}$ maximum preceding D-O 14 event |

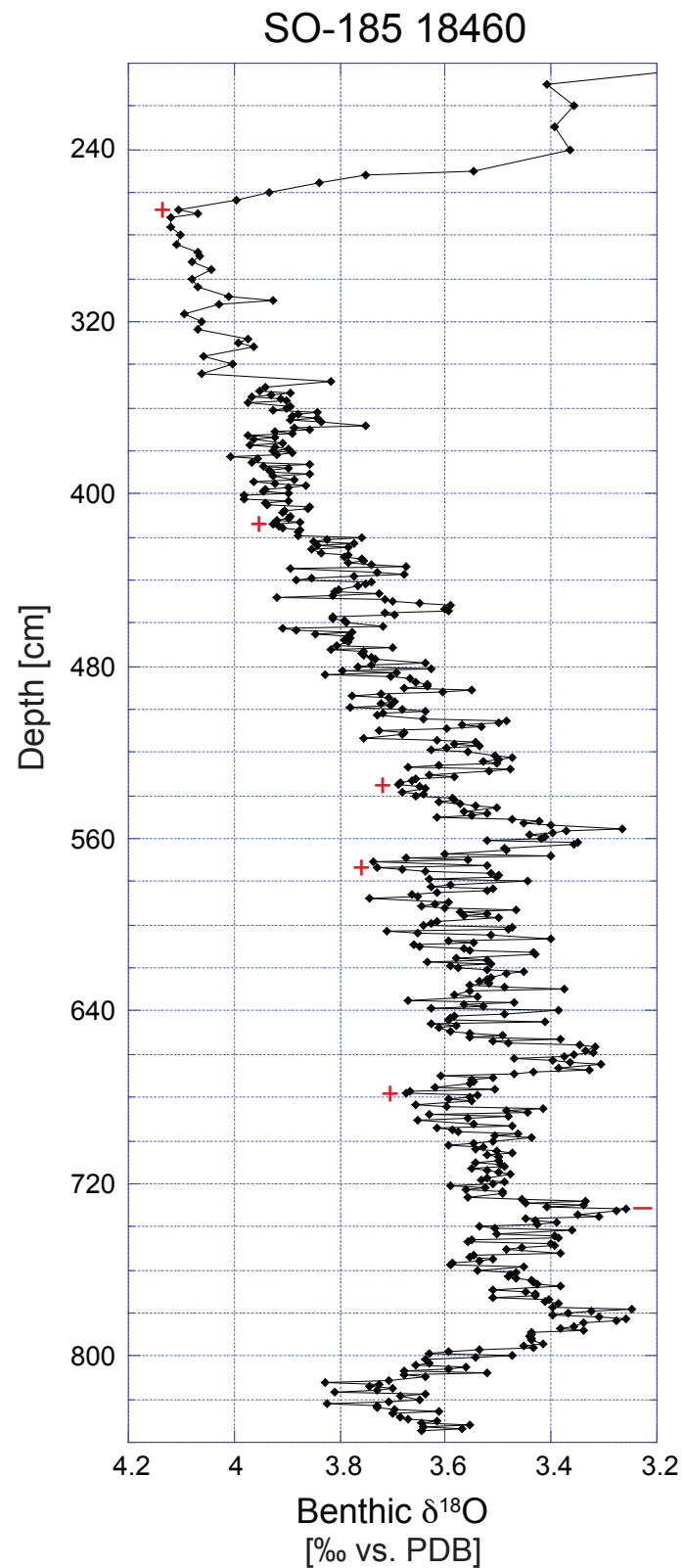


Figure 4.3 Benthic foraminiferal oxygen isotope data versus depth spanning MIS 1–4 (centennial-scale resolution record spanning MIS 3). Tie points are indicated by crosses (dash) between Core SO-185 18460 benthic (planktonic) foraminiferal $\delta^{18}\text{O}$ and the EDML (NGRIP) ice core used as basis for the MIS 3 age model.

We calculated sediment accumulation rates following *van Andel et al. (1975)*. These rates were derived by sedimentation rates based on the age model and an average dry bulk density value of $\approx 0.55 \text{ g cm}^{-3}$. Single sample dry bulk densities were determined by dividing a sample dry weight by a sample volume ($\approx 47.52 \text{ cm}^3$).

4.4 Results

4.4.1 Age model

Our age model of Core SO-185 18460 (Timor Passage) is based on correlation of high-resolution benthic oxygen isotope data to the $\delta^{18}\text{O}$ data of the EDML ice core from Antarctica (*EPICA Community Members, 2004*), and on correlation of planktonic oxygen isotope data to the NGRIP ice core from central Greenland (*NGRIP members, 2004*). This age model is created independently, but in the same fashion as for Core MD01-2378 located within the Timor Sea (*Zuraida et al., 2009*, see Chapter 3). NGRIP and EDML ice cores are dated on the GICC05 timescale, which is based on annual layer counting of three high-resolution ice core records from Greenland (*EPICA Community Members, 2006; Andersen et al., 2006; Svensson et al., 2008*).

Due to their high-resolution and significant amplitude fluctuations the NGRIP and the EDML $\delta^{18}\text{O}$ records give the opportunity to correlate high-resolution marine $\delta^{18}\text{O}$ records from low-latitudes to the respective Northern or Southern Hemisphere climate variations, and hence to assess the stadial-interstadial climate variability at low-latitudes. In detail, five tie points were used to correlate benthic $\delta^{18}\text{O}$ data of Core SO-185 18460 to $\delta^{18}\text{O}$ data of EDML between 18 ka and 49 ka, and one tie point at 55 ka was used to correlate planktonic $\delta^{18}\text{O}$ data of Core SO-185 18460 to $\delta^{18}\text{O}$ data of NGRIP (Figures 4.3–4.5, Table 4.2). An interpolated curve was fitted through all tie points using a Stineman function in Kaleidagraph Version 4 (*Stineman, 1980*), and afterwards this curve was sampled at 1 cm depth intervals to assign respective ages. A change in sedimentation rates from $\approx 10\text{--}16 \text{ cm kyr}^{-1}$ is evident and probably originated from the coring process (*Sz er em eta et al., 2004*). As no isotopic data are published beyond 60 ka (50 ka) for NGRIP (EDML) ice core on the GICC05 timescale (*Svensson et al., 2008*), the lower part of our age model (733–835 cm corresponding to $\approx 55\text{--}65 \text{ ka}$) is based on linear extrapolation.

Additionally six AMS ^{14}C dates measured on *G. ruber* between 12 and 28 ka are used to constrain our age model. During MIS 3 the earth magnetic field showed several episodes of weakness leading to increased production of cosmogenic isotopes and resulting in the occurrence of ^{14}C -inversions, such as the Laschamp Event at around 41 ka (*Voelker et al., 2000; Hughen et al., 2004*). Significant changes in THC intensity occurred during this time interval, in particular during Heinrich events (*NGRIP members, 2004*). Hence, most of the conditions for constant marine reservoir ages do not hold (*Grootes and Sarnthein, 2006; Sarnthein et al., 2007*), and the calibration of AMS ^{14}C dates is still under debate. Despite these uncertainties we can use our AMS ^{14}C based calculated calendar ages to constrain our age model.

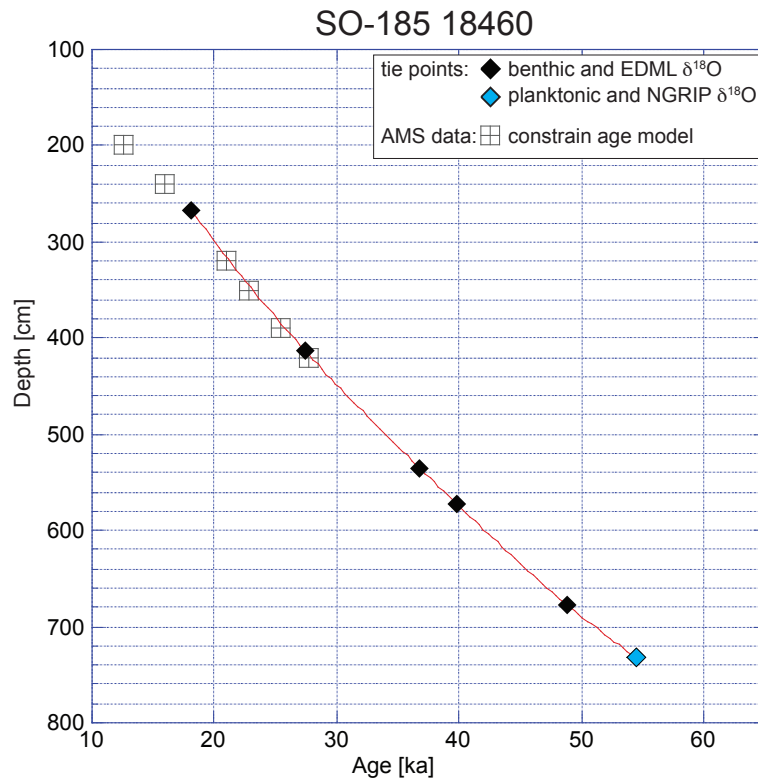


Figure 4.4 Age/ depth plot: black diamonds indicate tie points between EDML ice core and SO-185 18460 benthic foraminiferal $\delta^{18}\text{O}$, and blue diamond between NGRIP ice core and SO-185 18460 planktonic foraminiferal $\delta^{18}\text{O}$. Our age model is further constrained by 6 AMS ^{14}C dates (transparent, crossed squares).

4.4.2 Stable isotope values

Benthic and planktonic foraminiferal $\delta^{18}\text{O}$ records of Core SO-185 18460 indicate complete recovery of a continuous hemipelagic sedimentary succession between 22 and 65 ka, spanning the entire MIS 3 with a time resolution of $\approx 60\text{--}110$ yr (Figures 4.5–4.6). The benthic $\delta^{18}\text{O}$ record varies between $\approx 4.0\text{--}3.3\text{‰}$ exhibiting a maximum amplitude fluctuation of 0.7‰ . This curve reflects four distinct excursions to lower $\delta^{18}\text{O}$ values with a maximum amplitude of about 0.4‰ at ≈ 59 ka, ≈ 54 ka, ≈ 47 ka, and ≈ 39 ka. These benthic oxygen isotope excursions are in time with ice core $\delta^{18}\text{O}$ maxima of Antarctica (*Blunier and Brook, 2001; EPICA Community Members, 2006; Ruth et al., 2007*) and we correlate these four prominent events to the Antarctic warm events A4–A1 following the nomenclature of *Blunier and Brook (2001)*. Due to the high-resolution of recorded $\delta^{18}\text{O}$ in the EDML ice core detecting major (A4–A1) and minor Antarctic warm events during MIS 3 the *EPICA Community Members (2006)* developed the nomenclature of Antarctic Isotope Maximum (AIM). Applying this to our benthic oxygen isotope data AIM 16 (=A4), AIM 14 (=A3), AIM 12 (=A2) and AIM 8 (=A1) are identified (Figure 4.5). Furthermore, seven minor $\delta^{18}\text{O}$ excursions with amplitude fluctuations of $\approx 0.2\text{--}0.3\text{‰}$ to lower $\delta^{18}\text{O}$ values are detected in

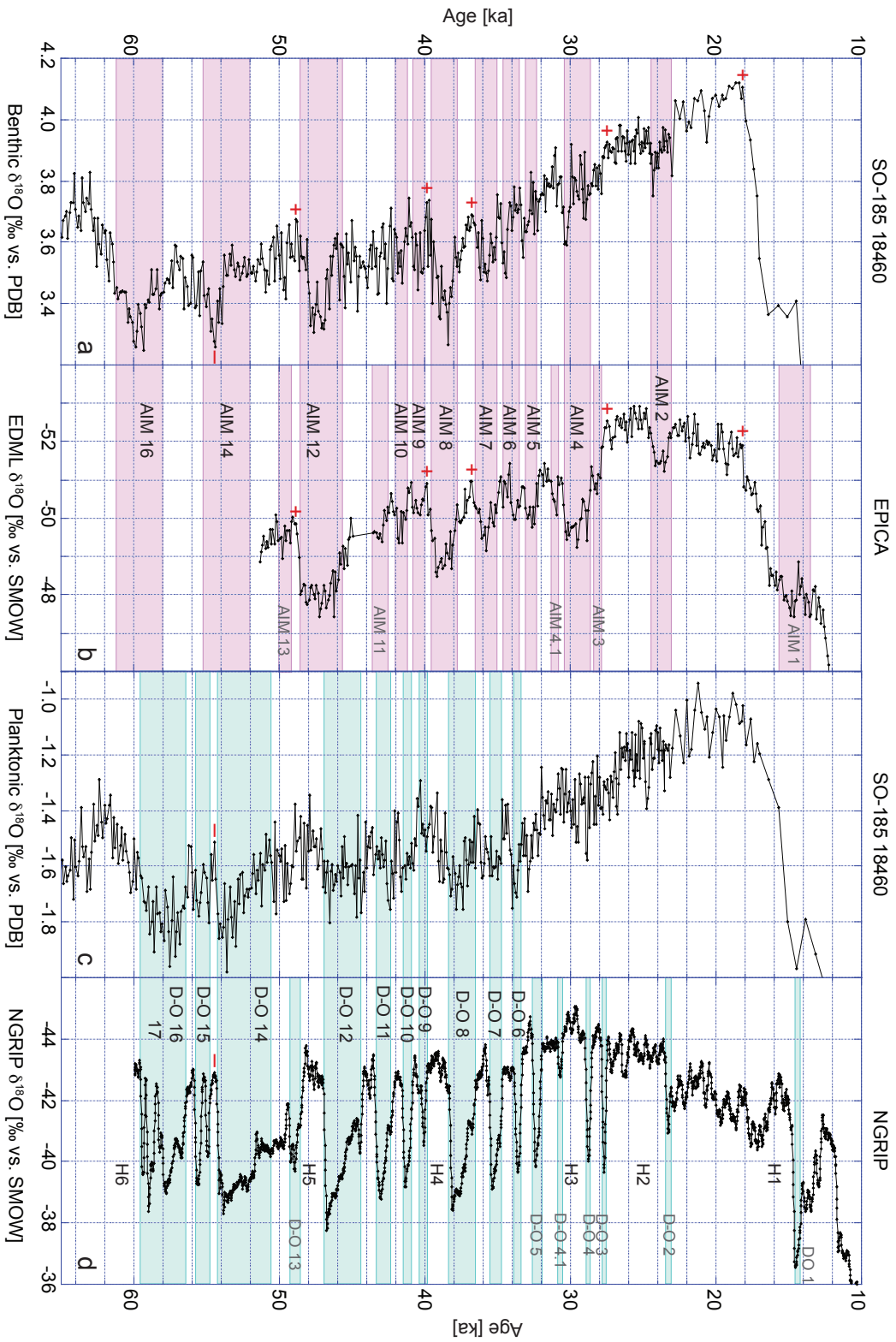


Figure 4.5 a) Benthic foraminiferal $\delta^{18}\text{O}$ (*P. wuellerstorfi*) in Core SO-185 18460 and b) $\delta^{18}\text{O}$ in EDML ice core versus age. Crosses indicate the points between both $\delta^{18}\text{O}$ records. Antarctic Isotope Maxima (AIM 1 – AIM 16) are indicated by shaded bars; c) and d) Comparison of SO-185 18460 planktonic foraminiferal $\delta^{18}\text{O}$ with Greenland ice core $\delta^{18}\text{O}$. Dashes indicate the point between both $\delta^{18}\text{O}$ records. D-O warm events (D-O 1 – D-O 17) are indicated by shaded bars. Nomenclature of EDMML and NGRIP warm events follows *EPICA Community Members (2006)*

the benthic oxygen isotope record (Figure 4.5). We correlate these events to AIM at ≈ 41.5 ka (AIM 10), ≈ 40.5 ka (AIM 9), ≈ 36 ka (AIM 7), ≈ 34 ka (AIM 6), ≈ 33 ka (AIM 5), ≈ 30 ka (AIM 4) and ≈ 24 ka (AIM 2). The benthic $\delta^{13}\text{C}$ record (Figure 4.6) used as indicator for bottom water ventilation exhibits an overall range between -0.3‰ and $\approx 0.3\text{‰}$. $\delta^{13}\text{C}$ values show an increase by progressive stages between ≈ 64 – 38 ka of $\approx 0.6\text{‰}$, reaching the maximum $\delta^{13}\text{C}$ value of $\approx 0.3\text{‰}$ at ≈ 39 ka. The younger part of the record (≈ 39 – 22 ka) shows a decreasing trend from $\approx 0.3\text{‰}$ to -0.2‰ .

Planktonic foraminiferal $\delta^{18}\text{O}$ values vary between $\approx -1.0\text{‰}$ and -2.0‰ over the entire record (Figures 4.5–4.6). Between 65–62 ka a first observed long-term trend is indicated by a continuous increase from -1.7‰ to -1.3‰ . Thereafter the $\delta^{18}\text{O}$ record exhibits three similar long-term cycles of variability within the time interval 61–31 ka. Each cycle is characterized by three to four minima with a period of one to three kyr. This sequence of high-frequency minima shows close affinity to fluctuation characteristics of northern high-latitude ice core records (Figure 4.6). We correlate these events clearly expressed by decreases of ≈ 0.4 – 0.5‰ to Northern Hemisphere D-O warm events (D-O 16, 17 centered at ≈ 58 ka, the double peak of D-O 15 at ≈ 55 ka, D-O 14 centered at ≈ 52 ka, D-O 12 centered at ≈ 46 ka, D-O 11 at ≈ 43 ka, D-O 10 at ≈ 41 ka, D-O 9 at ≈ 40 ka, D-O 8 centered at ≈ 37 ka, D-O 7 at ≈ 35 ka, and D-O 6 at ≈ 33.5 ka). Between ≈ 31 ka and ≈ 22 ka the $\delta^{18}\text{O}$ values increase and reach their maximum values during MIS 3 of about -1.1‰ at ≈ 25 ka. The planktonic $\delta^{13}\text{C}$ record shows four main trends and a maximum amplitude fluctuation of $\approx 0.7\text{‰}$ (Figure 4.6). After a slight decrease in $\delta^{13}\text{C}$ of about $\approx 0.3\text{‰}$ (65–60 ka) the record exhibits a continuous increase of about $\approx 0.5\text{‰}$ until ≈ 47 ka. Between ≈ 47 ka and ≈ 29 ka the record is characterized by values of $\approx 1.2\text{‰}$ to $\approx 1.5\text{‰}$, and the upper part reveals lower values of about $\approx 1.1\text{‰}$ and $\approx 1.3\text{‰}$.

To ease the comparison of both sites from the Timor Passage and Timor Sea Δ -values were calculated as described in the methods (section 4.3.1). Benthic $\Delta\delta^{18}\text{O}$ and $\Delta\delta^{13}\text{C}$ values vary between $\pm 0.25\text{‰}$ and -0.35 – -0.15‰ , respectively (Figure 4.7). Maximum fluctuations in both benthic $\Delta\delta$ records of about 0.3 – 0.5‰ occur at AIM 16, 14, 12 and 8. The planktonic $\Delta\delta^{18}\text{O}$ oxygen values vary between $\approx 0.25\text{‰}$ and -0.3‰ , whereas the planktonic $\Delta\delta^{13}\text{C}$ values vary between -0.45‰ and 0.1‰ . Focussing on Heinrich events there are slight changes between 0.2‰ and 0.4‰ in both planktonic Δ -isotope records to more negative values (Figure 4.7, indicated by arrows). In contrast to the benthic and planktonic Δ -isotope records the $\Delta\delta^{18}\text{O}_{sw}$ and ΔSST records exhibit three pronounced long-term trends (Figure 4.7, indicated by arrows). The first trend is a decrease in $\Delta\delta^{18}\text{O}_{sw}$ values of about 0.8‰ between ≈ 62 ka and ≈ 59 ka and an increase starting at ≈ 59 ka $\Delta\delta^{18}\text{O}_{sw}$ up to $\approx 0.4\text{‰}$ (at ≈ 55 ka). Between ≈ 55 ka and ≈ 44 ka the second trend is indicated by a decrease of about -0.9‰ in $\Delta\delta^{18}\text{O}_{sw}$ (≈ 55 ka– ≈ 49 ka), followed by an increase of about 0.9‰ with a maximum value (0.45‰) at ≈ 44 ka. This striking maximum is the starting point of the third $\Delta\delta^{18}\text{O}_{sw}$ trend with decreasing values up to -0.4‰ (≈ 39 ka) followed by successional fluctuations of about 0.5‰ between ≈ 39 ka and 26 ka.

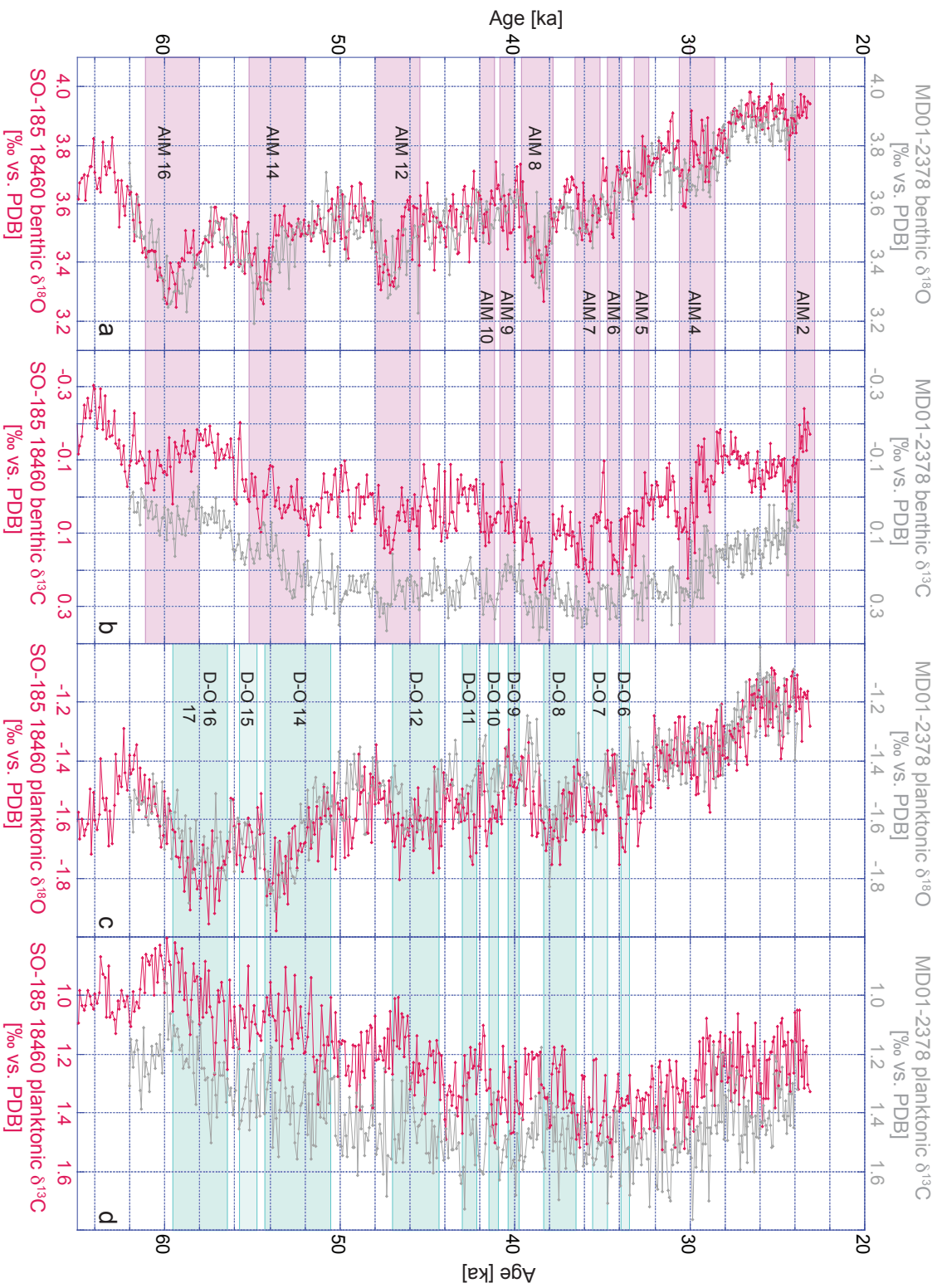


Figure 4.6 a) Benthic foraminiferal $\delta^{18}\text{O}$ and b) $\delta^{13}\text{C}$ (*P. wuellerstorfi*) of Cores SO-185 18460 (red) and MD01-2378 (grey); c) Planktonic foraminiferal $\delta^{18}\text{O}$ and d) $\delta^{13}\text{C}$ (*G. ruber*) in Cores SO-185 18460 (red) and MD01-2378 (grey). Shaded bars indicate correlated AIM (pink) and D-O warm events (green).

The $\Delta\delta^{18}\text{O}_{sw}$ and ΔSST records exhibit similar features (Figure 4.7). In particular, the ΔSST long-term trends are close to the $\Delta\delta^{18}\text{O}_{sw}$ record as described above. The ΔSST record covers a range of values of ≈ 6 K.

4.4.3 Benthic foraminiferal census counts

Accumulation rates of benthic foraminifera are used to estimate variations of past carbon-flux rates to the seafloor (Loubere, 1996; Herguera, 2000). In Core SO-185 18460 BFAR varies between ≈ 40 and ≈ 270 individuals $\text{cm}^{-2} \text{kyr}^{-1}$ over the studied time interval (Figure 4.8). Main increases in the number of specimens between ≈ 60 – 54 ka and ≈ 52 – 47 ka particularly coincide with marked rises in the AR of buliminids (Figure 4.8). Between ≈ 47 ka and ≈ 30 ka BFAR is characterized by lower values of ≈ 130 – 60 individuals $\text{cm}^{-2} \text{kyr}^{-1}$. BFAR values start to increase again at ≈ 30 ka reaching maximum values of ≈ 240 individuals $\text{cm}^{-2} \text{kyr}^{-1}$ at ≈ 28 ka. After ≈ 28 ka BFAR values vary between ≈ 200 – 100 individuals $\text{cm}^{-2} \text{kyr}^{-1}$.

Accumulation rates of buliminids show a positive correlation to the benthic $\delta^{18}\text{O}$ record (Figure 4.8) and vary between ≈ 5 and ≈ 55 individuals $\text{cm}^{-2} \text{kyr}^{-1}$. Our record reflects buliminid abundances of ≈ 8 – 16 individuals $\text{cm}^{-2} \text{kyr}^{-1}$ between ≈ 62.5 ka and ≈ 59.5 ka. Then buliminid AR values are increasing until ≈ 57 ka reaching a maximum value of ≈ 35 individuals $\text{cm}^{-2} \text{kyr}^{-1}$. Decreasing values (until ≈ 54 ka) are followed by a stepwise increase of buliminid abundance finally reaching the maximum of ≈ 55 individuals $\text{cm}^{-2} \text{kyr}^{-1}$ at ≈ 49 ka. The accumulation rate of buliminids is then characterized by rapid decreases reaching low values at ≈ 47 ka (≈ 7 individuals $\text{cm}^{-2} \text{kyr}^{-1}$). During the following time interval (≈ 46.5 ka– 39.5 ka) values vary between ≈ 16 – 28 individuals $\text{cm}^{-2} \text{kyr}^{-1}$. Starting at ≈ 39 ka the low abundance of buliminid is reflected by ≈ 5 individuals $\text{cm}^{-2} \text{kyr}^{-1}$ until ≈ 34 ka. In the end of MIS 3 accumulation rates of buliminid show again a continuous increase reaching values of about ≈ 45 individuals $\text{cm}^{-2} \text{kyr}^{-1}$.

Globocassidulinids are represented by low variations of accumulation rates during the studied time interval. Values vary between ≈ 0 – 8 individuals $\text{cm}^{-2} \text{kyr}^{-1}$.

4.5 Discussion

To elucidate the climate history of the Eastern Indian Ocean during MIS 3 and to distinguish between high-latitude and regional climate signals as well as monsoonal activity and oceanographic reorganization the presented stable isotope records and faunal census counts (Section 4.4) of Core SO-185 18460 are discussed in conjunction with those of Core MD01-2378 studied by Dürkop *et al.* (2008, see Chapter 2). Additionally BFAR records of both cores will be discussed to assess regional differences in foraminiferal abundances and to deduce their possible reasons.

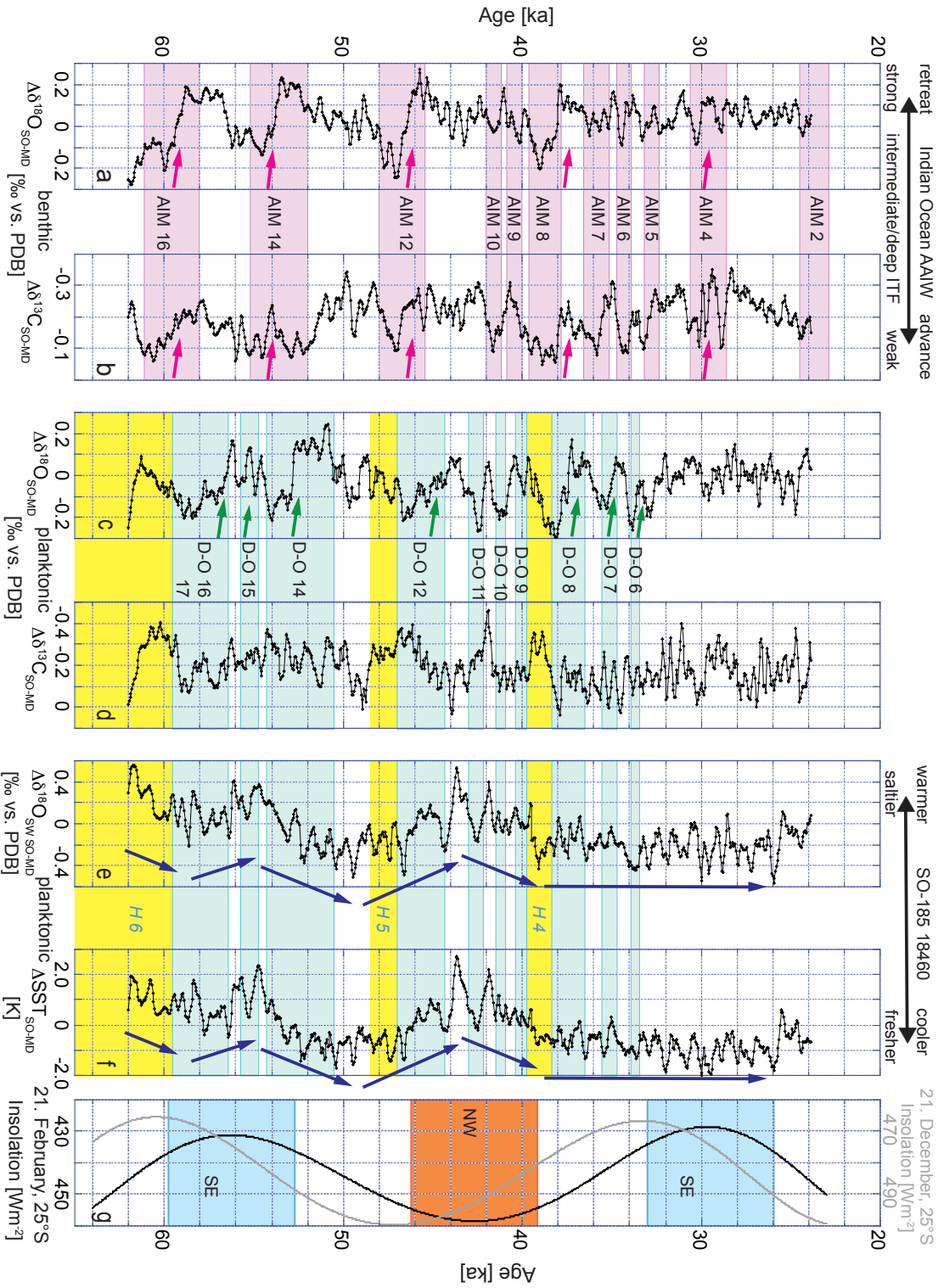


Figure 4.7 a) Benthic foraminiferal $\Delta\delta^{18}\text{O}$ and b) $\Delta\delta^{13}\text{C}$ (*P. wuellerstorfi*); c) Planktonic foraminiferal $\Delta\delta^{18}\text{O}$ and d) $\Delta\delta^{13}\text{C}$ (*G. ruber*); e) planktonic $\Delta\delta^{18}\text{O}_{\text{sw}}$; f) ΔSST and g) Insolation at 25°S. All Δ -values are calculated as SO minus MD. Shaded bars indicate: AIM (pink); D-O (green), Heinrich events (yellow). Arrows indicate: millennial (pink and green) and (semi-) precessional (blue) trends.

A striking feature of both high-resolution MIS 3 cores from the Timor Sea and the Timor Passage is the contrast between the benthic oxygen isotope signal varying with Southern Hemisphere high-latitude climate signature and the planktonic $\delta^{18}\text{O}$ isotopes showing close affinity to Northern Hemisphere high-latitude climate. In detail, benthic $\delta^{18}\text{O}$ values of Core SO-185 18460 covary with the Antarctic temperature signals, whereas the planktonic $\delta^{18}\text{O}$ values covary with Greenland temperature variations. This anti-phase relationship has been detected before in ice core records (*Dansgaard et al.*, 1993; *Grootes et al.*, 1993; *Blunier et al.*, 1998; *EPICA Community Members*, 2006) and several marine sediment records (*Shackleton et al.*, 2000; *Pahnke and Zahn*, 2005; *Martrat et al.*, 2007; *Dürkop et al.*, 2008; *Mulitza et al.*, 2008; *Jung et al.*, 2009). *Broecker* (1998) interpreted this phasing as a bipolar climate seesaw.

4.5.1 Southern Hemisphere climate signals and regional differences in benthic oxygen and carbon isotope records from the Eastern Indian Ocean

Benthic $\delta^{18}\text{O}$ records of both Cores SO-185 18460 and MD01-2378 show approximately the same distribution of minimum and maximum values within a range of 3.2‰ and 4.0‰. Especially the four prominent oxygen isotope minima at ≈ 60 ka, ≈ 54 ka, ≈ 47 ka, and ≈ 39 ka representing the main Antarctic warm events AIM 16, 14, 12 and 8 are clearly expressed in both benthic $\delta^{18}\text{O}$ records (Figure 4.6). As reviewed by *Siddall et al.* (2008) there is an ongoing debate about ice volume effect, its origin and the timing of sea level changes during MIS 3. These authors concluded that sea level stands were of about -60 m for the first and -80 m for the second half of MIS 3. Due to insufficiently observed data and the scarcity of model studies the mechanisms of sea level fluctuations during MIS 3 are poorly understood. *Shackleton et al.* (2000) interpreted half of the major benthic $\delta^{18}\text{O}$ excursions to lower values in their Iberian Margin records as Antarctic temperature signal due to unlikely rapid mixings of ice volume signals through the ocean.

However, *Dürkop et al.* (2008, see Chapter 2) suggested the transmission of the Southern Hemisphere signal to site MD01-2378 through the transfer of Antarctic Intermediate Water (AAIW) from the Antarctic Circumpolar Current towards the Timor Sea lasting ≈ 300 yr (*Matsumoto and Key*, 2004). Due to the strength and timing of the Southern Hemisphere signal detected in the benthic oxygen isotopes of Core SO-185 18460 we suggest that the same transport media and mechanism are applicable to this site. The benthic oxygen isotope records of Core SO-185 18460 located within the Timor Passage and of Core MD01-2378 located further south in the Timor Sea (Figures 4.1 and 4.6) display different shapes during the second half of the main AIM (at $\approx 59-58$ ka, $\approx 54-53$ ka, $\approx 46.5-45$ ka and $\approx 37-36$ ka). Therefore the shape of an AIM in the $\delta^{18}\text{O}$ record of Core MD01-2378 exhibits a gradual decrease and increase of $\delta^{18}\text{O}$ values as previously known from Antarctic ice core studies (*Johnsen et al.*, 1972; *Jouzel et al.*, 1987; *Blunier et al.*, 1998; *Blunier and Brook*, 2001; *EPICA Community Members*, 2004), whereas the shape of an AIM in the $\delta^{18}\text{O}$ record of Core SO-185 18460 shows a gradual decrease followed by an abrupt shift to higher $\delta^{18}\text{O}$ values.

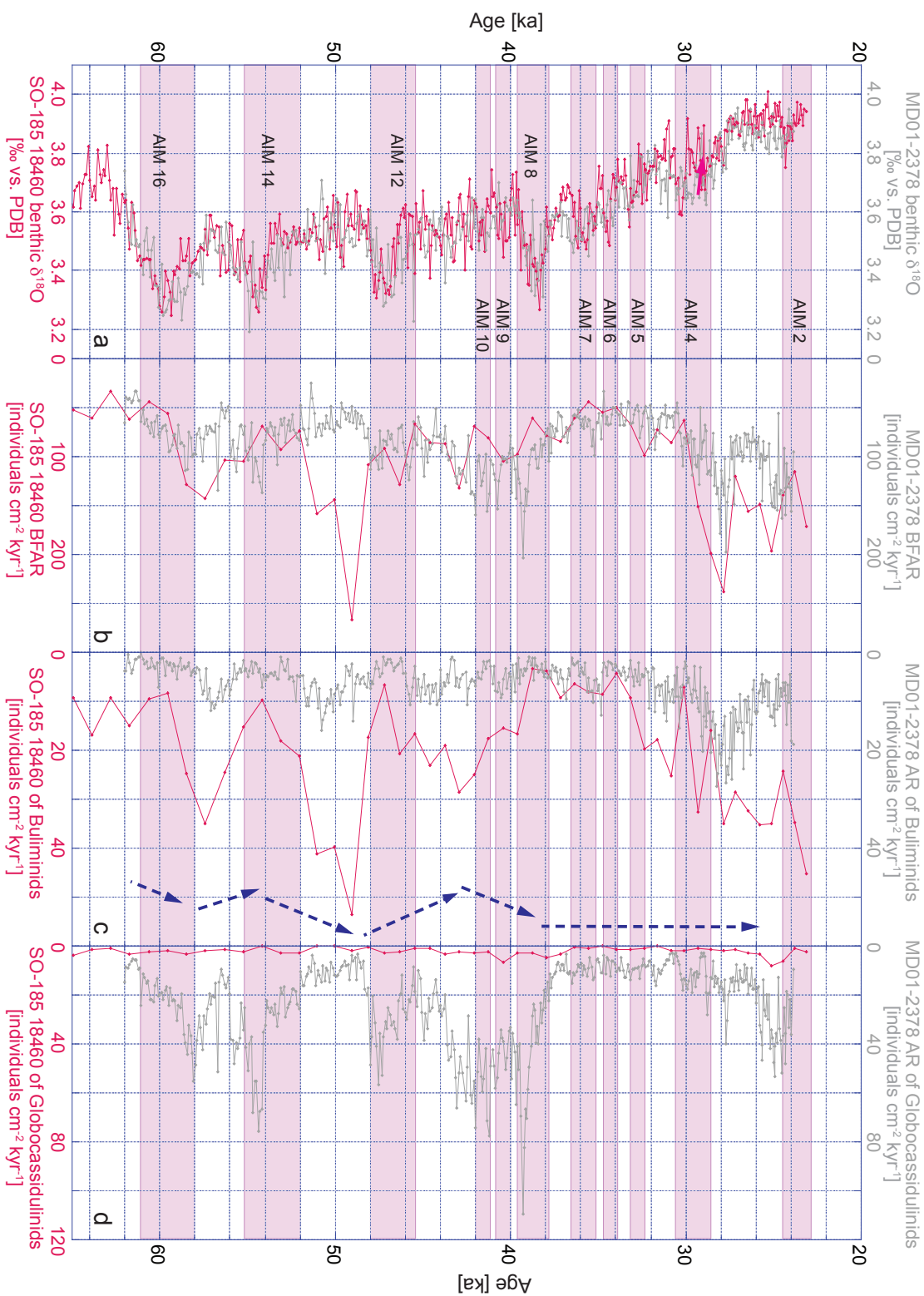


Figure 4.8 a) Benthic foraminiferal $\delta^{18}\text{O}$ and b) benthic foraminiferal accumulation rates (BFAR); c) accumulation rates (AR) of buliminids; and d) accumulation rates (AR) of globocassidulinids in Cores SO-185 18460 (red) and MD01-2378 (grey). Shaded bars indicate AIM. Arrows indicate (semi-) precessional (blue) trends, see Figure 4.7.

These abruptly muted benthic oxygen isotope signals in the $\delta^{18}\text{O}$ record of Core SO-185 18460 during the second half of the main AIM compared to Core MD01-2378 are much easier distinguishable in the benthic $\Delta\delta^{18}\text{O}$ record as indicated by arrows in Figure 4.7. However, these signals reflect regional oceanographic differences during the cooling phases of the pronounced AIM with a retreat of southern sourced deep water (AAIW) in the Timor Passage (SO-185 18460), and a more or less persistent AAIW ventilation in the Timor Sea (MD01-2378).

Between $\approx 42\text{--}40$ ka and $\approx 38\text{--}29$ ka Core SO-185 18460 exhibits higher variability in the benthic $\delta^{18}\text{O}$ record compared to Core MD01-2378, and reveals a more detailed structure with seven smaller excursions to lower $\delta^{18}\text{O}$ values as described in the results, which we relate to the Antarctic warm events AIM 10, 9, 7–4 and 2. These determined events are shorter in duration and smaller in amplitude than the detected prominent AIM 16, 14, 12 and 8. Both benthic $\delta^{18}\text{O}$ records show increasing trends starting at the minimum of AIM 8 (≈ 38 ka) until ≈ 25 ka. While Core MD01-2378 probably documents the steady influence of AAIW ventilation due to its southerly position, Core SO-185 18460 records abrupt retreats of AAIW at a key position within the Timor Passage, and hence within the global THC.

This hypothesis of forward and backward pushing AAIW at site SO-185 18460 is supported by its benthic carbon isotope record (Figure 4.6) and the benthic $\Delta\delta^{13}\text{C}$ record. In general both benthic $\delta^{13}\text{C}$ records of the cores from the Timor Sea and Timor Passage follow the MIS 3 trend as observed in *P. wuellerstorfi* and *Cibicidoides* spp. intermediate and deep-water mass records from the Iberian Margin (see [Shackleton et al., 2000](#)), the Southern Atlantic Ocean (see [Hodell et al., 2003](#)), and the Southwest Pacific (see [Pahnke and Zahn, 2005](#)). $\delta^{13}\text{C}$ values in Core SO-185 18460 are lower than those of Core MD01-2378, which may be due to local mixing with IOW masses, the deeper part of the ITF ([Talley and Sprintall, 2005](#)). Compared to the $\delta^{13}\text{C}$ record of Core MD01-2378 the range of values at site SO-185 18460 ($\approx 0.6\text{‰}$) is greater by $\approx 0.2\text{‰}$. During AIM benthic $\delta^{13}\text{C}$ data of Core SO-185 18460 reach positive values and move closer toward MD01-2378 $\delta^{13}\text{C}$ values. Decreasing benthic $\Delta\delta^{13}\text{C}$ values concurrently occur with increasing $\Delta\delta^{18}\text{O}$ values as indicated by arrows in Figure 4.7. These shifts in the benthic $\Delta\delta^{18}\text{O}$ and $\Delta\delta^{13}\text{C}$ records illustrate regional differences in Eastern Indian Ocean paleoceanography and indicate strong impacts of the southern sourced AAIW within the Timor Passage during times of weaker THC with an enhanced Southern Ocean circulation ([Schmittner et al., 2007](#)). After AIM 8 (at ≈ 38 ka) this process may be more intense with higher frequencies due to the ongoing deceleration of the THC related to the MIS 3–LGM transition.

4.5.2 Northern Hemisphere climate signals, monsoon activity, and regional differences in planktonic oxygen and carbon isotope values from the Eastern Indian Ocean

A tight coupling between North Atlantic temperatures and the Asian monsoon activity was documented by analysis of (sub-) tropical stalagmites ([Wang et al., 2001](#); [Burns et al., 2003](#)) and ice core dust parameters ([Ruth et al., 2007](#)). These studies support the idea of far-reaching

Northern Hemisphere atmospheric circulation patterns on millennial to centennial timescales. *Ruth et al.* (2007) proposed synchronous changes (within 5–10 years) in North Atlantic and Asian climate due to persistent atmospheric processes. They also provided evidence for the relation of Northern Atlantic temperatures and Asian monsoon intensity during interstadials (D-O events). Therefore increasing temperatures instantaneously strengthened Asian summer and weakened Asian winter monsoon. At the same time the atmospheric circulation patterns in the Northern Hemisphere are supposed to have been more meridional than zonal in character (*Wang et al.*, 2001). Further evidence for the rapid atmosphere-ocean interaction system between high- and low-latitudes on millennial to centennial timescales is indicated by several stalagmite studies, reflecting transports of heat and moisture across the equator and from low- to high-latitudes (*Schulz et al.*, 1998; *Wang et al.*, 2001).

Comparing planktonic $\delta^{18}\text{O}$ records of Cores SO-185 18460 and MD01-2378 similarities in decreasing and increasing trends are evident and millennial timescale fluctuations to lower $\delta^{18}\text{O}$ values are related to Northern Hemisphere D-O events (Figures 4.5–4.6). These warm events are supposed to have been transmitted through atmospheric teleconnections from high- to low-latitudes (*Dürkop et al.*, 2008, see Chapter 2). With respect to Core MD01-2378 the planktonic oxygen isotope record of Core SO-185 18460 exhibits much more high-frequency variations and covers a larger range of values with rather negative $\delta^{18}\text{O}$ values (Figure 4.6). Planktonic $\Delta\delta^{18}\text{O}$ and $\Delta\delta^{13}\text{C}$ records clearly reflect fluctuations on millennial timescales, whereas the $\Delta\delta^{18}\text{O}_{sw}$ and ΔSST primarily reflect fluctuations on (semi-) precessional timescales and covary with the austral summer insolation at 25°S (Figure 4.7). Thereby positive ΔSST and $\Delta\delta^{18}\text{O}_{sw}$ indicate higher SST and $\delta^{18}\text{O}_{sw}$ values at site SO-185 18460 compared to site MD01-2378. As the East Asian-Australian monsoon is an insolation dependent system one can relate the long-term fluctuations in the ΔSST and $\Delta\delta^{18}\text{O}_{sw}$ records to the different monsoon phases.

However, higher SST and $\delta^{18}\text{O}_{sw}$ values at site SO-185 18460 are correlated to a SE- (62–53 ka) and a NW- (46–39 ka) monsoon phase of the East Asian-Australian monsoon system on precessional timescale (Figure 4.7). In contrast lower SST and $\delta^{18}\text{O}_{sw}$ values at site SO-185 18460 are related to the transition phase (53–46 ka) and a less intense SE-monsoon phase (39–22 ka) of the East Asian-Australian monsoon system.

1st SE-monsoon phase (62–53 ka)

Today the surface-temperature gradient between both sites is relatively constant throughout the year with a maximum of about ≈ 1.0 K during July-September, whereas the surface salinities at both sites show the same values (≈ 34.2 – 34.3) for this period (Figure 4.2). Averaged ΔSST -values of ≈ 1 K indicate that these modern SE-monsoon conditions may be applicable to the SE-monsoon phase between 62–53 ka. Due to the close vicinity of both cores a difference in ΔSST -records as a result of ice volume effects can be neglected. As the SE-monsoonal winds are very dry compared to NW-monsoonal winds (*van der Kaars et al.*, 2000) slightly higher $\Delta\delta^{18}\text{O}_{sw}$ values may be a result of regional differences in evaporation with drier conditions at site SO-185 18460.

NW-monsoon phase (46–39 ka)

Regarding modern in-situ data (NODC, 2001) highest SST and relative high salinity values could be expected for NW-monsoonal conditions at both sites (Figure 4.2). Contrary to modern conditions the $\delta^{18}\text{O}_{sw}$ and SST values were higher at site SO-185 18460 (up to 0.5‰ and ≈ 2 K) with respect to site MD01-2378 during the NW-monsoon phase (46–39 ka). As shown by van der Kaars *et al.* (2000) and Tapper (2002) regional climate settings in the Timor Sea and Indonesian Archipelago are of high complexity. This is expressed by strong seasonal contrasts in precipitation patterns, which are related to the monsoonal influence. Taking these complex precipitation patterns into account and assuming a most southerly shift of the ITCZ during NW-monsoon phases, it may be possible that the position of Core SO-185 18460 experienced very warm and dry conditions with intense evaporation compared to Core MD01-2378 (Figure 4.2).

In contrast Core MD01-2378 seemed to have been influenced by fresher and cooler surface water during this time interval. As known from previous studies by Holbourn *et al.* (2005) and Dürkop *et al.* (2008, see Chapter 2) site MD01-2378 was affected by a hydrological front between the WAC and LC on different timescales. These authors mentioned a probable link between the occurrence of this hydrological front and monsoonal activity. Furthermore observations show a relation between the NW-monsoon and the activity of tropical cyclones (hurricanes) (see Suppiah, 1992, and references therein). These cyclones are formed between 10–20°S in the Eastern Indian Ocean. They move eastward and their activity is confined to austral summer months (NW-monsoon phase). During this time the heat lows over Pilbara and Cloncurry regions (deserts) are developed with maximum heating. Hence the monsoon circulation increases and results in heavy rainfall. However, fresher and cooler surface water was possibly advected to site MD01-2378 by a northeastward moving hydrological front or/ and related to tropical cyclone activity with increased precipitation and stronger vertical mixing during this NW-monsoon phase.

2nd SE-monsoon phase (33–26 ka)

In comparison to the first SE-monsoon phase, which is reflected by higher $\Delta\delta^{18}\text{O}_{sw}$ and ΔSST values the second SE-monsoon phase (33–26 ka) is less pronounced. It is characterized by negative ΔSST ($\approx -1\text{K}$) and $\Delta\delta^{18}\text{O}_{sw}$ (-0.2‰) values. These values reflect cooler and fresher surface water conditions at the position of Core SO-185 18460 compared to Core MD01-2378. As represented by the planktonic $\delta^{18}\text{O}$ records in Figure 4.6 a cooling trend started at ≈ 38 ka. With respect to site MD01-2378 the SST at site SO-185 18460 started a decreasing trend at ≈ 40 ka and reached minimum values of about 24°C at ≈ 30 ka (Zuraida, unpublished data). In accordance to this cooling planktonic $\delta^{13}\text{C}$ records of both cores converge and move to lower $\delta^{13}\text{C}$ values.

This second SE-monsoon phase between 33–26 ka may be comparable with times of stadial conditions due to the simultaneous MIS3–LGM transition. During stadials the ITCZ is supposed to have moved southward (Clark *et al.*, 2007). Characteristics of circulation patterns changed then from meridional to more zonal patterns with stronger westerlies (Jin *et al.*, 2007). This increased zonal atmospheric circulation led to a general weaker monsoon activity (Wang *et al.*,

2001) during these times. *Oppo and Sun (2005)* detected a connection between the East Asian summer monsoon and the inflow of cold surface water from the Pacific into the northern South China Sea. A decrease in East Asian summer monsoon strengthened the inflow of cold surface water. Suggesting general cooler background and weaker boreal summer monsoon conditions during this second SE-monsoon phase due to the described long-term cooling trend (Figure 4.6) a stronger inflow of cold Pacific surface water into the Indonesian Archipelago could be expected. This may explain the much colder SST and less saline conditions at the position of Core SO-185 18460. Another explanation for fresh water advection to this site would be provided by the study of *Atmadipoera et al. (2009)*. These authors observed a surface fresh water lense with its origin in the Java Sea during the monsoonal transition time from NW- to SE-monsoonal conditions. This fresh water lense is a result of excess precipitation and river run-off. It is supposed to move southward, to reach the outflow regions of the Indonesian Archipelago with a phase lag and to last there for several months. It may be plausible that a precipitation dependent fresh water lense existed during monsoonal transition phases on precessional timescales and led to cooling and less saline conditions at the position of Core SO-185 18460.

Millennial-timescale variability

Focussing on millennial timescale variability a clear pattern is not obvious in Δ SST and $\Delta\delta^{18}\text{O}_{sw}$ records due to the predominant precessional long-term trend, whereas the planktonic $\Delta\delta^{18}\text{O}$ record reflects distinct fluctuations during D-O events (Figure 4.7). Compared to site MD01-2378 lower $\delta^{18}\text{O}$ values are reflected by the SO-185 18460 record (Figure 4.6). When the Northern Hemisphere experienced warming site SO-185 18460 underwent a decrease in SST and in $\delta^{18}\text{O}_{sw}$ compared to site MD01-2378 as indicated by *Zuraida* (unpublished data). This difference between both sites is reflected as an increase in planktonic $\Delta\delta^{18}\text{O}$ values (Figure 4.7). During D-O events the ITCZ should have been in a more northerly position compared to Heinrich events (*Clark et al., 2007*). Additionally the intensity of the Northern Hemisphere summer monsoon was supposed to increase during D-O events (*Ruth et al., 2007*). This would have had repercussions on the Australian monsoon system too (*Hung et al., 2004; Miller et al., 2005*). Increased precipitation could have then produced the Java Sea fresh water lense, which may have moved southward as observed by *Atmadipoera et al. (2009)* for modern conditions. During stadials this advection may have been reasonable for lower saline and cooler surface conditions at the position of Core SO-185 18460 compared to Core MD01-2378.

4.5.3 Regional differences in benthic foraminiferal abundances in the Eastern Indian Ocean

Benthic foraminiferal abundances are dependent on the supply of organic carbon, which is delivered to the seafloor and reflects the exported productivity of the photic zone (*Herguera and Berger, 1991; Herguera, 2000*). Therefore the distribution of benthic foraminifera is largely controlled by the amount of food that reaches the seafloor (*Lutze and Coulbourn, 1984; Altenbach*

and Sarnthein, 1989; Herguera and Berger, 1991). As shown by Holbourn *et al.* (2005) and Dürkop *et al.* (2008) (see Chapter 2) increases in foraminiferal abundances are related to paleoproductivity increases induced by monsoon activity in the Timor Sea.

BFAR records of Cores SO-185 18460 and MD01-2378 are similar in absolute values and reveal the same trends of foraminiferal abundances except for the episode $\approx 52\text{--}48$ ka (Figure 4.8). During this time interval BFAR of Core SO-185 18460 reach maximum values whereas Core MD01-2378 exhibits lowest values. We attribute this difference to highest AR of buliminids, which may be representative of the endobenthic foraminiferal species. Furthermore both BFAR records deviate by ≈ 75 individuals $\text{cm}^{-2} \text{kyr}^{-1}$ between AIM 16 and 14 with higher foraminiferal abundance in Core SO-185 18460 and lower foraminiferal abundance in Core MD01-2378. We also relate this episode of BFAR rise to an endobenthic fauna increase in Core SO-185 18460 represented by a higher buliminid AR (Figure 4.8). Starting at ≈ 30 ka both records show marked increases with deviations up to ≈ 130 individuals $\text{cm}^{-2} \text{kyr}^{-1}$, which we attribute to the MIS 3–LGM transition, when higher surface ocean primary productivity is suggested (McCorkle *et al.*, 1999).

However, globocassidulinids, which are supposed to prefer low carbon-flux rates, high dissolved-oxygen concentrations (Murgese and De Deckker, 2007) and selectively favor diatoms as food (Suhr *et al.*, 2003), show AR of about maximum 10 individuals $\text{cm}^{-2} \text{kyr}^{-1}$ in Core SO-185-18460 and $\approx 10\text{--}110$ individuals $\text{cm}^{-2} \text{kyr}^{-1}$ in Core MD01-2378 (Figure 4.8). Very low AR of globocassidulinids in Core SO-185 18460 indicate a missing food source in the Timor Passage. In contrast the intense excursions of globocassidulinids AR in Core MD01-2378 are related to changes in the food source, which may be linked to the oceanic reorganization of the Southern Ocean accompanied by the migration of a hydrological front (Dürkop *et al.*, 2008; Zuraida *et al.*, 2009, see Chapters 2 and 3). We suggest that the migration followed a (semi-) precessional cycle as indicated in Figure 4.8 (blue dashed arrows in Figure 4.7).

Recent studies from the Eastern Indian Ocean have shown that changes in AR of buliminids may be linked to monsoon variability (Holbourn *et al.*, 2005; Dürkop *et al.*, 2008, see Chapter 2) or variations within the mixed layer and to reduced bottom water circulation Murgese *et al.* (2008). Generally low buliminid AR at both sites are representative for oligotrophic conditions where metabolized organic matter is mainly restricted to the sediment surface (Jorissen *et al.*, 1995). Buliminids occur in areas with high levels and continuous flux of organic matter to the seafloor (Lutze and Coulbourn, 1984). Their abundance increases with higher surface ocean primary productivity (McCorkle *et al.*, 1999) and/ or by reduced seafloor oxygenation (Murgese and De Deckker, 2007). A comparison of buliminid counts of the Timor Sea and Timor Passage reflects higher abundance at site SO-185 18460 (Figure 4.8). At this site buliminids maybe require less oligotrophic conditions with higher food supply and reduced oxygen levels compared to Core MD01-2378. This may indicate a change in the endobenthic foraminiferal abundance related to variations in paleoproductivity and bottom water ventilation within the Eastern Indian Ocean (Figure 4.8). Both AR records covary with stadial (increase) and interstadial (decrease) conditions during MIS 3. As buliminid AR are higher in Core SO-185 18460 the idea of regional differences

in bottom water ventilation as already described above for the benthic isotope records (Section 4.5.1) is supported. During stadials when buliminids showed highest abundances the Southern Ocean circulation with higher oxygen concentrations was probably enhanced in the Indo-Pacific (Schmittner *et al.*, 2007). While site MD01-2378 is suggested to be more steadily ventilated by AAIW as reflected by slight stadial AR excursions buliminid abundances strongly increase with possibly lower oxygen concentration at site SO-185 18460 (Figure 4.8) as soon as the AAIW started to retreat further to the south. Similar to the planktonic isotope data (Section 4.5.2) tropical cyclones were probably active close to the position of Core MD01-2378. Dürkop *et al.* (2008, see Chapter 2) suggested that these cyclones have induced strong vertical mixing of the upper water column during stadials, when the ITCZ moved most southerly. As a result this vertical mixing led to increases in primary production at site MD01-2378 during these time intervals.

Productivity changes on (semi-) precessional timescales at site SO-185 18460 are not clearly evident for MIS 3 as indicated by the blue dashed arrows in Figure 4.8. Increases in primary productivity are expected during SE-monsoon conditions, when winds would lead to upwelling in the Indonesian Archipelago (Gordon, 2005). Consequently, lower abundances of buliminids would be expected at site SO-185 18460 during the NW-monsoon phase, when southeastward directed winds would lead to downwelling condition. An increased stratification of the water column at site SO-185 18460 may be indicated by SST and $\delta^{18}\text{O}_{sw}$ records from Zuraida (unpublished data) compared to Core MD01-2378. As AR of buliminid of Core SO-185 18460 show higher abundances during the NW-monsoon phase, the bottom water circulation is supposed to be mainly responsible for changes in AR of buliminids.

4.6 Conclusions

Comparison of Cores SO-185 18460 and MD01-2378 provides essential insights in regional climate conditions and paleoceanography in the Eastern Indian Ocean in relation to global changes during MIS 3. High-resolution benthic oxygen and carbon isotope records of Core SO-185 18460 are correlated with Antarctic warm events (AIM). These signals are supposed to be transmitted by a northward pushing intermediate and deep water mass (AAIW) during times of weaker THC. The benthic isotope data and Δ -records indicate forward and backward pushing AAIW with abrupt retreats at site SO-185 18460 during times of THC acceleration.

In contrast planktonic oxygen isotope records detect Northern Hemisphere D-O events at both sites, which are probably transmitted from high- to low-latitudes through the East Asian-Australian monsoon system. A comparison of our proxy data with modern SST and salinity conditions at both sites reflects monsoon related climate variability in the Eastern Indian Ocean linked to a moving ITCZ on (semi-) precessional timescales. It is evident that the more northerly located site SO-185 18460 underwent higher variability in SST and $\delta^{18}\text{O}_{sw}$ than site MD01-2378 on (semi-) precessional and millennial timescales. Comparison of the planktonic proxy-data of both cores shows higher monsoon related climate variability at the position of Core SO-185 18460. This site was probably affected by intense evaporation during the first (semi-) precessional SE-

monsoon phase (62–53 ka). While Core SO-185 18460 experienced dry conditions during the NW-monsoon phase (46–39 ka), Core MD01-2378 reflects fresher and cooler conditions at the surface due to the migration of a hydrological front and increased vertical mixing induced by tropical cyclones. In contrast the position of Core SO-185 18460 underwent cooler and fresher surface water conditions during the second (semi-) precessional SE-monsoon phase (33–26 ka). Apparently fresh surface water was probably advected to site SO-185 18460 by an increased inflow of cool Pacific surface water into the Indonesian Archipelago or by a southeastward moving fresh water lense with its origin in the Java Sea.

Additionally benthic foraminiferal AR support the idea of regional differences in paleoceanographic settings in the Eastern Indian Ocean. AR of globocassidulinids may indicate a contrast in food sources between site MD01-2378 and SO-185 18460 on (semi-) precessional timescales. Therefore the apparent activity of a hydrological front at site MD01-2378 is reflected by increases in AR of globocassidulinids during the NW-monsoon phase (46–39 ka). In contrast AR of buliminids show variations on millennial timescales. Changes with stadials and interstadials had a stronger impact on site SO-185 18460 compared to site MD01-2378. Variations in bottom water ventilation as indicated by the benthic isotope data are supposed to be related with these changes.

4.7 Acknowledgment

We gratefully acknowledge the Deutsche Forschungsgemeinschaft (DFG) for funding this research (grant Ku 649/25-1) and the German Ministry for Education, Science and Technology (BMBF Grant 03GO185B) for funding the SONNE-185 cruise.

Chapter 5

Summary

High-resolution multi-proxy records from marine sediment cores from the Eastern Indian Ocean (Timor Sea) were analyzed to investigate the role of the tropics within the global climate system and to gain insights into the regional paleoceanography and climate settings during Marine Isotope Stage 3 (MIS 3). The Indonesian Throughflow (ITF) is a key component within the global thermohaline circulation (THC) transporting low-saline tropical waters from the western Pacific through the Indonesian Archipelago into the eastern Indian Ocean feeding the South Equatorial Current and the Leeuwin Current (*Tomczak and Godfrey, 2003; Talley and Sprintall, 2005*). Today this climate sensitive area is influenced by the biannual migration of the Intertropical Convergence Zone (ITCZ) and the related Asian-Australian monsoon system (*van der Kaars et al., 2000*), which leads to strong differences in regional precipitation patterns over the Indonesian Archipelago (*Tapper, 2002*) and induces formations of tropical cyclones between 10° S and 20° S (*Suppiah, 1992*). Thus, Core MD01-2378 in the outflow and Core SO-185 18460 in the mainflow area of the ITF are ideally situated to monitor linkages between tropical and high-latitude climate at this key position within the THC and the Asian-Australian monsoon system and to evaluate the regional paleoceanography and climate settings.

- This study of the marine sediment Cores MD01-2378 and SO-185 18460 monitored linkages between high- and low-latitude climate variability.
- Northern and Southern Hemisphere climate signals on millennial timescales have been detected in the tropical eastern Indian Ocean.
- A comparison of multi-proxy records of sites MD01-2378 and SO-185 18460 gave insights in regional paleoceanography and climate settings in the eastern Indian Ocean with probably high responses on changes in the Asian-Australian monsoon system during MIS 3.

5.1 High-resolution age model for Marine Isotope Stage 3

A quantitative comparison of high-resolution records from the tropics with those from high latitudes is dependent on an adequate age model. Therefore high-resolution benthic oxygen

isotope data of Cores MD01-2378 and SO-185 18460 were correlated to oxygen isotope data of the Antarctic EDML ice core for the time interval between 15 to 49 ka. The lower part is based on the correlation of one tie point between the planktonic oxygen isotope record with the oxygen isotope record of the Greenland NGRIP ice core and on linear extrapolation. The ice core data are synchronized to the layer counted NGRIP ice core following the Greenland Ice Core Chronology (GICC05) timescale (*EPICA Community Members, 2006; Andersen et al., 2006; Svensson et al., 2008*).

During MIS 3 the earth magnetic field showed several episodes of weakness leading to increased production of cosmogenic isotopes and resulting in the occurrence of ^{14}C -inversions, such as the Laschamp Event at around 41 ka (*Voelker et al., 2000; Hughen et al., 2004*). Hence, most of the conditions for constant marine reservoir ages do not hold (*Grootes and Sarnthein, 2006; Sarnthein et al., 2007*), and the calibration of AMS ^{14}C dates for MIS 3 is not straightforward. Despite these uncertainties we used AMS ^{14}C based calculated calendar ages with application of simulated glacial surface water reservoir ages to constrain our age models.

5.2 High-latitude climate signals in the tropics

The benthic oxygen isotope records of *P. wuellerstorfi* from Cores MD01-2378 and SO-185 18460 exhibit a high-latitude Southern Hemisphere signal covarying with Antarctic temperature increases and decreases during MIS 3. This signal is supposed to be transported through the Southern Ocean into the Timor Sea via the Antarctic Intermediate Water (AAIW). The ventilation of this water mass, also indicated by the benthic carbon isotope records, the $\Delta\delta^{18}\text{O}$ and $\Delta\delta^{13}\text{C}$, is dependent on the THC intensity with advances of AAIW during times of increased Southern Ocean circulation and Northern Hemisphere THC slow-downs (Heinrich events). The hypothesis of a weaker Northern Hemisphere THC intensity during Heinrich events is supported by the stable isotope values, Mg/Ca temperature and $\delta^{18}\text{O}_{\text{seawater}}$ estimations of the near surface dwelling planktonic foraminifer *G. ruber* and the upper thermocline dwelling foraminifer *P. obliquiloculata*, which indicate decreases in ITF intensity with a reduced transport of less saline water from the Pacific into the Indian Ocean.

In contrast, planktonic oxygen isotope records of *G. ruber* covary with high-latitude Northern Hemisphere temperature signals from Greenland with strong imprints of longer-lasting D-O events at site MD01-2378 and additionally shorter D-O events at site SO-185 18460. This Northern Hemisphere high-latitude climate signal was probably transmitted by the East Asian-Australian monsoon system.

A comparison of planktonic proxy-data with modern SST and salinity conditions at both sites reflects monsoon related climate variability in the Eastern Indian Ocean. This variability is linked to the insolation dependent position of the ITCZ on (semi-) precessional timescales. Compared to Core MD01-2378 the more northerly located Core SO-185 18460 apparently underwent higher variability due to the East Asian-Australian monsoon system. While conditions at the position of Core SO-185 18460 probably were drier during the first (semi-) precessional SE-monsoon and

the NW-monsoon phase, this site might be affected by fresh water advection from the Indonesian Archipelago during the second (semi-) precessional SE-monsoon phase. In contrast Core MD01-2378 experienced cooler and fresher conditions during the NW-monsoon phase due to the activity of tropical cyclones and the migration of the hydrological front between West Australian Current (WAC) and Leeuwin Current (LC).

5.3 Paleoproductivity in the Timor Sea

Benthic foraminiferal census counts and benthic foraminiferal accumulation rates of Cores MD01-2378 and SO-185 18460 reflect higher abundances of carbon-flux sensitive species (buliminids) during Southern Hemisphere stadials related to higher paleoproductivity probably induced by local upwelling or changes in bottom water circulation. Local upwelling at site MD01-2378 probably occurred due to increased vertical mixing related to tropical cyclone activity.

Higher buliminid abundances during Southern Hemisphere stadials also support the hypothesis of retreats of AAIW at site SO-185 18460. These are supposed to occur with decreases in bottom water ventilation probably related to a weaker Southern Ocean circulation with lower oxygen levels.

Regional differences in paleoceanographic settings in the Timor Sea may be supported by high accumulation rates of globocassidulinids at site MD01-2378, which may indicate a contrast in food sources between sites MD01-2378 and SO-185 18460. Increases in globocassidulinids in the outflow area of the Timor Sea are probably related to the migration of the hydrological front between the WAC and the LC during times of a weaker THC as also indicated by stable isotope values, Mg/Ca temperature and $\delta^{18}\text{O}_{\text{seawater}}$ estimations of the near surface dwelling planktonic foraminifer *G. ruber* and the upper thermocline dwelling foraminifer *P. obliquiloculata* at site MD01-2378.

Appendix A

Taxonomic list

| | |
|--|--|
| <i>Bulimina aculeata</i> (d'Orbigny) | Jones, 1994, p. 56, pl. 51, figs. 7–9. |
| <i>Bulimina marginata</i> (d'Orbigny) | Jones, 1994, p. 55, pl. 51, figs. 3–5. |
| <i>Bulimina mexicana</i> (Cushman) | Jones 1994, p. 56, pl. 51, figs. 10–13. |
| <i>Globobulimina</i> spp. | |
| <i>Globigerinoides ruber</i> (d'Orbigny) | Loeblich and Tappan, 1994, p. 107, pl. 206, figs. 10–12. |
| <i>Globocassidulina elegans</i> (Sidebottom) | Loeblich and Tappan 1994, p. 115, pl. 223, figs. 1–6. |
| <i>Globocassidulina subglobosa</i> (Brady) | Jones, 1994, p. 60, pl. 54, fig. 17. |
| <i>Planulina wuellerstorfi</i> (Schwager) | Loeblich and Tappan, 1994, p. 150, pl. 319, figs. 7–12. |
| <i>Pulleniatina obliquiloculata</i> (Parker and Jones) | Loeblich and Tappan, 1994, p. 103, pl. 188, figs. 1–6. |

Bibliography

- Adkins, J. F., A. P. Ingersoll, and C. Pasquero (2005), Rapid climate change and conditional instability of the glacial deep ocean from the thermobaric effect and geothermal heating, *Quaternary Science Reviews*, 24, 581–594, doi:10.1016/j.quascirev.2004.11.005. [2.4.1](#), [4.1](#)
- Alley, R. B., and P. U. Clark (1999), The Deglaciation of the Northern Hemisphere: A Global Perspective, *Annual Review of Earth and Planetary Sciences*, 27, 149–182, doi:10.1146/annurev.earth.27.1.149. [3.1](#), [3.4.2](#)
- Alley, R. B., J. Marotzke, W. D. Nordhaus, J. T. Overpeck, D. M. Peteet, R. A. Pielke Jr., R. T. Pierrehumbert, P. B. Rhines, T. F. Stocker, L. D. Talley, and J. M. Wallace (2003), Abrupt climate change, *Science*, 299, 2005–2010, doi:10.1126/science.1081056. [1.1.2](#)
- Altenbach, A. V. (1992), Short term processes and patterns in the foraminiferal response to organic flux rates, *Marine Micropaleontology*, 19, 119–129, doi:10.1016/0377-8398(92)90024-E. [2.4.2](#)
- Altenbach, A. V., and M. Sarnthein (1989), Productivity record in benthic foraminifera, in *Productivity of the Ocean: Past and Present*, edited by W. H. Berger, V. Smetacek, and G. Wefer, pp. 255–269, John Wiley, New York. [2.3.3](#), [4.5.3](#)
- Anand, P., H. Elderfield, and M. H. Conte (2003), Calibration of Mg/Ca thermometry in planktonic foraminifera from sediment trap time series, *Paleoceanography*, 18(2), 1050, doi: 10.1029/2002PA000846. [3.2.1](#), [3.1](#), [3.2.1](#), [3.4.1](#)
- Andersen, K. K., A. Svensson, S. J. Johnsen, S. O. Rasmussen, M. Bigler, R. Röthlisberger, U. Ruth, M.-L. Siggaard-Andersen, J. P. Steffensen, D. Dahl-Jensen, B. M. Vinther, and H. B. Clausen (2006), The Greenland Ice Core Chronology 2005, 15–42 ka. Part 1: constructing the time scale, *Quaternary Science Reviews*, 25, 3246–3257, doi:10.1016/j.quascirev.2006.08.002. [1.1.2](#), [2.3.1](#), [3.2.4](#), [4.1](#), [4.4.1](#), [5.1](#)
- Antonov, J. I., R. A. Locarnini, T. P. Boyer, A. V. Mishonov, and H. E. Garcia (2006), World Ocean Atlas 2005, Volume 2: Salinity, in *NOAA Atlas NESDIS 62*, edited by S. Levitus, p. 182, U.S. Government Printing Office, Washington, D.C. [3.1](#), [3.4.2](#)
- Arz, H. W., F. Lamy, A. Ganopolski, N. Nowaczyk, and J. Pätzold (2007), Dominant Northern Hemisphere climate control over millennial-scale glacial sea-level variability, *Quaternary Science Reviews*, 26(3-4), 312–321, doi:10.1029/2003GC000559. [3.4.3](#), [3.6](#)
- Atmadipoera, A., R. Molcard, G. Madec, S. Wijffels, J. Sprintall, A. Koch-Larrouy, I. Jaya, and A. Supagat (2009), Characteristics and variability of the Indonesian Throughflow Water at the Outflow Straits, *Deep-Sea Research I*, 56, 1942–1954, doi:10.1016/j.dsr.2009.06.004. [4.2](#), [4.5.2](#), [4.5.2](#)

- Barker, S., M. Greaves, and H. Elderfield (2003), A study of cleaning procedures used for foraminiferal Mg/Ca paleothermometry, *Geochemistry Geophysics Geosystems*, 4(9), 8407, doi:10.1029/2003GC000559. 3.2.1
- Bassinot, F., A. Holbourn, T. Kiefer, U. Pflaumann, and S. Rothe (Eds.) (2002), *WEPAMA Cruise MD 122 / IMAGES VII, Réf: OCE/2002/01*, vol. 68, 225 pp., Inst. Polaire Français - IPEV, Plouzané, France. 2.2.1
- Bé, A. W. H. (1977), An ecological, zoogeographic and taxonomic review of recent planktonic foraminifera, in *Oceanic Micropaleontology, Vol. 1*, edited by A. T. S. Ramsay, pp. 1–100, Academic Press, London. 3.4.1
- Bemis, B. E., H. J. Spero, J. Bijma, and D. W. Lea (1998), Reevaluation of the oxygen isotopic composition of planktonic foraminifera: Experimental results and revised paleotemperature equations, *Paleoceanography*, 13(2), 150–160, doi:10.1029/98PA00070. 3.2.3, 1
- Berger, A., and M. F. Loutre (1991), Insolation Values for the Climate of the last 10 Million Years, *Quaternary Science Reviews*, 10, 297–317, doi:10.1016/0277-3791(91)90033-Q. 1.1.1
- Blunier, T., and E. J. Brook (2001), Timing of millennial-scale climate change in Antarctica and Greenland during the last glacial period, *Science*, 291, 109–112, doi:10.1126/science.291.5501.109. 1.1.2, 1.1.2, 2.4.1, 3.1, 4.1, 4.1, 4.4.2, 4.5.1
- Blunier, T., J. Chappellaz, J. Schwander, A. Dallenbach, B. Stauffer, T. F. Stocker, D. Raynaud, J. Jouzel, H. B. Clausen, C. U. Hammer, and S. J. Johnsen (1998), Asynchrony of Antarctic and Greenland climate change during the last glacial period, *Nature*, 394, 739–743, doi:10.1038/29447. 1.1.2, 1.1.2, 3.1, 4.1, 4.1, 4.5, 4.5.1
- Bond, G. C., and R. Lotti (1995), Iceberg Discharges into the North Atlantic on Millennial Time Scales During the Last Glaciation, *Science*, 267, 1005–1010, doi:10.1126/science.267.5200.1005. 4.1
- Bond, G. C., W. Broecker, S. Johnsen, J. McManus, L. Labeyrie, J. Jouzel, and G. Bonani (1993), Correlations between climate records from North Atlantic sediments and Greenland ice, *Nature*, 365, 143–147, doi:10.1038/365143a0. 1.1.2, 1.1.2
- Broecker, W. S. (1998), Paleocan circulation during the last deglaciation: A bipolar seesaw?, *Paleoceanography*, 13(2), 119–121, doi:10.1029/97PA03707. 1.1.2, 2.4.1, 3.4.2, 4.1, 4.5
- Broecker, W. S. (2003), Does the Trigger for Abrupt Climate Change Reside in the Ocean or in the Atmosphere?, *Science*, 300, 1519–1522, doi:10.1126/science.1083797. 3.1, 3.4.2
- Burns, S. J., D. Fleitmann, A. Matter, J. Kramers, and A. A. Al-Subbary (2003), Indian Ocean Climate and an Absolute Chronology over Dansgaard/Oeschger Events 9 to 13, *Science*, 301, 1365–1367, doi:10.1126/science.1086227. 1.1.2, 2.4.1, 4.5.2
- Butzin, M., M. Prange, and G. Lohmann (2005), Radiocarbon simulations for the glacial ocean: the effects of wind stress, Southern Ocean sea ice and Heinrich events, *Earth and Planetary Science Letters*, 235, 45–61, doi:10.1016/j.epsl.2005.03.003. 2.2.3, 4.3.2
- Cacho, I., J. O. Grimalt, C. Pelejero, M. Canals, F. J. Sierro, J. A. Flores, and N. Shackleton (1999), Dansgaard-Oeschger and Heinrich Event Imprints in Alboran Sea Paleotemperatures, *Paleoceanography*, 14, 698–705, doi:10.1029/1999PA900044. 3.1

- Cane, M., and P. Molnar (2001), Closing of the Indonesian Seaway as a precursor to East African aridification around 3–4 million years ago, *Nature*, *411*, 157–162, doi:10.1038/35075500. [1.1.1](#)
- Chappell, J. (2002), Sea level changes forced ice breakouts in the Last Glacial cycle: new results from coral terraces, *Quaternary Science Reviews*, *21*, 1229–1240, doi:10.1016/S0277-3791(01)00141-X. [1.1.2](#), [1.1.2](#), [2.1](#)
- Chappell, J., A. Omura, T. Esat, M. McCulloch, J. Pandolfi, Y. Ota, and B. Pillans (1996), Reconciliation of late Quaternary sea levels derived from coral terraces at Huon Peninsula with deep sea oxygen isotope records, *Earth and Planetary Science Letters*, *141*(1–4), 227–236, doi:10.1016/0012-821X(96)00062-3. [3.6](#)
- Chen, Y. (2009), Climate instability during the last glaciation recorded in the Yuanbu loess section, *Progress in Natural Science*, *19*(4), 453–459, doi:10.1016/j.pnsc.2008.06.026. [1.1.1](#)
- Chlachula, J. (2003), The Siberian loess record and its significance for reconstruction of Pleistocene climate change in north-central Asia, *Quaternary Science Reviews*, *22*(18–19), 1879–1906, doi:10.1016/S0277-3791(03)00182-3. [1.1.1](#)
- Clark, P. U., N. G. Pisias, T. F. Stocker, and A. J. Weaver (2002), The role of the thermohaline circulation in abrupt climate change, *Nature*, *415*, 863–869, doi:10.1038/415863a. [1.1.2](#)
- Clark, P. U., S. W. Hostetler, N. G. Pisias, A. Schmittner, and K. J. Meissner (2007), Mechanisms for an 7-kyr Climate and Sea-Level Oscillation during Marine Isotope Stage 3, in *Ocean Circulation: Mechanisms and Impacts - Past and Future Changes of the Ocean's Meridional Overturning*, vol. AGU Monograph 173, edited by A. Schmittner, J. C. H. Chiang, and S. R. Hemming, pp. 209–246, American Geophysical Union (AGU), Washington D.C. [3.1](#), [4.5.2](#), [4.5.2](#)
- Clement, A. C., and M. A. Cane (1999), A role for the tropical Pacific coupled ocean-atmosphere system on Milankovitch and millennial timescales. Part I: A modeling study of tropical Pacific variability, in *Mechanisms of Global Climate Change at Millennial Time Scales*, vol. Geophysical Monograph 112, edited by P. U. Clark, R. S. Webb, and L. D. Keigwin, pp. 363–371, American Geophysical Union (AGU), Washington D.C. [1.1.2](#)
- Cléroux, C., E. Cortijo, J.-C. Duplessy, and R. Zahn (2007), Deep-dwelling foraminifera as thermocline temperature recorders, *Geochemistry Geophysics Geosystems*, *8*, Q04N11, doi:10.1029/2006GC001474. [3.4.1](#), [3.5](#)
- Cresswell, G. R. (1991), The Leeuwin Current - observations and recent models, *The Journal of the Royal Society of Western Australia*, *74*, 1–14. [2.4.2](#), [4.2](#)
- Dannenmann, S., B. K. Linsley, D. W. Oppo, Y. Rosenthal, and L. Beaufort (2003), East Asian monsoon forcing of suborbital variability in the Sulu Sea during Marine Isotope Stage 3: Link to Northern Hemisphere climate, *Geochemistry Geophysics Geosystems*, *4*(1), 1–13, doi:10.1029/2002GC000390. [1.1.2](#), [2.1](#), [3.1](#), [3.4.2](#)
- Dansgaard, W., S. J. Johnsen, H. B. Clausen, D. Dahl-Jensen, N. S. Gundestrup, C. U. Hammer, C. S. Hvidberg, J. P. Steffensen, A. E. Sveinbjörnsdóttir, J. Jouzel, and G. Bond (1993), Evidence for general instability of past climate from a 250-kyr ice-core record, *Nature*, *364*, 218–220, doi:10.1038/364218a0. [1.1.2](#), [1.1.3](#), [2.1](#), [4.1](#), [4.5](#)

- De Deckker, P., N. J. Tapper, and S. van der Kaars (2003), The status of the Indo-Pacific Warm Pool and adjacent land at the Last Glacial Maximum, *Global and Planetary Change*, 35, 25–35, doi:10.1016/S0921-8181(02)00089-9. 3.4.2
- Ding, Z. L., E. Derbyshire, S. L. Yang, Z. W. Yu, S. F. Xiong, and T. S. Liu (2002), Stacked 2.6-Ma grain size record from the Chinese loess based on five sections and correlation with the deep-sea $\delta^{18}\text{O}$ record, *Paleoceanography*, 17, doi:10.1029/2001PA000725. 1.1.1
- Dürkop, A., A. Holbourn, W. Kuhnt, R. Zuraida, N. Andersen, and P. M. Grootes (2008), Centennial-scale climate variability in the Timor Sea during Marine Isotope Stage 3, *Marine Micropaleontology*, 66(3), 208–221, doi:10.1016/j.marmicro.2007.10.002. 3.2.2, 3.2.4, 3.2, 3.2, 3.3, 3.4, 3.4.2, 3.4.3, 4.1, 4.3.3, 4.5, 4.5, 4.5.1, 4.5.2, 4.5.2, 4.5.3
- Dykoski, C. A., R. L. Edwards, H. Cheng, D. Yuan, Y. Cai, M. Zhang, Y. Lin, J. Qing, Z. An, and J. Revenaugh (2006), A high-resolution, absolute-dated Holocene and deglacial Asian monsoon record from Dongge Cave, China, *Earth and Planetary Science Letters*, 233, 71–86, doi:10.1016/j.epsl.2005.01.036. 1.1.2, 1.1.2
- Eggins, S., P. De Deckker, and J. Marshall (2003), Mg/Ca variation in planktonic foraminifera tests: implications for reconstructing palaeo-seawater temperature and habitat migration, *Earth and Planetary Science Letters*, 212, 291–306, doi:10.1016/S0012-821X(03)00283-8. 3.4.1
- England, M. H. (1992), On the Formation of Antarctic Intermediate and Bottom Water in Ocean General Circulation Models, *Journal of Physical Oceanography*, 22, 918–926, doi:10.1175/1520-0485(1992)022. 2.4.1
- EPICA Community Members (2004), Eight glacial cycles from an Antarctic ice core, *Nature*, 429, 623–628, doi:10.1038/nature02599. 1.1.1, 2.1, 2.3.1, 3.2.4, 4.4.1, 4.5.1
- EPICA Community Members (2006), One-to-one coupling of glacial climate variability in Greenland and Antarctica, *Nature*, 444, 195–198, doi:10.1038/nature05301. 1.1, 1.1.2, 2.3.1, 3.1, 3.2.4, 4.1, 4.1, 4.4.1, 4.4.2, 4.5, 4.5, 5.1
- Ericksen, A. (2008), Impact of calcite dissolution on Mg/Ca ratios of core-top planktonic foraminifera from the Timor Sea, Master's thesis, Christian-Albrechts-Universität zu Kiel, Germany. 3.2.1
- Fairbanks, R. G., R. A. Mortlock, T.-C. Chiu, L. Cao, A. Kaplan, T. P. Guilderson, T. W. Fairbanks, A. L. Bloom, P. M. Grootes, and M.-J. Nadeau (2005), Radiocarbon calibration curve spanning 0 to 50 000 years BP based on paired $^{230}\text{Th}/^{234}\text{U}/^{238}\text{U}$ and ^{14}C dates on pristine corals, *Quaternary Science Reviews*, 24, 10.1016/j.quascirev.2005.04.007. 2.2.3, 4.3.2
- Ganopolski, A., and S. Rahmstorf (2001), Rapid changes of glacial climate simulated in a coupled climate model, *Nature*, 409, 153–158, doi:10.1038/35051500. 1.1.2, 3.1, 3.4.2
- Godfrey, J., and A. Weaver (1991), Is the Leeuwin Current driven by Pacific heating and winds?, *Progress in Oceanography*, 27, 225–272, doi:10.1016/0079-6611(91)90026-I. 2.2.1
- Gooday, A. J. (1988), A response by benthic foraminifera to the deposition of phytodetritus in the deep sea, *Nature*, 332, 70–73, doi:10.1038/332070a0. 2.4.2
- Gooday, A. J. (1993), Deep-sea benthic foraminiferal species which exploit phytodetritus: characteristic features and controls on distribution, *Marine Micropaleontology*, 22, 187–205, doi:10.1016/0377-8398(93)90043-W. 2.4.2

- Gordon, A. L. (2005), Oceanography of the Indonesian Seas and their throughflow, *Oceanography*, 18(4), 14–27. 2.1, 3.4.2, 3.4.3, 4.1, 4.5.3
- Gordon, A. L., R. D. Susanto, and K. Vranes (2003), Cool Indonesian throughflow as a consequence of restricted surface layer flow, *Nature*, 425, 824–828, doi:10.1038/nature02038. 3.4.3
- Grootes, P. M., and M. Sarnthein (2006), Marine ¹⁴C reservoir ages oscillate, *Pages News*, 14(3), 18–19. 2.3.1, 4.4.1, 5.1
- Grootes, P. M., M. Stuiver, J. W. C. White, S. J. Johnsen, and J. Jouzel (1993), Comparison of oxygen isotope records from the GISP2 and GRIP Greenland ice cores, *Nature*, 366, 552–554, doi:10.1038/366552a0. 1.1.2, 1.1.3, 2.1, 4.1, 4.1, 4.5
- Heinrich, H. (1988), Origin and consequences of cyclic ice rafting in the Northeast Atlantic Ocean during the past 130,000 years, *Quaternary Research*, 29(2), 142–152, doi:10.1016/0033-5894(88)90057-9. 1.1.2, 4.1
- Hemleben, C., M. Spindler, and O. R. Anderson (Eds.) (1989), *Modern Planktonic Foraminifera*, 363 pp., Springer-Verlag, New York. 3.4.1
- Hemming, S. R. (2004), Heinrich events: Massive late Pleistocene detritus layers of the North Atlantic and their global climate imprint, *Reviews of Geophysics*, 42, 1–43, doi:10.1029/2003RG000128, rG1005. 1.1.2, 3.4.2
- Hendy, I. L., and J. P. Kennett (2000), Dansgaard-Oeschger Cycles and the California Current System: Planktonic Foraminiferal Response to Rapid Climate Change in Santa Barbara Basin, Ocean Drilling Program Hole 893A, *Paleoceanography*, 15, 30–42, doi:10.1029/1999PA000413. 3.1
- Herguera, J. C. (2000), Last glacial paleoproductivity patterns in the eastern equatorial Pacific: benthic foraminifera records, *Marine Micropaleontology*, 40, 259–275, doi:10.1016/S0377-8398(00)00041-4. 2.3.3, 4.4.3, 4.5.3
- Herguera, J. C., and W. H. Berger (1991), Paleoproductivity from benthic foraminifera abundance: glacial to postglacial change in the west-equatorial Pacific, *Geology*, 19, 1173–1176, doi:10.1130/0091-7613(1991)019. 2.3.3, 4.3.3, 4.5.3
- Hodell, D. A., K. A. Venz, C. D. Charles, and U. S. Ninnemann (2003), Pleistocene vertical carbon isotope and carbonate gradients in the South Atlantic sector of the Southern Ocean, *Geochemistry Geophysics Geosystems*, 4, 1–19, doi:10.1029/2002GC000367. 4.5.1
- Holbourn, A., W. Kuhnt, H. Kawamura, Z. Jian, P. Grootes, H. Erlenkeuser, and J. Xu (2005), Orbitally paced paleoproductivity variations in the Timor Sea and Indonesian Throughflow variability during the last 460 kyr, *Paleoceanography*, 20, doi:10.1029/2004PA001094. 1.1.3, 2.1, 2.2.1, 2.2.2, 2.2.4, 2.3.1, 2.3, 2.3.3, 2.4.2, 3.1, 3.2.1, 4.1, 4.3.3, 4.5.2, 4.5.3
- Huber, C., M. Leuenberger, R. Spahni, J. Flückiger, J. Schwander, T. F. Stocker, S. Johnsen, A. Landais, and J. Jouzel (2006), Isotope calibrated Greenland temperature record over Marine Isotope Stage 3 and its relation to CH₄, *Earth and Planetary Science Letters*, 245, 504–519, doi:10.1016/j.epsl.2006.01.002. 1.1.2, 2.1, 3.1, 4.1

- Hughen, K., S. Lehman, J. Southon, J. Overpeck, O. Marchal, C. Herring, and J. Turnbull (2004), ^{14}C activity and global carbon cycle changes over the past 50 000 years, *Science*, 303, 202–207, doi:10.1126/science.1090300. 2.3.1, 2.3.1, 4.4.1, 5.1
- Hung, C.-W., X. Liu, and M. Yanai (2004), Symmetry and Asymmetry of the Asian and Australian Summer Monsoons, *Journal of Climate*, 17, 2413–2426, doi:10.1175/1520-0442(2004)017. 2.4.1, 4.5.2
- Illahude, A. G., and A. L. Gordon (1996), Thermocline stratification within the Indonesian Seas, *Journal of Geophysical Research*, 101(C5), 401–412, doi:10.1029/95JC03798. 3.1
- Jansen, E., J. Overpeck, K. Briffa, J.-C. Duplessy, F. Joos, V. Masson-Delmotte, D. Olago, B. Otto-Bliesner, W. Peltier, S. Rahmstorf, R. Ramesh, D. Raynaud, D. Rind, O. Solomina, R. Villalba, and D. Zhang (2007), Palaeoclimate, in *Climate Change 2007: The Physical Science Basis. Contribution of Working Group I to the Fourth Assessment Report of the Intergovernmental Panel on Climate Change*, edited by S. Solomon, D. Qin, M. Manning, Z. Chen, M. Marquis, K. Averyt, M. Tignor, and H. Miller, pp. 433–498, Cambridge University Press, Cambridge, United Kingdom and New York, NY, USA. 1.1, 1.1.2
- Jian, Z., B. Huang, W. Kuhnt, and H. L. Lin (2001), Late Quaternary upwelling intensity and East Asian monsoon forcing in the South China Sea, *Quaternary Research*, 55, 363–370, doi: 10.1006/qres.2001.2231. 2.2.2
- Jian, Z. M., L. J. Wang, M. Kienast, M. Sarnthein, W. Kuhnt, H. L. Lin, and P. X. Wang (1999), Benthic foraminiferal paleoceanography of the South China Sea over the last 40 000 years, *Marine Geology*, 156(1), 159–186, doi:10.1016/S0025-3227(98)00177-7. 2.3.3
- Jin, L., F. Chen, A. Ganopolski, and M. Claussen (2007), Response of East Asian climate to Dansgaard/Oeschger and Heinrich events in a coupled model of intermediate complexity, *Journal of Geophysical Research*, 112, 1–14, doi:10.1029/2006JD007316. 4.5.2
- Johnsen, S. J., W. Dansgaard, H. B. Clausen, and C. C. Langway (1972), Oxygen Isotope Profiles through the Antarctic and Greenland Ice Sheets, *Nature*, 235, 429–434, doi:10.1038/235429a0. 1.1.2, 4.1, 4.5.1
- Johnsen, S. J., H. B. Clausen, W. Dansgaard, K. Fuhrer, N. Gundestrup, C. U. Hammer, P. Iversen, J. Jouzel, B. Stauffer, and J. P. Steffensen (1992), Irregular glacial interstadials recorded in a new Greenland ice core, *Nature*, 359, 311–313, doi:10.1038/359311a0. 1.1.2, 1.1.3, 2.1, 4.1
- Jones, R. W. (1994), *The Challenger Foraminifera*, 149 pp., Oxford University Press, New York.
- Jorissen, F. J., H. C. de Stigter, and J. G. V. Widmark (1995), A conceptual model explaining benthic foraminiferal microhabitats, *Marine Micropaleontology*, 26(1–4), 3–15, doi:10.1016/0377-8398(95)00047-X. 4.5.3
- Jouzel, J., C. Lorius, J. R. Petit, C. Genthon, N. I. Barkov, V. M. Kotlyakov, and V. M. Petrov (1987), Vostok ice core: a continuous isotope temperature record over the last climatic cycle (160,000 years), *Nature*, 329, 403–408, doi:10.1038/329403a0. 1.1.2, 4.1, 4.5.1
- Jung, S. J., D. Kroon, G. Ganssen, F. Peeters, and R. Ganeshram (2009), Enhanced Arabian Sea intermediate water flow during glacial North Atlantic cold phases, *Earth and Planetary Science Letters*, 280, 220–228, doi:10.1016/j.epsl.2009.01.037. 4.5

- Knutti, R., J. Flückiger, T. F. Stocker, and A. Timmermann (2004), Strong hemispheric coupling of glacial climate through freshwater discharge and ocean circulation, *Nature*, 430, 851–856, doi:10.1038/nature02786. 2.4.1
- Koch-Larrouy, A., G. Madec, B. Blanke, and R. Molcard (2008), Water mass transformation along the Indonesian throughflow in an OGCM, *Ocean Dynamics*, 58(3–4), 289–309, doi:10.1007/s10236-008-0155-4. 4.2
- Kuhnt, W. (2005), Cruise report SONNE-185 "Variability of the Indonesian Throughflow and Australasian climate history of the last 150 000 years (VITAL)". 2.2.1, 3.2.1, 1, 3.5
- Kuhnt, W., A. Holbourn, R. Hall, M. Žuvela, and R. Käse (2004), Neogene history of the Indonesian Throughflow, in *Continent-Ocean Interactions Within East Asia Marginal Seas, Geophysical Monograph Series*, vol. 149, edited by Peter Clift et al., pp. 299–320, AGU, Washington D.C. 1.1.3, 2.1, 2.2.1
- Labeyrie, L. D., J.-C. Duplessy, and P. L. Blanc (1987), Variations in mode of formation and temperature of oceanic deep waters over the past 125,000 years, *Nature*, 327, 477–482, doi:10.1038/327477a0. 1
- Labitzke, K., and K. Matthes (2003), Eleven-year solar cycle variations in the atmosphere: observations, mechanisms and models, *The Holocene*, 13(3), 311–317, 10.1191/0959683603hl623rp. 1.1.1
- Landais, A., N. Caillon, C. Goujon, A. Grachev, J. Barnola, J. Chappellaz, J. Jouzel, V. Masson-Delmotte, and M. Leuenberger (2004), Quantification of rapid temperature change during DO event 12 and phasing with methane inferred from air isotopic measurements, *Earth and Planetary Science Letters*, 225, 221–232, doi:10.1016/j.epsl.2004.06.009. 1.1.2, 2.1, 4.1
- Laskar, J., P. Robutel, F. Joutel, M. Gastineau, A. C. M. Correia, and B. Lestrade (2004), A long-term numerical solution for the insolation quantities of the Earth, *Astronomy and Astrophysics*, 428(1), 261–285. 1.1.1
- Ledley, T. S., E. T. Sundquist, S. E. Schwartz, D. K. Hall, J. D. Fellows, and T. L. Killeen (1999), Climate Change and Greenhouse Gases, *EOS Transactions, American Geophysical Union*, 80(39), 453. 1.1.1
- Levi, C., L. D. Labeyrie, F. C. Bassinot, F. Guichard, E. Cortijo, C. Waelbroeck, N. Caillon, J. Duprat, T. de Garidel-Thoron, and H. Elderfield (2007), Low-latitude hydrological cycle and rapid climate changes during the last deglaciation, *Geochemistry Geophysics Geosystems*, 5, doi:10.1029/2006GC001514. 3.1, 3.4.2
- Lin, H., L. C. Peterson, J. T. Overpeck, S. E. Trumbore, and D. W. Murray (1997), Late Quaternary climate change from $\delta^{18}\text{O}$ records of multiple species of planktonic foraminifera: High-resolution records from the anoxic Cariaco Basin, Venezuela, *Paleoceanography*, 12(3), 415–427, doi:10.1029/97PA00230. 3.4.1
- Lin, I., W. T. Liu, C.-C. Wu, G. T. F. Wong, C. Hu, Z. Chen, W.-D. Liang, Y. Yang, and K.-K. Liu (2003), New evidence for enhanced ocean primary production triggered by tropical cyclone, *Geophysical Research Letters*, 30(13), 1718, doi:10.1029/2003GL017141. 2.4.2
- Lisiecki, L. E., and M. E. Raymo (2005), A Pliocene-Pleistocene stack of 57 globally distributed benthic $\delta^{18}\text{O}$ records, *Paleoceanography*, 20, 1–20, doi:10.1029/2004PA001071. 1.1.1, 1.1.2

- Locarnini, R. A., A. V. Mishonov, J. I. Antonov, T. P. Boyer, and H. E. Garcia (2006), World Ocean Atlas 2005, Volume 1: Temperature, in *NOAA Atlas NESDIS 61*, edited by S. Levitus, p. 182, U.S. Government Printing Office, Washington, D.C. [3.1](#), [3.2.1](#), [3.2](#), [3.3.2](#), [3.3](#), [3.4.2](#)
- Loeblich, A. R., and H. Tappan (1994), *Foraminifera of the Sahul Shelf and Timor Sea*, 661 pp., Cushman Foundation for Foraminiferal Research, Cambridge (U.S.A.).
- Longhurst, A. R. (1998), *Ecological Geography of the Sea*, 398 pp., Academic Press, San Diego. [2.2.1](#)
- Loubere, P. (1991), Deep-sea benthic foraminiferal assemblage response to a surface ocean productivity gradient: a test, *Paleoceanography*, *6*, 193–204, doi:10.1029/90PA02612. [2.4.2](#)
- Loubere, P. (1994), Quantitative estimation of surface ocean productivity and bottom water oxygen concentration using benthic foraminifera, *Paleoceanography*, *9*, 723–737, doi:10.1029/94PA01624. [2.4.2](#)
- Loubere, P. (1996), The surface ocean productivity and bottom water oxygen signals in deep water benthic foraminiferal assemblages, *Marine Micropaleontology*, *28*, 247–261, doi:10.1016/0377-8398(96)00004-7. [2.4.2](#), [4.4.3](#)
- Lutze, G. F., and W. T. Coulbourn (1984), Recent benthic foraminifera from the continental margin of northwest Africa: community structure and distribution, *Marine Micropaleontology*, *8*, 361–401, doi:10.1016/0377-8398(84)90002-1. [2.3.3](#), [4.5.3](#)
- Lynch-Stieglitz, J. (2004), Ocean Science: Hemispheric Asynchrony of Abrupt Climate Change, *Science*, *304*, 1919–1920, doi:10.1126/science.1100374. [3.1](#)
- Manabe, S., and R. J. Stouffer (1997), Coupled ocean-atmosphere model response to freshwater input: Comparison to Younger Dryas event, *Paleoceanography*, *12*, 321–336. [4.1](#)
- Marchal, O., T. F. Stocker, and F. Joos (1998), Impact of oceanic reorganizations on the ocean carbon cycle and atmospheric carbon dioxide content, *Paleoceanography*, *13*, 225–244. [4.1](#)
- Martrat, B., J. Grimalt, N. J. Shackleton, L. de Abreu, M. A. Hutterli, and T. F. Stocker (2007), Four climate cycles of recurring deep and surface water destabilizations on the Iberian Margin, *Science*, *317*, 502–507, doi:10.1126/science.1139994. [1.1.2](#), [2.4.1](#), [4.1](#), [4.1](#), [4.5](#)
- Matsumoto, K., and R. M. Key (2004), Natural radiocarbon distribution in the deep ocean, in *Global Environmental Change in the Ocean and on Land*, edited by M. Shiyomi et al., pp. 45–58, Terrapub, Tokyo. [2.4.1](#), [4.5.1](#)
- McCartney, M. S. (1977), Subantarctic Mode Water, in *A Voyage of Discovery: George Deacon 70th Anniversary Volume*, edited by M. V. Angel, pp. 103–119, Pergamon Press, Oxford. [2.4.1](#)
- McCorkle, D. C., D. T. Heggie, and H. H. Veeh (1998), Glacial and Holocene stable isotope distributions in the southeastern Indian Ocean, *Paleoceanography*, *13*(1), 20–34, doi:10.1029/97PA02305. [2.4.1](#), [2.4.2](#)
- McCorkle, D. C., H. H. Veeh, and D. T. Heggie (1999), Glacial-interglacial paleoceanography from Australian margin sediments: northwest Australian margin and Great Australian Bight, *Journal of Australian Geology and Geophysics*, *17*(5/6), 145–157. [4.5.3](#)

- Miller, G., J. Mangan, D. Pollard, S. Thompson, B. Felzer, and J. Magee (2005), Sensitivity of the Australian Monsoon to insolation and vegetation: Implications for human impact on continental moisture balance, *Geology*, 33, 65–68, doi:10.1130/G21033.1. 1.1.2, 2.1, 4.5.2
- Mulitza, S., M. Prange, J.-B. Stuut, M. Zabel, T. von Dobeneck, A. C. Itambi, J. Nizou, and M. Schulz (2008), Sahel megadroughts triggered by glacial slowdowns of Atlantic meridional overturning, *Paleoceanography*, 23, 1–11, doi:10.1029/2008PA001637. 4.5
- Müller, A., and B. N. Opdyke (2000), Glacial-interglacial changes in nutrient utilization and paleoproductivity in the Indonesian Throughflow sensitive Timor Trough, easternmost Indian Ocean, *Paleoceanography*, 15(1), 85–94, doi:10.1029/1999PA900046. 1.1.3, 2.1
- Muller, J., M. Kylander, R. A. J. Wüst, D. Weiss, A. Martinez-Cortizas, A. N. LeGrande, T. Jennerjahn, H. Behling, W. T. Anderson, and G. Jacobson (2008), Possible evidence for wet Heinrich phases in tropical NE Australia: The Lynch's Crater deposit, *Quaternary Science Reviews*, 27, 468–475, doi:10.1016/j.quascirev.2007.11.006. 3.1
- Murgese, D. S., and P. De Deckker (2007), The Late Quaternary evolution of water masses in the eastern Indian Ocean between Australia and Indonesia, based on benthic foraminifera faunal and carbon isotopes analyses, *Palaeogeography, Palaeoclimatology, Palaeoecology*, 247, 382–401, doi:10.1016/j.palaeo.2006.11.002. 3.1, 4.5.3
- Murgese, D. S., P. De Deckker, M. I. Spooner, and M. Young (2008), A 35,000 year record of changes in the eastern Indian Ocean offshore Sumatra, *Palaeogeography, Palaeoclimatology, Palaeoecology*, 256, 195–213, doi:10.1016/j.palaeo.2008.06.001. 4.5.3
- Nadeau, M.-J., M. Schleicher, P. M. Grootes, H. Erlenkeuser, A. Gott dang, D. J. W. Mous, M. Sarnthein, and H. Willkomm (1997), The Leibniz-Labor AMS facility at the Christian-Albrechts Universität Kiel, Germany, *Nuclear Instruments and Methods in Physics Research, Section B*(123), 22–30. 2.2.3, 4.3.2
- NGRIP members (2004), High-resolution record of Northern Hemisphere climate extending into the last interglacial period, *Nature*, 43, 147–151, doi:10.1038/nature02805. 1.1.2, 2.3.1, 4.1, 4.4.1
- NODC (2001), National Oceanographic Data Center, World Ocean Atlas 2001: Objective Analyses, Data Statistics, and Figures, *CD-ROM Documentation*, National Oceanic and Atmospheric Administration, Silver Spring, Md., <http://www.nodc.noaa.gov/>. 1.4, 4.2, 4.5.2
- Oppo, D. W., and Y. Sun (2005), Amplitude and timing of sea-surface temperature change in the northern South China Sea: Dynamic link to the East Asian monsoon, *Geology*, 33(10), 785–788, doi:10.1130/G21867.1. 4.5.2
- Pahnke, K., and R. Zahn (2005), Southern Hemisphere Water Mass Conversion Linked with North Atlantic Climate Variability, *Science*, 307, 1741–1746, doi:10.1126/science.1102163. 3.3.4, 4.5, 4.5.1
- Partin, J. W., K. M. Cobb, J. F. Adkins, B. Clark, and D. P. Fernandez (2007), Millennial-scale trends in West Pacific Warm Pool hydrology since the Last Glacial Maximum, *Nature*, 449, 452–455, doi:10.1038/nature06164. 3.1
- Pearce, A. F., and G. R. Cresswell (1985), Ocean circulation off Western Australia and the Leeuwin Current, *CSIRO Information Service Sheet*, 16–3, 1–4. 2.4.2, 4.2

- Pearson, P. N., and M. R. Palmer (1999), Middle Eocene Seawater pH and Atmospheric Carbon Dioxide Concentrations, *Science*, 284, 1824–1826, doi:10.1126/science.284.5421.1824. 1.1.1
- Peter, B. N., P. Sreeraj, and K. G. V. Kumar (2005), Structure and variability of the Leeuwin Current in the south eastern Indian Ocean, *Journal of the Indian Geophysical Union*, 9(2), 107–119. 2.2.1
- Pflaumann, U., and Z. Jian (1999), Modern distribution patterns of planktonic foraminifera in the South China Sea and western Pacific: a new transfer technique to estimate regional sea-surface temperatures, *Marine Geology*, 156(1–4), 41–83. 3.4.1
- Piotrowski, A. M., S. L. Goldstein, S. R. Hemming, and R. G. Fairbanks (2004), Intensification and variability of ocean thermohaline circulation through the last deglaciation, *Earth and Planetary Science Letters*, 225(1–2), 205–220, doi:10.1016/j.epsl.2004.06.002. 3.1, 3.4.2
- Piotrowski, A. M., S. L. Goldstein, S. R. Hemming, and R. G. Fairbanks (2005), Temporal relationships of carbon cycling and ocean circulation at glacial boundaries, *Science*, 307, 1933–1938, doi:10.1126/science.1104883. 3.3.4
- Prell, W. L., and J. E. Damuth (1978), The climate-related diachronous disappearance of *Pulleniatina obliquiloculata* in late Quaternary sediments of the Atlantic and Caribbean, *Marine Micropaleontology*, 3(3), 267–277, doi:10.1016/0377-8398(78)90031-2. 3.4.1
- Ravelo, A. C., and R. G. Fairbanks (1992), Oxygen Isotopic Composition of Multiple Species of Planktonic Foraminifera: Recorders of the Modern Photic Zone Temperature Gradient, *Paleoceanography*, 7(6), 815–831, doi:10.1029/92PA02092. 3.4.1, 3.5
- Ravelo, A. C., R. G. Fairbanks, and S. G. H. Philander (1990), Reconstructing tropical Atlantic hydrography using planktonic foraminifera and an ocean model, *Paleoceanography*, 5, 409–431, doi:10.1029/90PA00484. 3.4.1
- Rohling, E. J. (2004), Progress in paleosalinity: Overview and presentation of a new approach, *Paleoceanography*, 22, PA3215, doi:10.1029/2007PA001437. 3.2.3
- Rosenthal, Y., D. W. Oppo, and B. K. Linsley (2003), The amplitude and phasing of climate change during the last deglaciation in the Sulu Sea, western equatorial Pacific, *Geophysical Research Letters*, 30(8), 1428, doi:10.1029/2002GL016612. 3.4.2
- Ruddiman, W. F. (2006), Orbital changes and climate, *Quaternary Science Reviews*, 25, 3092–3112, doi:10.1016/j.quascirev.2006.09.001. 1.1.1
- Ruth, U., M. Bigler, R. Röthlisberger, M.-L. Siggaard-Andersen, S. Kipfstuhl, K. Goto-Azuma, M. E. Hansson, S. J. Johnsen, H. Lu, and J. P. Steffensen (2007), Ice core evidence for a very tight link between North Atlantic and East Asian glacial climate, *Geophysical Research Letters*, 34, doi:10.1029/2006GL027876. 1.1.2, 2.1, 2.4.1, 4.4.2, 4.5.2, 4.5.2
- Sarnthein, M., and K. Winn (1977), Reconstruction of low and middle latitude export productivity, 30000 years B.P. to present: implications for global carbon reservoirs, in *Climate Ocean Interaction*, edited by M. E. Schlesinger, pp. 317–342, Springer, New York. 2.2.2
- Sarnthein, M., K. Winn, S. J. A. Jung, J.-C. Duplessy, L. Labeyrie, H. Erlenkeuser, and G. Ganssen (1994), Changes in East Atlantic deepwater circulation over the last 30,000 years: Eight time slice reconstructions, *Paleoceanography*, 9(2), 209–267, doi:10.1029/93PA03301. 3.1, 3.4.2

- Sarnthein, M., K. Stattegger, D. Dreger, H. Erlenkeuser, P. M. Grootes, B. Haupt, S. Jung, T. Kiefer, W. Kuhnt, U. Pflaumann, C. Schäfer-Neth, M. Schulz, D. Seidov, J. Simstich, S. van $^{\circ}$ C-Alfane, E. Vogelsang, V. A., and M. Weinelt (2001), Fundamental modes and abrupt changes in North Atlantic circulation and climate over the last 60 ky - Numerical modelling and reconstruction, in *The Northern North Atlantic: A Changing Environment*, edited by P. Schäfer, W. Ritzrau, M. Schlüter, and J. Thiede, Springer, Berlin. 3.1, 3.4.2
- Sarnthein, M., P. M. Grootes, J. P. Kennett, and M.-J. Nadeau (2007), 14 C reservoir ages show deglacial changes in ocean currents and carbon cycle, in *Ocean Circulation: Mechanisms and Impacts - Past and Future Changes of Meridional Overturning*, vol. 173, edited by A. Schmittner, J. C. H. Chiang, and S. R. Hemming, pp. 175–196, American Geophysical Union, AGU Geophysical Monograph, Washington D. C. 2.3.1, 4.4.1, 5.1
- Schleicher, M., P. Grootes, M.-J. Nadeau, and A. Schoon (1998), The carbonate 14 C background and its components at the Leibniz AMS facility, *Radiocarbon*, 40, 85–93. 2.2.3, 4.3.2
- Schlitzer, R. (Ed.) (2002), *Ocean Data View*, available at: <http://www.awi-bremerhaven.de/GEO/ODV>. 1.4
- Schmittner, A., E. D. Galbraith, S. W. Hostetler, T. F. Pedersen, and R. Zhang (2007), Large fluctuations of dissolved oxygen in the Indian and Pacific oceans during Dansgaard-Oeschger oscillations caused by variations of North Atlantic Deep Water subduction, *Paleoceanography*, 22, 1–17, doi:10.1029/2006PA001384. 4.1, 4.5.1, 4.5.3
- Schott, F. A., and J. P. McCreary Jr. (2001), The monsoon circulation of the Indian Ocean, *Progress in Oceanography*, 51, 1–123. 4.1
- Schulz, H., U. von Rad, and H. Erlenkeuser (1998), Correlation between Arabian Sea and Greenland climate oscillations of the past 110,000 years, *Nature*, 393, 54–57, doi:10.1038/31750. 1.1.2, 4.1, 4.5.2
- Shackleton, N. J. (1987), Oxygen isotopes, ice volume and sea level, *Quaternary Science Reviews*, 6(3–4), 183–190, doi:10.1016/0277-3791(87)90003-5. 1
- Shackleton, N. J. (2000), The 100,000-Year Ice-Age Cycle Identified and Found to Lag Temperature, Carbon Dioxide, and Orbital Eccentricity, *Science*, 289, 1897–1902, doi:10.1126/science.289.5486.1897. 1.1.2
- Shackleton, N. J., M. A. Hall, and E. Vincent (2000), Phase relationships between millennial-scale events 64,000–24,000 years ago, *Paleoceanography*, 15(6), 565–569, doi:10.1029/2000PA000513. 1.1.2, 2.4.1, 3.4.2, 4.1, 4.1, 4.5, 4.5.1, 4.5.1
- Siddall, M., E. J. Rohling, A. Almogi-Labin, C. Hemleben, D. Meischner, I. Schmelzer, and D. A. Smeed (2003), Sea-level fluctuations during the last glacial cycle, *Nature*, 423, 853–858, doi:10.1038/nature01690. 1.1.2, 2.1, 2, 3.2, 3.3, 3.4.3, 3.6
- Siddall, M., E. J. Rohling, W. G. Thompson, and C. Waelbroeck (2008), Marine Isotope Stage 3 sea level fluctuations: Data synthesis and new outlook, *Reviews of Geophysics*, 46, RG4003, doi:10.1029/2007RG000226. 1.1.2, 4.5.1
- Solanki, S. K., I. G. Usoskin, B. Kromer, M. Schüssler, and J. Beer (2004), Unusual activity of the Sun during recent decades compared to the previous 11,000 years, *Nature*, 431, 1084–1087, doi:10.1038/nature02995. 1.1.1

- Spooner, M. I., T. T. Barrows, P. De Deckker, and M. Paterne (2005), Palaeoceanography of the Banda Sea, and Late Pleistocene initiation of the Northwest Monsoon, *Global and Planetary Change*, 49, 28–46, doi:10.1016/j.gloplacha.2005.05.002. 3.1
- Sprintall, J., J. T. Potemra, S. L. Hautala, N. A. Bray, and W. W. Pandoe (2003), Temperature and salinity variability in the exit passages of the Indonesian Throughflow, *Deep-Sea Research Part II: Topical Studies in Oceanography*, 50, 2183–2204, doi:10.1016/S0967-0645(03)00052-3. 3.1
- Sprintall, J., S. E. Wijffels, R. Molcard, and I. Jaya (2009), Direct Estimates of the Indonesian Throughflow Entering the Indian Ocean: 2004–2006, *Journal of Geophysical Research*, 114(C07001), 1–19, doi:10.1029/2008JC005257. 1.4, 4.2
- Srifer, R. L., and M. Huber (2007), Observational evidence for an ocean heat pump induced by tropical cyclones, *Nature*, 447, 577–580, doi:10.1038/nature05785. 2.4.2
- Stineman, R. W. (1980), A Consistently Well-Behaved Method of Interpolation, *Creative Computing*, 6, 54–57. 4.3.1, 4.4.1
- Stocker, T. F., and S. J. Johnsen (2003), A minimum thermodynamic model for the bipolar seesaw, *Paleoceanography*, 18, 1–10, doi:10.1029/2003PA000920. 1.1.2
- Stott, L., C. Poulsen, S. Lund, and R. Thunell (2002), Super ENSO and Global Climate Oscillations at Millennial Time Scales, *Science*, 297, 222–226, doi:10.1126/science.1071627. 1.1.2, 2.1, 3.4.2
- Suhr, S. B., D. W. Pond, A. J. Gooday, and C. R. Smith (2003), Selective feeding by benthic foraminifera on phytodetritus on the western Antarctic Peninsula shelf: evidence from fatty acid biomarker analysis, *Marine Ecology Progress Series*, 262, 153–162. 2.4.2, 4.5.3
- Suppiah, R. (1992), The Australian summer monsoon: a review, *Progress in Physical Geography*, 16, 283–318, doi:10.1177/030913339201600302. 2.4.2, 4.5.2, 5
- Suppiah, R. (1998), Surges, cross-equatorial flows and their links with the Australian summer monsoon circulation and rainfall, *Australian Meteorological Magazine*, 47(2), 113–130. 3.4.3
- Svensson, A., K. K. Andersen, M. Bigler, H. B. Clausen, D. Dahl-Jensen, S. M. Davies, S. J. Johnsen, R. Muscheler, S. O. Rasmussen, R. Röthlisberger, J. P. Steffensen, and B. M. Vinther (2006), The Greenland Ice Core Chronology 2005, 15–42 ka. Part 2: comparison to other records, *Quaternary Science Reviews*, 25, 3258–3267, doi:10.1016/j.quascirev.2006.08.003. 2.3.1, 3.2.4, 3.2, 3.3, 4.1
- Svensson, A., K. K. Andersen, M. Bigler, H. B. Clausen, D. Dahl-Jensen, S. M. Davies, S. J. Johnsen, R. Muscheler, F. Parrenin, S. O. Rasmussen, R. Röthlisberger, I. Seierstad, J. P. Steffensen, and B. M. Vinther (2008), A 60 000 year Greenland stratigraphic ice core chronology, *Climate of the Past*, 4, 47–57. 1.1.2, 3.2.4, 3.2, 3.3, 4.1, 4.4.1, 5.1
- Székely, N., F. Bassinot, Y. Balut, L. Labeyrie, and M. Pagel (2004), Oversampling of sedimentary series collected by giant piston corer: Evidence and corrections based on 3.5-kHz chirp profiles, *Paleoceanography*, 19, doi:10.1029/2002PA000795. 2.3.1, 4.4.1
- Talley, L. D., and J. Sprintall (2005), Deep expression of the Indonesian Throughflow: Indonesian Intermediate Water in the South Equatorial Current, *Journal of Geophysical Research*, 110, C10009, doi:10.1029/2004JC002826. 4.2, 4.2, 4.5.1, 5

- Tapper, N. (2002), Climate, climatic variability and atmospheric circulation patterns in the Maritime Continent region, in *Bridging Wallace's Line: The Environmental and Cultural History and Dynamics of the Southeast Asian-Australian Region*, edited by P. Kershaw, pp. 12–30, Catena, Reiskirchen (Germany). [2.4.2](#), [4.2](#), [4.5.2](#), [5](#)
- Tedesco, K. A., and R. C. Thunell (2003), Seasonal and Interannual Variations in Planktonic Foraminiferal Flux and Assemblage Composition in the Cariaco Basin, Venezuela, *Journal of Foraminiferal Research*, *33*(3), 192–210, doi:10.2113/33.3.192. [3.4.1](#)
- Thomas, E., and A. J. Gooday (1996), Deep-sea benthic foraminifera: tracers for Cenozoic changes in oceanic productivity?, *Geology*, *24*, 355–358. [2.3.3](#)
- Timmermann, A., U. Krebs, F. Justino, H. Goosse, and T. Ivanochko (2005), Mechanisms for millennial-scale global synchronization during the last glacial period, *Paleoceanography*, *20*, doi:10.1029/2004PA001090. [2.4.1](#)
- Tomczak, M., and J. Godfrey (2003), *Regional Oceanography: An Introduction*, vol. 2nd edition, Daya, Delhi. [2.2.1](#), [4.2](#), [5](#)
- van Aken, H. M., I. S. Brodjonegoro, and I. Jaya (2009), The deep-water motion through the Lifamatola Passage and its contribution to the Indonesian throughflow, *Deep-Sea Research I*, *56*, 1203–1216, doi:10.1016/j.dsr.2009.02.001. [4.2](#)
- van Andel, T. H., G. R. Heath, and T. C. Moore (1975), Cenozoic history and paleoceanography of the central equatorial Pacific Ocean, *Memoirs of the Geological Society of America*, *143*, 1–134. [2.2.4](#), [4.3.3](#)
- van der Kaars, S., X. Wang., P. Kershaw, F. Guichard, and D. A. Setiabudi (2000), A late Quaternary palaeoecological record from the Banda Sea, Indonesia: patterns of vegetation, climate and biomass burning in Indonesia and northern Australia, *Palaeogeography, Palaeoclimatology, Palaeoecology*, *155*, 135–153, doi:10.1016/S0031-0182(99)00098-X. [4.2](#), [4.5.2](#), [4.5.2](#), [5](#)
- van Kreveld, S., M. Samthein, H. Erlenkeuser, P. Grootes, S. Jung, M. J. Nadeau, U. Pflaumann, and A. Voelker (2000), Potential links between surging ice sheets, circulation changes, and the Dansgaard-Oeschger cycles in the Irminger Sea, 60–18 kyr, *Paleoceanography*, *15*(4), 425–442. [1.1.2](#), [4.1](#)
- Voelker, A. H., P. M. Grootes, M.-J. Nadeau, and M. Sarnthein (2000), Radiocarbon levels in the Iceland Sea from 25–53 kyr and their link to the Earth's magnetic field intensity, *Radiocarbon*, *42*(3), 437–452. [2.3.1](#), [4.4.1](#), [5.1](#)
- Voelker, A. H. L., and workshop participants (2002), Global distribution of centennial-scale records for marine isotope stage (MIS) 3: a database, *Quaternary Science Reviews*, *21*, 1185–1214, doi:10.1016/S0277-3791(01)00139-1. [1.1.2](#), [1.1.2](#), [1.1.3](#), [1.3](#), [2.1](#), [4.1](#)
- Wang, P., S. Clemens, L. Beaufort, P. Braconnot, G. Ganssen, Z. Jian, P. Kershaw, and M. Sarnthein (2005), Evolution and variability of the Asian monsoon system: state of the art and outstanding issues, *Quaternary Science Reviews*, *24*, 595–629, doi:10.1016/j.quascirev.2004.10.002. [1.1.2](#)

- Wang, X., A. S. Auler, R. L. Edwards, H. Cheng, P. S. Cristalli, P. L. Smart, D. A. Richards, and C.-C. Shen (2004), Wet periods in northeastern Brazil over the past 210-kyr linked to distant climate anomalies, *Nature*, 432, 740–743, doi:10.1038/nature03067. 3.1
- Wang, Y. J., H. Cheng, R. L. Edwards, Z. S. An, J. Y. Wu, C.-C. Shen, and J. A. Dorale (2001), A High-Resolution Absolute-Dated Late Pleistocene Monsoon Record from Hulu Cave, China, *Science*, 294, 2345–2348, doi:10.1126/science.1064618. 1.1.2, 1.1.2, 2.4.1, 3.1, 3.4.3, 4.1, 4.5.2, 4.5.2
- Watanabe, O., J. Jouzel, S. Johnsen, F. Parrenin, H. Shoji, and N. Yoshida (2003), Homogeneous climate variability across East Antarctica over the past three glacial cycles, *Nature*, 422, 509–512, doi:10.1038/nature01525. 2.1
- Wells, P. E., and G. M. Wells (1994), Large-scale reorganization of ocean currents offshore Western Australia during the Late Quaternary, *Marine Micropaleontology*, 24, 157–186, doi:10.1016/0377-8398(94)90020-5. 2.2.1, 2.4.2, 4.1
- Wolff, E. W., H. Fischer, and R. Röthlisberger (2009), Glacial terminations as southern warmings without northern control, *Nature Geoscience*, 2, 206–209, doi:10.1038/NGEO442. 4.1
- Wyrwoll, K.-H., and G. H. Miller (2001), Initiation of the Australian summer monsoon 14 000 years ago, *Quaternary International*, 83-85, 119–128, doi:10.1016/S1040-6182(01)00034-9. 1.1.2, 2.1
- Wyrwoll, K.-H., and P. Valdes (2003), Insolation forcing of the Australian monsoon as controls of Pleistocene mega-lake events, *Geophysical Research Letters*, 30(24), doi:10.1029/2003GL018486. 1.1.2, 2.1
- Xu, J., W. Kuhnt, A. Holbourn, N. Andersen, and G. Bartoli (2006), Changes in the vertical profile of the Indonesian Throughflow during Termination II: Evidence from the Timor Sea, *Paleoceanography*, 21, 1–14, doi:10.1029/2006PA001278. 2.4.1, 3.1, 3.2.1, 3.4.1
- Xu, J., A. Holbourn, W. Kuhnt, Z. Jian, and H. Kawamura (2008), Changes in the Thermocline Structure of the Indonesian Outflow during Terminations I and II, *Earth and Planetary Science Letters*, 273, 152–162, doi:10.1016/j.epsl.2008.06.029. 3.1, 3.5
- Zuraida, R. (submitted), Indonesian Throughflow Variability on Sub-Orbital Timescales during Marine Isotope Stage 3: Geochemical Aspects, Ph.D. thesis, Christian-Albrechts-Universität zu Kiel, Germany. 4.3.1, 4.5.2, 4.5.2, 4.5.3
- Zuraida, R., A. Holbourn, D. Nürnberg, W. Kuhnt, A. Dürkop, and A. Erichsen (2009), Evidence for Indonesian Throughflow slow-down during Heinrich Events 3-5, *Paleoceanography*, 24, 1–15, doi:10.1029/2008PA001653. 2.6, 4.1, 4.4.1, 4.5.3

Lebenslauf

Persönliche Daten

Name: Anke Dürkop
Geboren am: 23.02.1979 in Kyritz
Familienstand: ledig

Berufserfahrung

12/2005 – heute Doktorandin, wissenschaftliche Angestellte (bis 01/2009)
Christian-Albrechts-Universität Kiel

09/2007 – 09/2007 Studien am „College of Ocean and Earth Science“ der
Tongji University Shanghai

09/2005 – 10/2005 Ausfahrt mit dem Forschungsschiff „Sonne“,
Darwin (Australien) – Jakarta (Indonesien)

Hochschulausbildung

1998 – 2005 Studium der Meteorologie an der
Christian-Albrechts-Universität zu Kiel
Diplomarbeit bei Prof. Dr. Mojib Latif

Schulausbildung

1991 – 1998 Friedrich-Ludwig-Jahn-Gymnasium Kyritz
Abschluss: Allgemeine Hochschulreife

1985 – 1991 Goethe-Grundschule Kyritz

Kiel, 29.05.2009

Präsentationsliste

Artikel in Fachzeitschriften

- A. Dürkop et al. (2008), *Centennial climate variability in the Timor Sea during Marine Isotope Stage 3*, Marine Micropaleontology 66, Seite 208-221
- N. Keenlyside, M. Latif and A. Dürkop (2007), *On Sub-ENSO Variability*, Journal of Climate, Volume 20, Seite 3452-3469
- R. Zuraida, A. Holbourn, D. Nürnberg, W. Kuhnt, A. Dürkop and A. Erichsen (2009), *Evidence for Indonesian Throughflow slow-down during Heinrich Events 3-6*, Paleoceanography, Volume 24, Seite 1-15

Diplomarbeit

Klimavariabilität im tropischen Pazifik

Ausgewählte Posterpräsentationen

- *9th International Conference on Paleoceanography*,
02. – 07. September 2007, Shanghai (China)
A. Dürkop et al., Centennial-scale climate variability in the Timor Sea during Marine Isotope Stage 3
- *European Geosciences Union General Assembly*
15. – 20. April 2007, Wien (Österreich)
A. Dürkop et al., Climate variability on centennial timescales in the Timor Sea during Marine Isotope Stages 2 and 3
- Statusseminar „Meeresforschung mit FS Sonne“
14. – 16. Februar 2007, Kiel (Deutschland)
A. Dürkop et al., Indonesian Throughflow and Australasian climate variability on centennial timescales during Marine Isotope Stages 2 and 3

Erklärung

Meine Abhandlung zur Promotion ist abgesehen von der Beratung durch meine akademischen Lehrer nach Inhalt und Form meine eigene Arbeit. Sie hat weder ganz noch teilweise hier oder an anderer Stelle im Rahmen eines Prüfungsverfahrens vorgelegen. Diese Arbeit ist unter Einhaltung der Regeln guter wissenschaftlicher Praxis entstanden.

Kapitel 2 und 3 basieren auf Manuskripten, die bereits bei wissenschaftlichen Fachzeitschriften publiziert wurden. Kapitel 4 basiert auf einem Manuskript, das bei Earth and Planetary Science Letters eingereicht werden wird.

Kapitel 3: Zuraida, R., A. Holbourn, D. Nürnberg, W. Kuhnt, **A. Dürkop**, and A. Erichsen (2009), Evidence for Indonesian Throughflow slow-down during Heinrich Events 3-5, *Paleoceanography*, 24, 1–15, doi:10.1029/2008PA001653.

Erbrachter Eigenanteil:

1. 223 von 446 Proben wurden von mir mikroskopiert. Pro Probe wurden dabei je 20 *G. ruber* und 20 *P. obliquiloculata* für die stabile Isotopenanalyse sowie 30 *G. ruber* und 20 *P. obliquiloculata* für die Mg/Ca-Analyse aus der Fraktion 250–315 μm entnommen. Darüber hinaus sind von mir 60 von 121 *G. ruber* Replikate und 61 von 122 *P. obliquiloculata* Replikate für die stabile Isotopenanalyse und die Mg/Ca-Analyse ausgelesen worden.
2. Insgesamt habe ich *G. ruber* aus 446 Proben und die zugehörigen 49 Replikate nochmals unter dem Mikroskop hinsichtlich ihrer Qualität für die stabile Isotopenanalyse geprüft und die Kammern der Foraminiferengehäuse mit einer Nadel geöffnet. Anschließend sind die Proben mit Ethanol im Ultraschallbad gereinigt worden.
3. Das Altersmodell ist für diese Veröffentlichung von mir aufgrund neu verfügbarer Eiskern-daten modifiziert worden und dient als Grundlage für die Interpretation der Proxydaten.
4. Als Co-Autorin war ich in den Prozess der Fertigstellung des Manuskriptes eingebunden.

Kiel, den 29.05.2009

.....

Anke Dürkop

